SIMULATION OF TREE STEM INJURY, AIR FLOW AND HEAT DISPERSION IN FORESTS FOR PREDICTION OF FIRE EFFECTS

DISSERTATION

Presented in Partial Fulfillment of the Requirements for the Degree Doctor of Philosophy in the Graduate School of The Ohio State University

By

Efthalia K. Chatziefstratiou, Dipl. Ing., M.S.

Graduate Program in Environmental Sciences

The Ohio State University

2015

Dissertation Committee:

Gil Bohrer "Advisor"

Matthew B. Dickinson

Ethan Kubatko

Gajan Sivandran

Barbara Wyslouzil

Copyright by

Efthalia Chatziefstratiou

2015

Abstract

This work presents two computational tools, Firestem2D and the fire module of Regional Atmospheric Modelling System (RAMS)-based Forest Large Eddy Simulation (RAFLES), which will help to make predictions of fire effects on trees and the atmosphere.

FireStem2D is a software tool for predicting tree stem heating and injury in forest fires. It is a physically-based, two-dimensional model of stem thermodynamics that results from heating at the bark surface. It builds on an earlier one-dimensional model (FireStem) and provides improved capabilities for predicting fire-induced mortality and injury before a fire occurs by resolving stem moisture loss, temperatures through the stem, degree of bark charring, and necrotic depth around the stem.

The results of numerical parameterization and model evaluation experiments for FireStem2D that simulate laboratory stem-heating experiments of 52 tree sections from 25 trees are presented. A set of virtual sensitivity analysis experiments were also conducted to test the effects of unevenness of heating around the stem and with above ground height using data from two studies: a low-intensity surface fire and a more intense crown fire. The model allows for improved understanding and prediction of the effects of wildland fire on injury and mortality of trees of different species and sizes.

Further, a study of the effects of particular properties of a high-resolution canopy resolving large eddy simulation (RAFLES) was conducted. RAFLES was later used to simulate the dispersion of heat and smoke inside and above forest canopies during low-

intensity prescribed surface fires. RAFLES is the only large eddy simulation model that can resolve the effects of the volume of the trees in the canopy. All other models neglect the volume effects and only allow the flow to interact with the forest through a prescribed drag term. As a preliminary study for the heat dispersion simulations, the effects of resolving the tree volumes on air flow inside and around semi porous barriers, such as forests and cities were evaluated.

The effects of the numerical representation of volume restriction, independent of the effects of the leaf drag were explicitly tested by comparing drag-only simulations, where neither volume nor aperture restrictions to the flow were prescribed, restriction-only simulations, where no drag was prescribed, and control simulations, where both drag and volume plus aperture restrictions were included.

Finally, RAFLES was used to investigate how different canopy structures interact with augmented surface heat flux, simulating a low-intensity surface fire and how these interactions influence turbulence and heat exchange between canopy and atmosphere. A simplified, low-intensity fire event was simulated by directly prescribing heat flux to the bottom three grid layers of the simulation, below the canopy top. The effect of canopy structure on heat accumulation in the canopy and heat dispersion in and above canopy was tested. Furthermore, for each canopy structure, homogeneous and heterogeneous fire patterns were prescribed to contrast the effect of heterogeneity of the fire pattern with that of the canopy structure.

Dedication

This is dedicated to my love Yorgo and my late grandmother Asimenia

Acknowledgements

This work could not have been completed without the help and support of many people that I was lucky to work with. First, I would like to thank my advisor Prof. Gil Bohrer for guiding and advising me in my dissertation research. I am grateful to my PhD committee members, Prof. Ethan Kubatko, Prof. Gajan Sivandran, Prof. Barbara Wyslouzil, for our fruitful discussions and their helpful comments. I would also like to thank Dr. Matthew Dickinson, PhD committee member, for his valuable guidance. Along with Anthony Bova, they helped me greatly, especially at the beginning of my PhD.

I would like to acknowledge my friends and colleagues at the laboratory in the department of Civil and Environmental Engineering, Liel Azrieli, Dr. Somayeh Dodge, Dr. Renato Frasson, Dr. Steve Garrity, Willian Kenny, Ashley Matheny, Dr. Kyle Maurer, Tim Morin, Golnaz Mirfenderesgi, Camilo Rey Sanchez, Dekel Schlomo, for our nice collaboration and fun time we had all these years.

This work is the result of many years of support from my family. Many thanks to my parents Zoi and Kyriakos, my brother Dimitris and all my relatives and friends. I am so grateful to my love and inspiration, Yorgo, for always being there, motivating me to be not only a better scientist, but a better person as well.

Vita

August 18 1983	Born, Xanthi, Greece
2007	Dipl. Ing Civil Engineering, Aristotle University of Thessaloniki
2008	M.Sc. Antiseismic design of structures, Aristotle University of Thessaloniki
2010 to present	Graduate Research Associate, Department of Civil Engineering, The Ohio State University

Publications

Journals

1. Chatziefstratiou EK, Bohrer G, "Resolving the effects of canopy structure on fire-emitted heat transport and smoke dispersion using large eddy simulations", under preparation

2. Chatziefstratiou EK, Velissariou V, Bohrer G, "Resolving the effects of aperture and volume restriction of the flow by semi-porous barriers using large eddy simulations", Journal of Boundary Layer Meteorology, doi:10.1007/s10546-014-9923-5, April 2014

3. Chatziefstratiou EK, Bohrer G, Bova AS, Subramanian R, Frasson RPM, Scherzer A, Butler BW, Dickinson MD, "FireStem2D – A two-dimensional heat transfer model for simulating tree stem injury in fires", PLoS ONE 8(7): e70110, doi:10.1371/journal.pone.0070110, July 2013

Conferences

1. Bohrer G, Maurer KD, Chatziefstratiou E, Medvigy D. Large-eddy simulations with a dynamic explicit vegetation model. Oral presentation, 12/2014. American Geophysical Union Meeting 2014, San Francisco, CA.

2. Chatziefstratiou EK, Bohrer G, Kenny WT, Resolving the effects of canopy structure on fire-emitted feat transport using large eddy simulations AMS , May 2014, Portlan, Oregon

3. Chatziefstratiou EK, Kenny WT, Heilman WE , Bohrer G, Resolving the effects of canopy structure on fire-emitted smoke dispersion using large eddy simulations, AMS , May 2014, Missoula, Montana

4. Kenny WT, Bohrer G, Chatziefstratiou EK, Development and application of the High resolution VOC Atmospheric Chemistry in Canopies (Hi-VACC) model, AGU Fall Meeting Abstracts 1, 03, December 2013, San Francisco, CA

5. Kenny WT, Chatziefstratiou EK, Heilman WE, Bohrer G, Using the High-resolution VOC atmospheric chemistry in canopies (Hi-VACC) model to simulate smoke dispersion from forest fires, 10th Symposium of fire and forest meteorology, Bowling Green, KY.

6. Chatziefstratiou EK, Bohrer G, Velissariou V, Large eddy simulations of volume restriction effects on canopy-induced increased-uplift regions, American Geophysical Union Meeting 2012, San Francisco, CA.

7. Kenny WT, Frasson R, Bohrer G, Chatziefstratiou EK, Hadlocon L, Wyslouzil B, Zhao L, Eichinger WE, Measurements and large-eddy simulations of particulate matter dispersion over a vegetative wind-break, American Meteorological Society 30th Conference on Agricultural and Forest Meteorology, Boston, MA.

8. Bohrer G, Garrity SR, Chatziefstratiou EK, Heilman WE, Large eddy simulation of canopy-structure effects on smoke dispersion from low-burning prescribed fires. 9th Symposium on Fire and Forest Meteorology, Palm Springs, CA, USA.

9. Chatziefstratiou EK, Bohrer G, Bova AS, Dickinson MB, FireStem II – a 2-D heat transfer model for simulation of stem damage in prescribed fires, 96th Ecological Society of America Annual Meeting. Austin, TX.

10. Chatziefstratiou EK, Bohrer G, Bova AS, Dickinson MB, FireStem II – a 2-D heat transfer model for simulation of stem damage in prescribed fires, 4th Fire in Eastern Oak Forests Conference, Springfield, MO.

Fields of Study

- Major field: Environmental Sciences
- Civil Engineering
- Environmental engineering
- Ecological modeling
- Biosphere-atmosphere interactions
- Computational fluid dynamics
- Large-eddy simulations
- Thermodynamics
- Fire behavior modeling

Table of Contents

Abstract ii

Dedication iv

Acknowledgements v

Vita vi

List of Tables xiii

List of figures xiv

Chapter 1: Introduction 1

Chapter 2: FireStem2D – A heat transfer model for simulating tree stem injury in fires .. 9

2.1 The FireStem2D model 11

2.1.1. Governing equation 12

2.1.2 Thermophysical Properties of Wood 14

2.1.3 Thermophysical Properties of Bark 20

2.1.4 Forcing at the outer edge of the simulated stem 21

2.1.5 Heat flux forcing 21

2.1.6 Radiant heat flux exchange with the ambient air 22

2.1.7 Desiccation 23

2.1.8 Bark charring 24

2.1.9 Tissue injury 25

2.2 Methods 26

2.2.1 Laboratory experiments 27

2.2.2 FireStem2D simulations of the laboratory experiments 30

2.2.3 Model Parameterization 30

2.2.4 Virtual experiments for sensitivity analysis 31

2.3 Model performance 34

2.3.1 FireStem2D Parameterization and Evaluation 34

2.3.2 Sensitivity analyses 38

2.4 Discussion 42

Chapter 3: Resolving the Effects of Aperture and Volume Restriction of the Flow by Semi-Porous Barriers using Large-Eddy Simulations 47

3.1 Methodology 50

3.1.1 Model description 50

3.1.2 Cut-Cell Formulation of Barriers 53

3.1.3 Barrier Structure and Drag 56

3.1.4 Boundary, Initial Conditions, and Experimental Set-up 56

3.1.5 Analysis of Simulation Results 60

3.2 Evaluation of the effects of aperture and volume restriction of the flow by barriers 61

3.2.1 Barrier effects on vertical and horizontal velocity components in the streamwise direction 61

3.2.2 Barrier effects on the vertical and horizontal velocity components in the cross-stream direction 65

3.2.3 Barrier effects on turbulence, pressure gradient and advective sources of momentum 67

3.2.4 Barrier effects on shear stress 69

3.2.5 Barrier effects on vorticity 70

3.3 Discussion 71

Chapter 4: Tracking fire-emitted heat transport in low intensity fires using large eddy simulations 76

4.1 Material and methods 78

4.1.1 Simulation of Experimental Set up 78

4.1.2 Virtual experiment 80

4.2 Results 83

4.2.1 Heat dispersion in and above canopy for “averaged case” 85

4.2.2 “Average” Vs “point” calculations 87

4.2.3 Heat storage and temperature in and above canopy 88

4.2.4 Effects of canopy and fire heterogeneity on heat flux 90

4.3 Discussion 91

Chapter 5: Conclusions 93

5.1 Summary of this work 93

5.2 Future directions 95

5.3 The future of fire effects modeling 96

Appendix: Thermal tolerance parameter estimation. 98

References 102

List of Tables

Table 1. Tree species and sections used in the laboratory experiment and parameterization of the thermophysical properties of the species. Wm, water loss rate parameter, estimated per species with the optimization process and properties of all stem sections measured in the lab and simulated by FireStem2D. The moisture parameters P1, P2, and P3 are the fraction of the maximum inner bark moisture content at the radial locations shown in Figure 2 of (Jones et al. 2004)……. 17

Table 2. Percentage of live stem cross-sectional area (percentage of the tree area that remained intact after the burning experiment) for a *Pinus strobus* and a *Quercus prinus* with diameters 8, 14, and 24 cm, for simulation heat case 1 (heating only the front and lee sides of a tree section, along half of the tree's circumference), and 2 (uniform heating around the full circumference of tree stem). …… 40

Table 3. Ten cases were simulated. The simulation time in all cases was set to 12 hours, which allowed the simulation to reach a quasi-stationary stage……. 58

Table 4. Thermodynamic parameters estimated by fitting Equation A1 to data. Data from the 25 °C pretreatment group were used from Caldwell (1993). Caldwell tested two varieties of cucumber (Poinsett and Ashley) and mean rate constants were extracted from his Figure 4 so standard deviation estimates were not valid. The temperature range (Tmin to Tmax) for each experiment is given (ºC)..…….. 100

List of figures

Figure 1. Schematic of a two-dimensional control volume used in the development of the numeric model. Stems are divided into uniform angular wedges and each wedge is discretized into nodes (e.g. P,N,S,W,E) in the radial direction. The distance between nodes is flexible (e.g. δrw) , and was set in the simulations described in this study to 1 mm. δre: distance of E from P, δrw: distance of W from P, δθn: angular distance of N from P, δθs: angular distance of S from P. 13

Figure 2. Simulated tree-stem temperature distribution in various time steps: A. The heat-up phase (t=20 sec). B. The peak temperature point (t=80 sec). C. The beginning of cool-down phase (t=100 sec). D. After long cool-down period (t=200 sec). Heating was provided in a heterogeneous way around the virtual stem section, with heat forcing at the upper right and lower left quadrant of the stem and no heat (ambient room temperature) prescribed at the upper left and lower right quadrants. The colors represent temperatures, colorbar is in K..... 15

Figure 3. Comparison of laboratory observations and FireStem2D simulations of temperature variation through time for four tree species at different locations in the stem section: **A**. Just beneath surface. **B**. At the cambium. Solid curves mark FireStem2D simulation results and dashed curves mark laboratory observations. Bold vertical lines in each time series marks the observed timing of peak heating, and defines the end of the heat-up phase, and start of the cool-down phase, afterwards. 35

Figure 4. Scatter-plots of measured time series of temperature at a single point (at cambium, at a depth of 1 to 5 cm into the stem) for 52 tree sections collected from 25

trees of 8 different species (table 1): **A.** Heat-up phase (regression line: y=0.6907(±0.013)x+96(±2.1801), R^2=0.61). **B.** Cool-down phase (regression line: y=0.6946(±0.0043)x+100.6409(±1.3906), R^2=0.64). Dashed lines mark the overall model-observation fit, solid lines mark the ideal (1:1) model-observation relationship. FireStem2D predicts the temporal dynamics of temperature in the cambium well, although it slightly overestimates the peak temperatures. 36

Figure 5. Scatter-plot of FireStem2D simulated versus measured peak-temperature time in all stem sections (Table 1). Dashed line marks the overall model-observation fit, solid line marks the ideal (1:1) model-observation relationship (regression line: y=0.9885(±0.0355)x+1.9306(±10.7992), R^2=0.98). The model is not significantly different than the observations. 36

Figure 6. Scatter-plot of necrotic depth of 52 tree sections from 25 trees of 8 different species from the heating experiments (Table 1) compared with the simulated necrotic depth estimated with FireStem2D. Dashed line marks the overall model-observation fit, solid line marks the ideal (1:1) model-observation relationship (regression line y=1.051(±0.1325)x-0.6044(±1.3612), R^2=0.84). Regression line and 1:1 line are not significantly different, proving the very good prediction of necrotic depths. 37

Figure 7. Depth of necrosis (mm) (y-axis) versus the measured total-energy flux integrated over time, THF in kJ/m^2 (x-axis), for all stem sections used in the lab experiments. Dashed line marks a logarithmic fit of simulation results (y=21.48(±1.89)log(x)-68.66(±7), R^2=0.93), solid line marks a logarithmic fit of observed laboratory results (y=16.63(±2.1)log(x)-51.05(±7.63), R^2=0.84). This model-

driven empirical relationship can be used to extrapolate stem heating and vascular cambium necrosis beyond heat fluxes used in experimental stem heating trials..... 37

Figure 8. Forcing pattern and results for Case 1: **A.** Temperature distribution in the stem at the peak of heating process. **B.** Schematic illustration of heat forcing that was applied only to the front (upper right quadrant) and lee (lower left quadrant) sides as a plot of heat flux (HF) multiplier vs. the circumferential wedge number. The first wedge is located between 0 and 1.4 degrees from the top ("north") of the stem and wedge numbers are increased in the clockwise direction. At each wedge, the HF multiplier is applied to the circumferential mean heat-flux forcing. **C.** Remaining uninjured stem after heating. **D.** Necrotic depth of each wedge of the stem. 39

Figure 9. Forcing pattern and necrotic depth results for Cases 2-5**:** For each case, the upper panel plot shows (black line) how heat forcing was applied around the tree stem and the lower panel for the same case presents the Necrotic Depth (grey line) of each wedge of the stem. Plot layout is the same as panels B and D in figure 8. **Case 2.** Heat forcing was applied evenly around the tree stem. **Case 3.** 3/8 of heat forcing was applied at each of the front and lee side and 1/8 at each of the other sides. **Case 4.** 2.67/8 of heat forcing was applied at front side and 5.33/8 at the lee side. **Case 5.** 2/8 of heat forcing was applied at front side, 4/8 at lee side, and 1/8 at the left and right sides. Our simulation results show that different heating scenarios and heterogeneity of the heat flux around the stem can have different effects on the resulting necrosis and its potential to girdle the tree stem and lead to mortality. 41

Figure 10. Simulated impact of height (above ground) on necrosis depth in two different virtual experiments: **A.** Low intensity fire: Necrotic depth at different heights: 0m, 4m, 8m, 12m, 17m, 20m for a *P. strobus* (solid markers) and a *Q. prinus* (open markers). The diagram also lists the time at which each necrotic depth was reached. In low intensity fires lower tree levels suffer strongest effects than stem parts higher in the crown. **B.** Crown Fire: Necrotic depth in different heights: 3.1m, 6.2m, 9.2m, 12.3m, 13.8m for a *P. strobus*..... 42

Figure 11. The cut-cell method: semi-porous barrier representation. Control volumes are labelled with Ψ and the corresponding control surfaces with σ. Ψ_{22} and Ψ_{21} represent the control volume of unobstructed cells. Ψ_{11}, Ψ_{12} are reduced by an amount equal to the obstructing vegetation volume portion represented in brown and green (for stem and branches, and leaves, respectively) in the corresponding grid cell. The apertures at the grid surface interfaces are also reduced such that: $0 = \sigma_{x11} < \sigma_{x12} < \sigma_{x01} = \sigma_{x21} < \sigma_{x20} = \sigma_{x22} = \Delta y \Delta z$ in the streamwise direction and $0 = \sigma_{z10} = \sigma_{z20} < \sigma_{z11} < \sigma_{z21} = \sigma_{z12} = \sigma_{z22} = \Delta y \Delta x$ in the vertical direction. Flow through the blocked apertures σ_{z10}, σ_{z20}, is totally restricted, through the fully open apertures σ_{x01}, σ_{x21}, σ_{x02}, σ_{x22}, σ_{z21}, σ_{z12}, σ_{z22}, is totally unrestricted and is partially restricted for all other apertures. 55

Figure 12. High velocity cases - Upper panels: Sparse cases, lower panels: Dense cases. The color represents: **a.** Sparse, drag-only case: normalized vertical wind velocity, averaged through the cross-wind side of the barrier, w_t / u_*, **b.** Sparse, control case: w_t / u_*, **c.** Differences of w_t / u_* between sparse cases (control **-** drag-only), **d.** Differences of normalized horizontal wind speed between sparse cases (control **-** drag-only), averaged

through the crosswind side of the barrier $u-speed_t/u_*$, **e.** Dense, drag-only case: normalized vertical wind velocity, averaged through the cross-wind side of the barrier, w_t/u_*, **f.** Dense, control case: w_t/u_*, **g.** Differences of w_t/u_* between dense cases (control **-** drag-only), **h.** Differences of normalized streamwise wind speed ($u-speed_t$) between dense cases (control **-** drag-only), averaged through the cross-wind side of the barrier, $u-speed_t/u_*$. Blue continuous lines depict the streamlines. Labels and setup for all cases are described in table 3. Upwind uplift zones (red areas) and recirculation zones (white & blue areas downwind of barrier) are stronger in control cases. A separation region occurred on the downwind edge of the barrier. 62

Figure 13. Low velocity cases - Upper panels: Sparse cases, lower panels: Dense cases. The color represents: **a.** Sparse, drag-only case: normalized vertical wind velocity, averaged through the cross-wind side of the barrier, w_t/u_*, **b.** Sparse, control case: w_t/u_* *, **c.** Differences of w_t/u_* between sparse cases (control **-** drag-only), **d.** Differences of normalized horizontal wind speed between sparse cases (control **-** drag-only), averaged through the crosswind side of the barrier $u-speed_t/u_*$, **e.** Dense, drag-only case: normalized vertical wind velocity, averaged through the cross-wind side of the barrier, w_t/u_*, **f.** Dense, control case: w_t/u_*, **g.** Differences of w_t/u_* between dense cases (control **-** drag-only), **h.** Differences of normalized streamwise wind speed ($u-speed_t$) between dense cases (control **-** drag-only), averaged through the cross-wind side of the barrier, $u-speed_t/u_*$. Blue continues lines depict the streamlines. Labels and setup for all cases

are described in table 3. Upwind uplift zones (red areas) and recirculation zones (white & blue areas downwind of barrier) are stronger in control cases. A separation region occurred on the downwind edge of the barrier. 63

Figure 14. High velocity cases, Restriction-only (no drag) cases – The color represents the normalized vertical wind speed averaged through the crosswind side of the barrier, w_t / u_*. Arrows represent the direction of the wind and they are 10 times exaggerated in the vertical direction. Labels and setup for all cases are described in table 3. In no-drag cases we still observe an uplift zone at the upwind edge of the barriers and a weak recirculation zone past the downwind edge of the canopy. 64

Figure 15. High velocity cases – The color represents: **a.** Normalized vertical wind velocity at *y-z* plane averaged through the streamwise side of the barrier, w_t / u_*. Panels from left to right: sparse drag-only case, dense drag-only case, sparse control case, dense control case. **b.** Normalized cross-wind wind velocity at *y-z* plane averaged throughout the streamwise side of the barrier, v_t / u_*. Panels from left to right: sparse drag-only case, dense drag-only case, sparse control case, dense control case. Labels and setup for all cases are described in table 3.The edge effects at *y-z* plane are not significant. 66

Figure 16. High velocity cases **-** Comparison of spatial variation of the streamwise momentum source terms, averaged through the crosswind side of the barrier. Difference of turbulence divergence between control and drag-only sparse cases (a), dense cases (b). Difference of pressure gradient terms between control and drag-only sparse cases (c),

dense cases (d), Difference of advective terms between control and drag-only sparse cases (e), dense cases (f). All terms are normalized with u_*^2 / h 68

Figure 17. Low velocity cases **-** Comparison of spatial variation of the streamwise momentum source terms, averaged through the crosswind side of the barrier. Difference of turbulence divergence between control and drag-only sparse cases (a), dense cases (b). Difference of pressure gradient terms between control and drag-only sparse cases (c), dense cases (d), **e.** Difference of advective terms between control and drag-only sparse cases (e), dense cases (f). All terms are normalized with u_*^2 / h 69

Figure 18. Comparison of variation of temporally and horizontally mean shear, averaged at three positions along the streamwise direction. **a.** Low velocity cases, **b.** High velocity cases. Labels and setup for all cases are described in table 3. Resolving the volume restriction of the barrier reduces momentum flux in the barrier. 70

Figure 19. Comparison of normalized mean vorticity, $\omega_y\left(\frac{h}{u_*}\right) = \frac{h}{u_*}\left(\frac{\partial u_t}{\partial z} - \frac{\partial w_t}{\partial x}\right)$, averaged through the crosswind side of the barrier, across 4 extreme simulation cases at 22.5m above ground. **a.** High velocity cases, **b.** Low velocity cases. Vorticity is higher in the control cases just before the canopy and drops fast as flow enters the canopy resulting in less vorticity than in drag-only cases. Just downwind of the canopy vorticity is again higher in the control cases. In low velocity cases vorticity in control cases starts decreasing faster than drag only cases very close to the canopy edge. Same happens in high velocity cases but further downwind. 71

Figure 20. Canopy description. Color depicts Leaf Area Index (LAI). Left column depicts homogeneous cases, right column depicts heterogeneous/gappy cases. A. (case name: Hom): mean LAI=2.3825, B. (case name: Het): mean LAI=2.3825, C. (case name: L75): mean LAI=1.785 (75% of initial), D. (case name: G75): mean LAI=1.785 (75% of initial), E. (case name: L50) mean LAI=1.19 (50% of initial), F. (case name: G50) mean LAI=1.19 (50% of initial). 80

Figure 21. Vertical cross-section of the experimental domain showing the burning plot. The arrows represent the wind velocity (m/s) and the color the temperature (K). 81

Figure 22. Fire patterns. Color depicts fireline heat flux (Kw/m). The total fire intensity was kept the same in all cases. A. Homogeneous case, B. Heterogeneous case (marked with the letter F from here on). 84

Figure 23. Change of vertical turbulent flux in K/s at 21 m height (≈1.5 canopy height). Blue lines enclose the area in x-axis where w't' is assumed significant. 85

Figure 24. Averaged vertical profiles of vertical turbulent flux (*TurbZ*) and advection (*AdvZ*), horizontal turbulent flux (*TurbX*) advection (*AdvZ*) for the homogeneous canopy and fire pattern. The blue line marks the height of the canopy..... 86

Figure 25. Point (at x=565m) vertical profiles of vertical turbulent flux (*TurbZ*) and advection (*AdvZ*), horizontal turbulent flux (*TurbX*) advection (*AdvZ*) for the homogeneous canopy and fire pattern. The blue line marks the height of the canopy..... 87

Figure 26. Heat storage (*HStor*) for different simulation cases. The blue line marks the height of the canopy. 89

Figure 27. Temperatures in the burning plot and above it. Canopy structures are depicted in figure 20. The letter F at the end of half of the cases stand for heterogeneous fire pattern. Fire patterns are showed in Figure 22. The blue line marks the height of the canopy. 89

Figure 28. Vertical turbulent flux Vs height. The blue line marks the height of the canopy. 90

Figure 29. Horizontal advective flux Vs height. The blue line marks the height of the canopy. 91

Chapter 1: Introduction

Properly managed wildland fires are critical for a healthy ecosystem (Keane et al. 2008). Low intensity fires can clear out the fuel accumulated under a forest canopy and prevent a future catastrophic fire. They also assist fire dependent species to compete over fire intolerant species. The biggest challenge of fire management is to eliminate excessive tree mortality, heat accumulation in the canopy and smoke dispersion to levels that accommodate the management goals and at the same time do not threaten human and ecosystem well-being. Efficient fire management can be achieved with the help of computational tools that predict the effects of a fire on trees and the atmosphere. This work discusses the development of two such computational tools, Firestem2D and fire module of Regional Atmospheric Modelling System (RAMS)-based Forest Large Eddy Simulation (RAFLES), which will help to make predictions of fire effects on trees and atmosphere.

Historically, fire would burn forests in various frequencies, depending on climate conditions and topography of the region (Waldrop et al. 2012). In the 19th century, excessive logging and fire suppression changed the historical fire pattern and resulted in substantial degradation and loss of fire-dependent ecosystems (Allen et al. 2002). Only recently, in the 1980s, ecologists started recognizing the important role that fire plays in restoration or preservation of structure and function of forests and prescribed burning gained acceptance for some management objectives (Keane et al. 2008). These objectives include hazardous fuel reduction, sites preparation for seeding or planting, competing

vegetation management, appearance and access enhancement. However, the crucial component of a successful prescribed burning is not only to achieve some of the above mentioned objectives, but to strike the balance between achieving these management goals and eliminating excessive tree mortality and smoke dispersion.

Optimal prescribed fire conditions and tactics are achieved by accurately simulating fire interaction with canopy and predefining safe mortality rates and smoke dispersion predictions. However, wildland fires are driven by complex physical and chemical processes whose interactions depend on the coupling between atmosphere, fire, topography, and solid fuels. Thus, it is very difficult to understand these processes and their interactions. Furthermore, it is very difficult to study them with full-scale repeatable experiments due to cost, labor and safety constraints (Butler et al. 2004, Clements et al. 2006). Scientists, in response to increasing demand for improvement in our understanding of wildland fires and their effects, have been working on developing fire models that are able to simulate fire behavior and provide answers to fire managers' questions (Hyde et al 2013). In this work, I present two such software tools, aimed to serve the fire managers' goals. The first model is Firestem2D that predicts tree stem necrosis around the tree and in different heights in wildfires, and the second model is fire module of RAFLES that predicts heat and smoke dispersion during burning events.

In the second chapter, FireStem2D is presented and evaluated. FireStem2D is a two-dimensional heat transfer model that predicts stem temperatures and necrotic depths during fire. FireStem2d is the evolution of a previous one-dimensional heat transfer model, FireStem (Jones et al. 2004). In FireStem2D, heat is being transferred both radially and

circumferentially and the depth of necrosis is estimated around the tree stems at different heights.

The earliest attempts to predict fire-induced tree mortality were through the development and use of empirical models. Initially, qualitative studies were conducted to estimate tree mortality (Flint 1925; McCarthy and Sims 1935). Later, the empirical models also started incorporating quantitative studies ((Kayll 1963; Martin 1963) and in the 1980's models were developed to predict the probability of tree mortality (Peterson and Ryan 1986; Reinhardt and Ryan 1989). In the 1990's scientists began to apply finite-differencing methods for modeling heat transfer (Patankar 1980; Bergman et al. 2011) to simulate fire stem heating (Rego and Rigolot 1990; Costa et al. 1991). FireStem2D is, to the best of my knowledge, the first 2-D heat transfer theoretical model that predicts stem necrosis in wildland fires.

One-dimensional models assume that heating is uniform around the circumference of the stem. However, in reality the leeside vortices of a passing flame entrain heat and combustion gasses and burn the stem heterogeneously, resulting in maximal heating on the side of the stem leeward to the wind (Gutsell and Johnson 1996). This leads to deeper injury on the lee side, but may still be insufficient to cause stem death, because injury does not occur around the entire stem. A tree can survive as long as it is not girdled, in other words a narrow unaffected wedge, about 20% of the stem area, may be sufficient to keep a tree alive (Ducrey et al. 1996). Therefore, being able to simulate the impact of the circumferential heat distribution variation is very important to safely predict tree mortality. FireStem2D, as a two-dimensional model, predicts tree circumference heterogeneous burning and calculates various necrotic depths around a tree stem.

Furthermore, FireStem and FireStem2D are, to the best of our knowledge, the first fire heat transfer models that simulate tree stem with a heat flux boundary condition. All other numerical heat transfer models in tree stems subjected to fire have used temperature boundary conditions. This allows the model to be linked to a fire behavior model that can provide the heat flux in the tree surface, but not the temperature. The ultimate goal of this work is to link the heat transfer model to a fire behavior model and give safe predictions of tree mortality to fire managers before prescribing a burn.

FireStem2D treats the stem as a cylindrical slice, a very convenient geometry for common numerical methods. FireStem2D is a finite-difference model that calculates heat transfer into the stem. The stem is divided circumferentially into wedges and radially into nodes. It takes into account the thermophysical properties (moisture profiles, heat capacity, and density) of bark and wood, the geometrical characteristics (diameter, bark and cambium thickness) of the stem and heat forcing. Following, it calculates heat transfer, desiccation and bark charring. Finally, it estimates the tissue necrosis.

In the current work, I present the parameterization and evaluation of FireStem2D based on a set of controlled laboratory stem-heating experiments. The species used for the experiments are common in eastern and central North America and particularly represent the composition of mixed oak forests in Ohio (red maple, sugar maple, mockernut hickory, yellow-poplar, blackgum, eastern white pine, chestnut oak and northern red oak). Finally, to showcase the potential applications for the model, I conducted a series of virtual experiments to explore model sensitivity to the unevenness of heating around the stem and height above ground using fire data from two studies, one of a low intensity surface fire and one of a crown fire.

In chapter 3, I study the effects of particular properties of a high-resolution canopy using large eddy simulation (RAFLES). I will later use RAFLES to simulate the dispersion of heat and smoke inside and above forest canopies during low-intensity prescribed surface fires. RAFLES is the only large eddy simulation model that can resolve the effects of tree volumes in the canopy. All other models neglect the volume effects and only allow the flow to interact with the forest through a prescribed drag term. In chapter 3, as a preliminary study for the heat dispersion simulations, I evaluate the effects of resolving the tree volumes on air flow inside and around semi porous barriers, such as forests and cities. More specifically, I discuss the effect of aperture and volume restriction of the air flow by semi-porous barriers using Large Eddy Simulations (LES). The study of air flow has applications in various research areas, such as the study of the emission and dispersion of particles and volatile organic compound from forests (Bergen 1975; Prueger et al. 2008; Wolfe and Thornton 2011), as well as forest fires further analysed in the fourth chapter.

Stems, branches, and leaves restrict the open volume inside the canopy. They constitute a step-like barrier and produce drag on the flow; but they do not completely block the flow as a solid step would do. While air does not flow through stems or leaves, viewed at the model's grid-mesh resolution, which is typically much coarser than a leaf or a stem width, they represent a subgrid-scale (SGS) disturbance that cannot be explicitly resolved. The step analogy of forest edges has been studied via analyses of field observations (Detto et al. 2008; Panferov and Sogachev 2008), data from wind-tunnel and flume experiments over artificial canopies (Seraphin and Guyenne 2008; Chamorro and Porte-Agel 2009; Markfort et al. 2010; Folkard 2011; Fontan et al. 2013), or from various

model simulations (Patton et al. 2006; Dupont and Brunet 2008b, a; Paik et al. 2009; Huang et al. 2011; Schlegel et al. 2012).

Typically, high-resolution models of forest edges, using either the large-eddy simulation (LES) or Reynolds-averaged Navier-Stokes (RANS) model, represent forest edges as a drag term while they simulate other types of sharp transitions as solid barriers. These models ignore the effects of partial volume and aperture restriction within a semi-porous barrier. In this work, RAMS-based Forest Large-Eddy Simulation (RAFLES) model that has the ability to represent both the effects of drag, primarily from leaf surfaces in forests, and of volume restriction in the barrier sub-domain, mostly from stems and branches, was employed to examine, the effects of subgrid-scale solid volume restriction in semi-porous barriers

RAFLES model is based on the Regional Atmospheric Modelling System (RAMS), a regional model that can operate as a large-eddy simulation (LES) model (Avissar et al. 1998; Avissar and Schmidt 1998) and solves the 3-D Navier–Stokes equations on a rectangular, vertically stretched grid mesh, using a quasi-hydrostatic approach and the Boussinesq approximation. The canopy in RAFLES model is represented as an explicit multi-layer, 3-D heterogeneous sub-domain where vegetation (or structure walls in an urban "canopy") exchanges drag, and latent and sensible heat with the air flowing through the canopy sub-domain (Bohrer et al. 2007).

The focus of our study is to examine the features of disturbances to the flow caused by the transition from an open space to a rectangular, prism-shaped, semi-porous barrier and back to an open, unobstructed domain. We focus on the effects that are resolved by including the volume restriction as compared to a drag-only representation of the

obstruction. This was achieved by using a cut-cell coordinate-system approach for finite-volume discretization (Adcroft et al. 1997; Walko and Avissar 2008) to represent subgrid-scale representation of barrier volume and aperture restrictions. More specifically, we compared cases where we prescribe only drag (drag-only cases) to those for which we prescribe drag and volume restriction (control cases) to investigate the differences in the uplift zones upwind of the barrier, in adjustment zones in the barrier, in turbulent zones above the barrier and in recirculation zones downwind of the barrier. For each case a low and a high wind forcing was prescribed to examine how different velocity scenarios affect the flow inside and around the barrier.

In chapter 4, a heat release module was introduced to RAFLES to examine how increased fire heat interacts with different canopy structures. It is essential but highly challenging for fire managers to strike the exact balance between burning objectives and ecological impacts of a prescribed fire. On the one hand, they want to release enough heat for enough time to achieve their restoration goals, which typically involve burning understory vegetation and ground fuel. On the other hand they want to avoid excessive tree mortality and smoke. Excessive tree mortality can radically change the forests' function and structure, whereas smoke can disperse to nearby highways and cities limiting visibility and causing respiratory problems. The heat release module of RAFLES, presented here, aims to assist planning and management of low-intensity prescribed fires (Hyde et al. 2013) by providing insight on how the interactions of different canopy and fire structures with additional surface heat flux influence turbulence and heat exchange between canopy and atmosphere.

For the purpose of this study, a simplified, low-intensity fire event was simulated by directly prescribing heat flux to the bottom three grid layers of the simulation, below the canopy top. The sensitivity of within-canopy heat accumulation rate and above canopy profiles of heat advection and turbulent heat flux to canopy and fire pattern heterogeneity was tested. More specifically, canopies of three leaf density levels were tested and each with a homogeneous and a heterogeneous canopy structure and fire pattern. Furthermore, a quadrant and an octant analysis were conducted to investigate how temperature is being transported at the top of the canopy and above it in the burning plots of the cases mentioned above.

In short, the models presented in this work can be useful components of tools that predict fire effects on trees and atmosphere. They contribute to the prediction of tree mortality and air quality during and after a prescribed fire. When prescribing a burn, fire managers will eventually be able to evaluate tree mortality and air quality expected should they choose to conduct the burn. Further, our extensive sensitivity analyses that link results to causes will assist fire managers to suggest the most appropriate fire management practices. The findings of this work will impact the broader field of fire behavior research, by shedding light on complex interactions between canopy density and fire patterns and the atmosphere. Finally, some of the findings may serve as useful input or can be incorporated into empirical and semi-empirical models commonly used by fire managers to predict fire behavior and tree mortality.

Chapter 2: FireStem2D – A heat transfer model for simulating tree stem injury in fires

FireStem2D is an extensive update and expansion of FireStem (Jones et al. 2004; Jones et al. 2006), a stem heating model developed for use by researchers and forest and fire managers for predicting effects of prescribed fires and wildfires. This work is already published in PlosOne journal (Chatziefstratiou et al. 2013).

Prescribed burning is used for various purposes, such as restoration and maintenance of fire-dependent forests, grasslands, and savannas, clearing land for cultivation, and maintaining habitat for fire-dependent plants and animals (Wade and Lunsford 1989). Early attempts to predict stem injury from wildland fire included studies to detect the factors that have the greatest effect on the survival of trees exposed to fire (Flint 1925; Starker 1934). McCarthy and Sims (1935) introduced an empirical method for estimating fire-caused tree mortality. Shirley (1936) exposed tissues to heated baths to determine lethal temperatures and produced relations for injury as a function of time and temperature for a range of species. Later studies were conducted to determine the thermal properties of wood and bark, such as bark thickness, density, thermal conductivity, heat capacity, and moisture absorption and desorption (Hale 1955; Millikin 1955; Spalt and Reifsnyder 1962; Martin 1963b). The U.S. Forest Service led the development of empirical models to predict the probability of tree mortality from both stem and crown injury (Peterson and Ryan 1986; Reinhardt and Ryan 1989). Martin (1963a) showed that it would

be possible to make mortality predictions by combining a one-dimensional (1-D) heat transfer model with a model of the denaturation of proteins at elevated temperatures. Advances to stem-heat injury prediction included the application of 1-D finite differencing methods (Patankar 1980; Rego and Rigolot 1990; Costa et al. 1991; Jones et al. 2004; Jones et al. 2006). Recently, Michaletz et al. (2012) provided evidence that cavitation and deformation of the xylem under wildland fire conditions reduce water transport in stems and branches and may affect tree injury.

One-dimensional models assume that heating is uniform around the circumference of the stem. However, in reality heating is generally maximal on the side of the stem leeward to the wind. Leeside vortices entrain heat and combustion gasses that generate a standing leeward flame that maximizes heating on the leeside of the stem. This leads to deeper injury on the lee side, but may be insufficient to cause stem death, because injury does not occur around the entire stem (Gutsell and Johnson 1996). A two-dimensional model can better simulate the effects that fire can have at different directions around the circumference of the tree. Understanding the impacts of the variation of the circumferential heat distribution on the eventual stem injury is very important, as a tree can survive as long as it is not girdled, which may be the case even where a narrow wedge, about 20% of the stem area, remains unaffected (Ducrey et al. 1996). A two-dimensional model developed by Potter and Andresen (2002) is driven by heat flux from solar radiation; however, this model was not developed or used to simulate stem heating from fires.

Following, we describe FireStem2D, a tree-stem heating model that provides two-dimensional (2-D) estimates of tissue (e.g., live bark, cambium, and wood) necrosis around the circumference of stems. We describe model parameterization and evaluation based on

a set of laboratory stem-heating experiments. Finally, we explore model sensitivity to the unevenness of heating around the stem and height above ground using fire data from two studies of a low intensity surface fire and a more intense crown fire. The software along with documentation can be accessed in the following site: http://www.firelab.org/research-projects/physical-fire/126-firestem.

2.1 The FireStem2D model

FireStem2D simulates the influence of fire as a dynamic and spatially heterogeneous heat-source around the circumference of a virtual horizontal slice of a stem. FireStem2D is a physically-based, thermodynamic, 2-D model of tree stem injury as a function of external heat forcing. It is conceptually based on the 1-D model FireStem (Jones et al. 2004; Jones et al. 2006). FireStem was the first numerical model for fire-induced heat transfer in tree stems to include a heat flux boundary condition. FireStem2D includes further developments of the forcing, numerical solver and water loss functions, and the extension to a 2-D domain that includes tangential heat flow. In contrast, Jones (2003) extended FireStem in a 2-D domain by simulating radial heat transfer within adjacent 1-D wedges that did not communicate in the circumferential direction.

FireStem2D provides increased capability for predicting fire-induced mortality and injury before a fire occurs. By directly simulating tissue temperatures, moisture loss, and charring, it forecasts the depth and circumferential extent of injury caused by incident heat flux around a stem at a given height above ground. These data are further integrated to provide a depth of tissue necrosis around the stem through a tissue viability function. Stems are simulated as circular slices (Figure 1) (Jones et al. 2004). The required inputs to

the model include geometric information (stem diameter, outer and inner bark thickness), and physical properties (thermal conductivity, density, specific heat, moisture content in inner and outer bark, and wood). Stems are divided into uniform angular wedges and each wedge is discretized into nodes in the radial direction. The distance between nodes is flexible. The numerical solver uses a Crank-Nicolson approach (Crank and Nicolson 1996). Initial conditions are prescribed as a uniform temperature (Potter and Andresen 2002). Conditions at the outer boundary throughout the simulation are enforced as a prescribed flux (temperature gradient). This forcing can change through time, simulating the heat flux from a fire line as it is moving past a tree. We use a periodic boundary to connect the last circumferential wedge to the first, and assume no flux boundary conditions at the inner (stem center) boundary. This assumption, taken for numerical simplicity, means that heat must diffuse around the inner-most ring of stem elements in order to cross the tree center to the opposing radial wedge. This is reasonable because the elements are very narrow at the inner-most ring and the circumference is not much longer than the distance across, and because under most realistic conditions only a marginal amount of heat reaches that depth.

2.1.1. Governing equation

The model simulates heat transfer in two dimensions. The equation uses cylindrical coordinates (r, for the radial axis coordinate – from bark to core in meters, and θ, for the circumferential axis coordinate – around the stem in radians) to describe the heat transfer radially (first part of right side of equation 1.1) and circumferentially (second part of right side of equation 1.1):

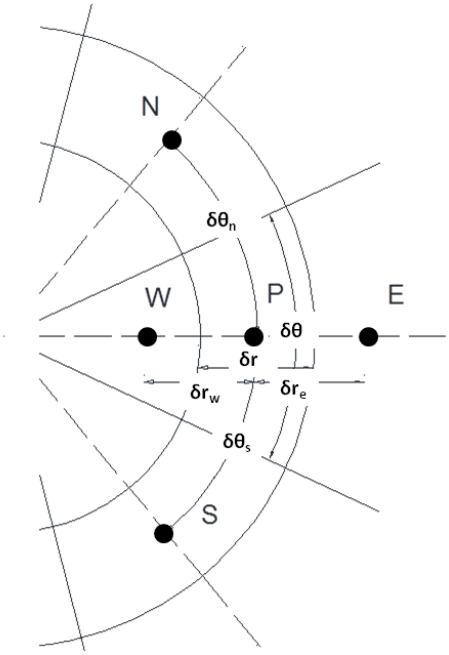

Figure 1. Schematic of a two-dimensional control volume used in the development of the numeric model. Stems are divided into uniform angular wedges and each wedge is discretized into nodes (e.g. P,N,S,W,E) in the radial direction. The distance between nodes is flexible (e.g. δrw) , and was set in the simulations described in this study to 1 mm. δre: distance of E from P, δrw: distance of W from P, δθn: angular distance of N from P, δθs: angular distance of S from P.

$$\frac{\partial \rho c_p T}{\partial t} = \frac{1}{r}\frac{\partial}{\partial r}\left(rk\frac{\partial T}{\partial r}\right) + \frac{1}{r}\frac{\partial}{\partial \theta}\left(\frac{k}{r}\frac{\partial T}{\partial \theta}\right), \qquad (1.1)$$

where t is the time coordinate (seconds), ρ is the moist stem (wood + water) density (kg/m^3), which is variable in time and space and calculated using empirical equations 1.3 and 1.6 (for the wood and bark, respectively), k is conductivity (W/m/K) calculated using

empirical equations 1.4 and 1.7 (for the wood and bark, respectively), c_p is heat capacity (J/kg/K) calculated using empirical equations 1.5 and 1.8 (for the wood and bark, respectively), and *T i*s temperature (K). Equation 1.1 is solved by numerical integration over a small, finite, annular control volume ($r_w : r_e$, $\theta s : \theta n$, shown schematically in Figure 1), (following (Patankar 1980)), and a finite incremental time step, Δt, using a Crank-Nicholson time-integration scheme:

$$\int_{t}^{t+\Delta t}\int_{\theta s}^{\theta n}\int_{r_w}^{r_e}\frac{\partial \rho c_p T}{\partial t}\,dr d\theta dt = \int_{t}^{t+\Delta t}\int_{\theta s}^{\theta n}\int_{r_w}^{r_e}\left[\frac{1}{r}\frac{\partial}{\partial r}\left(rk\frac{\partial T}{\partial r}\right)+\frac{1}{r}\frac{\partial}{\partial \theta}\left(\frac{k}{r}\frac{\partial T}{\partial \theta}\right)\right]dr d\theta dt, \qquad (1.2)$$

2.1.2 Thermophysical Properties of Wood

The moist density of the wood and its thermal conductivity are not assumed constant in the model. Both of these thermophysical properties vary in space and time and are affected by the wood structure, which varies in space from the central to the peripheral parts of the stem, and its moisture content, which varies both as a function of the wood structure and as a function of the heating process. The initial moisture content of the wood varies from the center of the tree, through the heartwood and sapwood to the vascular cambium. The following relationship was created to calculate the initial moist density of hardwoods (Martin 1963a; Simpson and TenWolde 1999; Jones 2003):

$$\rho = \rho_w\left[1+\left(\frac{P1-P2}{r_d}\times r + P2\right)M\right], \qquad (1.3)$$

where ρ_w (kg/m^3) is the density of the dry wood at each location of interest along the radial coordinate, r_d (m) is the radial distance to the vascular cambium, M (unitless ratio of water mass per unit dry wood mass) is the maximal moisture content near the bark of the modeled wood section, and the moisture parameters P1, P2 scale the fraction of the maximum inner bark moisture content at the radial locations (a graphic example is shown in Figure 2 of Jones et al. (2004) and see also Jones (2003), and are given in Table 1.

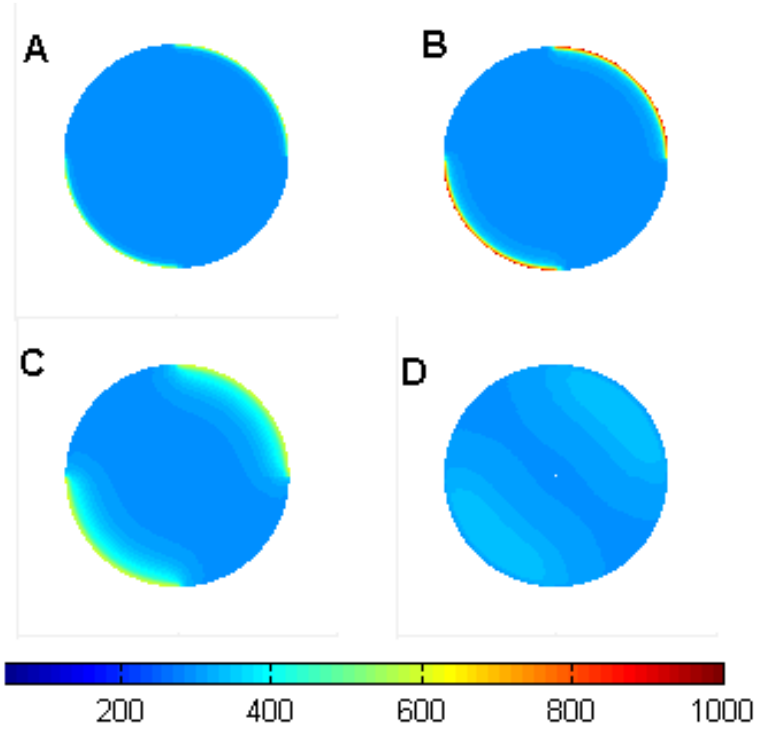

Figure 2. Simulated tree-stem temperature distribution in various time steps: A. The heat-up phase (t=20 sec). B. The peak temperature point (t=80 sec). C. The beginning of cool-down phase (t=100 sec). D. After long cool-down period (t=200 sec). Heating was provided in a heterogeneous way around the virtual stem section, with heat forcing at the upper right and lower left quadrant of the stem and no heat (ambient room temperature) prescribed at the upper left and lower right quadrants. The colors represent temperatures, colorbar is in K.

Thermal conductivity was calculated as a function of the wood density and moisture content (Glass and Zelinka 2010) as:

$$k = G_M(0.1941 + 0.4064M) + 0.01864, \qquad (1.4)$$

where G_M is specific gravity based on oven-dry mass and volume at moisture content and is equal to ρ/ρ_w ,and M (unitless ratio of water mass per unit dry wood mass) is the moisture content. Thermal conductivity increases as density, moisture content, temperature, or extractive content of the wood increase.

Heat capacity of the moist wood, c_p (J/kg/K) is calculated as a weighted sum of c_{p0} (the heat capacity of dry wood), c_{pw} (the heat capacity of water), and A_c (the energy in the wood-water bond):

$$c_p = \frac{c_{p0} + c_{pw}M}{1+M} + A_c, \qquad (1.5)$$

where $c_{p0} = 0.1031 + 0.00386T$; $c_{pw} = 3.8 + 130/(645 - T)$, for T<630 (K); c_{pw} = 15, for T>630 (K)*;* and $A_c = M(-0.06191 + 2.36\times10^{-4}T - 1.33\times10^{-4})$ (Bergman et al. 2011). The second term in the numerator of the right hand side of the equation is an adjustment for the moisture content of wood, c_{pw}, and the last term on the right further adjusts the heat capacity to account for the energy in the wood-water bond.

Species	Tree #	Section #	Diameter (mm)	Bark thickness (mm)	Mean Moisture Content (%)	Mean Density (g/cm2)
***Acer rubrum* (L.)**	1	1	140	2.84	80.63	0.523
Parameters	1	2	131	3.5	80.63	0.523
W_m P1 P2 P3	2	1	125	3	69.97	0.629
0.8 1 0.5 0.2	2	2	122	3	69.97	0.629
	3	1	136	4	67.89	0.613
	3	2	128	3.9	67.89	0.613
***Acer saccharum* (Marsh.)**	4	1	140	3.7	45.3	0.63
Parameters	4	2	120	3	45.3	0.63
W_m P1 P2 P3	4	3	126	3	45.3	0.63
1 1 0.5 0.2	5	1	128	3	49.21	0.662
	5	2	126	3	49.21	0.662
	6	1	133	3.4	47.14	0.677

Continued

Table 1. Properties of tree species and sections used in the laboratory experiment and simulations. W_m, is water loss rate parameter, estimated per species with the optimization process and properties of all stem sections measured in the lab and simulated by FireStem2D. The moisture parameters $P1$, $P2$, and $P3$ are the fraction of the maximum inner bark moisture content at the radial locations shown in Figure 2 of (Jones et al. 2004)**.**

Table 1 continued

***Carya tomentosa* (Lam.)**				7	1	139	8	36.47	0.735
Parameters				8	1	151	10.4	36.64	0.69
W_m	P1	P2	P3	8	2	130	8.6	36.64	0.69
0.2	1	0.83	0.26	9	1	140	8.54	38.04	0.731
				9	2	129	6.9	38.04	0.731
***Liriodendron tulipifera* (L.)**				10	1	136	6.2	88.13	0.437
Parameters				10	2	132	7	88.13	0.437
W_m	P1	P2	P3	11	1	130	8	87.99	0.401
1	0.63	0.26	0.19	11	2	126	8	87.99	0.401
				12	1	130	8	105.11	0.443
				12	2	126	6	105.11	0.443
***Nyssa sylvatica* (Marsh.)**				13	1	134	6.2	57.12	0.468
Parameters				13	2	129	6.1	57.12	0.468
W_m	P1	P2	P3	14	1	132	6	51.82	0.501
0.6	1	0.5	0.2	14	2	102	6	51.82	0.501
				15	1	135	5.8	44.91	0.509
				15	2	110	4	44.91	0.509

Continued

Table 1 continued

***Pinus strobus* (L.)**				16	1	125	3.7	100	0.338
Parameters				16	2	105	2.9	100	0.338
W_m	P1	P2	P3	16	3	100	2.4	100	0.338
0.8	0.63	0.26	0.19	17	1	140	3.1	100	0.3
				17	2	140	2.6	100	0.3
				18	1	125	3.1	100	0.323
				18	2	123	3.1	100	0.323
***Quercus prinus* (L.)**				19	1	134	9	40.57	0.633
Parameters				19	2	130	7	40.57	0.633
W_m	P1	P2	P3	20	1	120	8	39.39	0.609
0.1	1	0.5	0.2	20	2	114	8	39.39	0.609
				21	1	132	6	40.9	0.631
				21	2	128	8	40.9	0.631
				22	1	124	12	41.97	0.672
				22	2	120	11	41.97	0.672
				22	3	108	8	41.97	0.672
***Quercus rubra* (L.)**				23	1	128	5.9	37.53	0.697
Parameters				23	2	128	5	37.53	0.697
W_m	P1	P2	P3	24	1	142	8	35.93	0.724
0.5	1	0.5	0.2	24	2	124	6	35.93	0.724
				25	1	140	9	42.81	0.716
				25	2	132	5	42.81	0.716

2.1.3 Thermophysical Properties of Bark

Bark densities are calculated for each control volume based on the dry bark density and the local moisture content, be it inner (live) bark or outer (dead) bark:

$$\rho = \rho_b \left(1 + M\right), \qquad (1.6)$$

where ρ_b (kg/m^3) is the density of the dry bark.

Martin (Martin 1963a) provides empirical parameterization for the conductivity of the bark, as a function of the dry density (first term on right hand side), moisture content (second term), and temperature (third term):

$$k = 0.0419 \cdot \left[0.005026\,\rho_b + 0.013241\left(\rho - \rho_b\right) + 0.0078\left(\mathrm{T} - 273.15\right) - 0.397\right], \qquad (1.7)$$

Martin (Martin 1963a) also provides empirical parameterization for bark heat capacity as a function of temperature and water content:

$$c_p = 4186.8 \cdot \left[0.264 \; + 0.00116\left(\mathrm{T} - 273.15\right) + Mc_{pw} / 4.19 + \Delta c\right], \qquad (1.8)$$

where Δ_c (cal×g^{-1}×K^{-1}) is an empirical correction for the effect of moisture on heat capacity (Martin 1963a).

2.1.4 Forcing at the outer edge of the simulated stem

The simulation is driven by a prescribed forcing of heat flux, which represents the heating that is provided by the fire. This forcing is prescribed by the user as a time series for fire-driven convective and radiant heat fluxes at the outer edge of each numerical section (wedge) around the stem. The model adds this prescribed heat flux to the flux budget at the outer edge of the bark and uses the net flux as a numerical boundary condition, at the outermost node of the bark. The net heat flux at the surface node (representing the outer layer of the bark) is calculated by the model as:

$$q''_{tot,(0,j)} = q''_{forcing} - q''_{rad,(0,j)} - q''_{desiccation} - q''_{charring} \quad , \qquad (1.9)$$

where $q''_{forcing}$ is prescribed by the user in the simulation input file and represents the sum of fire-induced radiant and convective heat fluxes, $q''_{rad,(0,j)}$ is net radiant heat flux (W/m^2) exchange with the ambient air, $q''_{desiccation}$ is heat flux due to desiccation (W/m^2), and $q''_{charring}$ is heat flux due to charring (W/m^2).A simulation typically starts before the fire ignition (or when the fire line is far from the target stem) at which time the initial stem temperature is close to ambient. In that case, the initial desiccation and charring components are zero and do not need to be accounted for as initial conditions.

2.1.5 Heat flux forcing

The users can either prescribe the heat flux from direct measurement or from output of a high resolution fire behavior model that provides the heat flux. Alternatively, users can approximate the values of heat flux based on the fire temperature around the

stem. An example for such calculation is provided in the section '*virtual experiments for sensitivity analysis*', below. The air temperature around the stem could be measured in a real fire experiment or generated synthetically using a fire dynamics model or an empirical fire-temperature curve. The total heat flux forcing, $q''_{forcing}$, is the sum of a radiant, q''_{inrad}, and a convective, q''_{inconv}, components:

$$q''_{forcing} = q''_{inrad} + q''_{inconv} \quad , \tag{1.10}$$

2.1.6 Radiant heat flux exchange with the ambient air

Radiant heat flux exchange with the ambient air at the outer edge of the simulated stem is prescribed as:

$$q''_{rad,(0,j)} = \sigma \cdot (T^4_{s,(0,j)} - \varepsilon \cdot T^4_{o,(0,j)}) \quad , \tag{1.11}$$

where the right hand side is the black-body radiation, where $\varepsilon=1$ is black-body emissivity coefficient, σ=5.67×E-8 (W/m^{2}K^4) is the Stefan-Boltzmann constant, T_s is the temperature at the surface node (K) and T_o is the ambient air temperature (K) before the fire ignition or far away from the fire. The subscript *(i,j)* marks the coordinate in the polar grid system, where i is the grid number from the outer edge along the radial direction and j marks the angular wedge number around the stem. Here, i=0 marks a boundary condition at the outer edge of the tree's bark.

2.1.7 Desiccation

The evaporation of water within the bark acts as an additional protective barrier against temperature increases that can damage the stem (Jones 2003). The energy lost by evaporation is calculated as the mass of water loss multiplied by the most recently calculated specific heat of water. Heat flux forcing due to desiccation is characterized as follows:

$$q''_{desiccation,(0,j)} = \frac{\partial w}{\partial t} \cdot V \cdot dt \cdot c_{pw} \cdot T_{s(0,j)}, \qquad (1.12)$$

where V is control volume (m^3), and $\partial w / \partial t$ is the time rate of change of water volume in a numerical cell of wood, which is solved using the empirical relationship from (Morvan and Dupuy 2001):

$$\frac{\partial w}{\partial t} = W_m \frac{k_w}{\sqrt{T_{(j,i)}}} \rho \cdot M \cdot \exp\left(-\frac{E_w}{R T_{(j,i)}} \right), \qquad (1.13)$$

where W_m is a parameter for water loss rate due to high temperature, calculated for the purpose of this work. Its value was parameterized per species using empirical data from a series of laboratory experiments. M is moisture content (unitless ratio), T is temperature (K), ρ is moist wood density (kg/cm^3), the coefficient k_w=6.05×E5 ($K^{0.5}$ / s) and the exponential factor E_w/R= 5956 (K) are taken from (Morvan and Dupuy 2001). The empirical parameterization accounts for unmodeled factors, such as resistance to vapor transfer radially through the stem.

2.1.8 Bark charring

As the temperature of desiccated bark rises, charring may occur. Charring is the oxidation of the solid carbonaceous material that remains after all moisture and volatile matter has been driven off. Although only a thin portion of the original bark chars, the thermal properties of the charred layer affect the rate of energy transfer into the vital tissues of tree stems (Jones 2003). Heat flux forcing due to charring is characterized as follows

$$q''_{charring,(0,j)} = \frac{\partial p}{\partial t} \cdot V \cdot dt \cdot T_{s(0,j)}, \qquad (1.14)$$

where V is control volume (m^3) and $\partial p / \partial t$ is the time rate of charring. Charring is modeled in a manner analogous to water loss, with the exception that in each time step charring can only occur at the one node that is deeper from a previously charred node. The rate equation is based on (Regland and Aerts 1991).

$$\frac{\partial p}{\partial t} = P_m \cdot A_p \cdot \rho \cdot \left(1 - c_f\right) \cdot \exp\left(-\frac{E_p}{R T_{(j,i)}}\right), \qquad (1.15)$$

where P_m is the pyrolysis multiplier, c_f =0.30 (unitless) is the density fraction, the coefficient A_p=7 $\times 10^7$ (s^{-1}) and the exponential factor E_p/R=15,610 (K) are empirical parameters, taken from (Regland and Aerts 1991). The combustion and heat generation by bark material (glowing or flaming combustion) is neglected though it is known to be important for certain species (Gill and Ashton 1968; Vines 1968). In our experiments we

do not parameterize for P_m as we do not observe charring in any case, because of relatively low temperatures in the bench-scale experiments.

2.1.9 Tissue injury

Once the temporal dynamics and spatial distribution of temperature in the stem section is resolved, it is possible to relate the temperature to potential stem injury. Thermally induced tissue viability is described by a temperature-dependent rate equation, where the rate of decline in tissue viability is proportional to current viability (Dickinson and Johnson 2001; Dickinson 2002; Dickinson et al. 2004):

$$dN / dt = -f \cdot N, \qquad (1.16)$$

where N is the degree of viability for a given node (0=dead to 1=alive). The viability progression rate, f (s^{-1}), is calculated as:

$$f = -\left(\frac{kB}{h} \cdot T_{(j,i)} \right) \cdot \exp\left(\frac{\Delta H \cdot \left(\frac{T_{(j,i)}}{T_{crit}} - 1 \right) - b_{comp} \cdot T_{(j,i)}}{R \cdot T_{(j,i)}} \right), \qquad (1.17)$$

where T (K) is temperature at point *(j,i)* in the tree stem, kB is Boltzmann constant, h is Planck's constant and kB/h=2.08×e^{10} ($K^{-1}s^{-1}$), R=8.31 (J mol^{-1} K^{-1}) (Dickinson et al. 2004) is the universal gas constant, and ΔH (kJ/mol) is activation enthalpy, and T_{crit} and b_{comp} are

parameters of a compensation law relating thermodynamic parameters. Details on parameter estimation are given in the Appendix.

Viability level can be calculated for a constant temperature exposure by solving equation 1.17 as a first-order differential equation:

$$N = N_0 \exp(-f \cdot t_{tot}), \qquad (1.18)$$

where N_0 is initial viability and t_{tot} is total heating time. If N at a certain node falls below 0.001, the node is considered dead and depth of necrosis corresponds to the depth of the most interior dead node after completion of stem cooling. This value of N is arbitrary. The relationship between viability rate and extent of necrosis is exponential and 0.001 represents a 3×log reduction, at which level viability can be assumed negligible as this is a very low value relative to the decimal precision of most of the parameters used in the model (e.g., (Dickinson and Johnson 2004)). Finally, by solving for discrete time intervals, viability level N at each node at each time step Δt can be calculated for a temperature regime that varies through time:

$$N(t + \Delta t) = N(t) \exp(-f \cdot \Delta t), \qquad (1.19)$$

2.2 Methods

All necessary permits were obtained for the described field studies. Permits were given by the US Department of Agriculture - Forest Service to Matthew B Dickinson and

Warren Heilman at the Delaware, OH and Lancing, MI stations of the Forest Service's Northern Research Station.

2.2.1 Laboratory experiments

Controlled laboratory stem-heating experiments were conducted on stem sections collected from eight tree species during the dormant season. We selected species that are common in eastern and central North America and particularly represent the composition of mixed oak forests in Ohio where the experiment was conducted: *Acer rubrum* (L.) (red maple), *Acer saccharum* (Marsh.) (sugar maple), *Carya tomentosa* (Lam.) (mockernut hickory), *Liriodendron tulipifera* (L.) (yellow-poplar), *Nyssa sylvatica* (Marsh.) *var. sylvatica* (blackgum), *Pinus strobus* (L.) (eastern white pine), *Quercus prinus* (L.) (chestnut oak) and *Quercus rubra* (L.) (northern red oak). Most of these species are typically classified as thin-barked (Harmon 1984), except *Q. prinus* and *C. tomentosa,* which are intermediate (Table 1 includes the details of all stem sections used, including bark thickness). The results of these experiments were used for the parameterization and evaluation of FireStem2D.

The 30 cm stem sections were prepared for heating by first coating the sawn ends with paraffin to reduce water loss during heating. Sections were then wrapped with fiberglass-backed aluminum fire-shelter material (Anchor Industries, Inc., Evansville, IN) containing a 10 cm x 10 cm square opening through which bark was heated. The exposed section of each stem was heated using six 25 cm, 400 watt, Type LHP rod heaters (Glo-Quartz, Mentor, OH, USA). Rods were spaced approximately 3 cm apart in an arc positioned 5 cm away from the exposed bark surface. An aluminum shield was placed

behind the rods to reflect radiation from the side opposite the target stem. Power to the heating rods was regulated by two variable AC transformers set at 115 VAC.

Prior to heating, stem sections were fitted with three thermocouples (0.52 mm diameter type K probes; Omega Engineering, Inc., Stamford, CT, USA) to monitor temperatures at the bark surface, just beneath the bark surface, and at the cambium layer between bark and wood. Sections were heated until the cambial probe reached a temperature of 343 K, at which time the rods were turned off. In several cases, the cambial probe was inadvertently placed in the wood. Temperatures and heat flux continued to be recorded until the cambial temperature returned to within 10% of the ambient temperature. Total heat flux (convective plus radiative) was measured with a MedTherm Schmidt-Boelter-type heat-flux sensor (Model 64-15T-15R(S)-21210, MedTherm Corporation, Huntsville, AL, USA) logged on a Campbell CR10X micrologger (Campbell Scientific, Logan, UT, USA) at 1-second intervals. The sensor was encased in a 2.5 cm diameter copper cylinder and was positioned on the top of the stem section, flush with the bark surface. Insulating cotton was placed on the top of the stem section to shield the stem from the casing. We examined the MedTherm output for drift associated with temperature rise in the copper cylinder and detected none even over 10 minute exposures. Radiative heat loss likely dampened temperature rise because the copper body was exposed and only received radiation at its front.

MedTherm voltage output was converted to total heat flux (kW m^{-2}) through calibration relationships provided by the Rochester Institute of Technology Center for Imaging Sciences (Robert Kremens, Rochester Institute of Technology, unpublished data). The relationship between MedTherm voltage and blackbody heat flux is directly

proportional in the range of heat fluxes relevant for this experiment and, consequently, a single 673 K blackbody temperature was used. Total heat fluxes were later adjusted to reflect the estimated total heat flux value at the bark surface at the midpoint of the window. To do this, we used the ratio of two independent MedTherm measurements taken simultaneously during heating regimes identical to those used during the stem heating trials, but with the stem section removed. The MedTherms were placed at the top of the stem section as in the stem heating trials and at the same location as it would have at the surface of the bark at the center of the 10 cm window.

The depth of necrosis into the stem following each stem heating experiment was determined by staining thin stem sections with triphenyl tetrazolium chloride (Bova and Dickinson 2005). Measurements taken on three ~1 cm thick stem cross-sections cut at the midpoint of the window and 1 cm above and below the midpoint were used to calculate average depth of necrosis. Total bark thickness was also measured in all samples and separate outer bark measurements were taken on those species with well-defined inner and outer bark. The depth of the thermocouple probe used to measure the cambial temperature at the midpoint of the window was also determined during the section preparation process. Sections for necrosis and thermocouple depth determination were cut with a power miter saw.

Moisture content and oven-dry density were measured on samples of outer bark, inner bark, and sapwood collected from a section that was removed from the top of each stem just prior to heating. Average moisture content was determined by weighing samples collected from the fresh section and drying the samples at 380$\pm$2 K (Siau 1983). Oven-dry density (oven dry mass/fresh sample volume) was calculated by weighing another set of

samples and coating them in molten paraffin before weighing them again. Sample volume was determined using Archimedes rule by submerging the sample into a beaker of water. The volume of the paraffin (mass/density) was then subtracted to determine the volume of the fresh wood sample. Moisture content was used to estimate oven-dry mass and calculate oven-dry density.

2.2.2 FireStem2D simulations of the laboratory experiments

We used FireStem2D to simulate the results of the laboratory heating experiments. Simulated stems were divided into 16 uniform angular wedges, and each wedge was discretized into nodes in the radial direction. The distance between nodes in this simulation study was 1 mm. The required inputs to the model were calculated given data from the laboratory experiments and are shown in table 1.

2.2.3 Model Parameterization

We compared laboratory observations and FireStem2D simulations to estimate a single model parameter: the temperature-driven water loss rate, W_m (eq. 1.14). Morvan and Dupuy (Morvan and Dupuy 2001) found that its value lies between 0.01 and 1 for a drying fuel particle. We used an optimization process to determine the best approximation to its value. The goal was to find W_m that minimized the error between lab measurements and simulations of necrotic depth and cambium temperatures over all samples of the same species. We define the species-specific error, E_s, as:

$$E_s = \sum_{is=1}^{ns} \left[\left(\frac{T_{FS} - T_{lab}}{T_{lab}} \right)_{is}^2 + \left(\frac{N_{FS} - N_{lab}}{N_{lab}} \right)_{is}^2 \right], \qquad (1.20)$$

where *ns* is the number of samples of a particular species and the notation *is* represents a counter for sample and corresponding model simulation number. The first term on the right hand side represents model errors in estimation of temperature, T_{FS} (K), is the temperatures calculated with FireStem2D, resampled every 200 seconds, T_{lab}, the corresponding temperatures measured in the lab. The second term on the right hand side represented model errors in estimation of necrotic depth, N_{FS} (mm), is the necrotic depth calculated with FireStem2D, N_{lab}, the corresponding necrotic depth measured in the lab.

2.2.4 Virtual experiments for sensitivity analysis

To showcase the potential application for the model, we have conducted a series of virtual experiments to test: (1) the effects of the spatial heterogeneity of the distribution of heat around the stem and its interaction with stem diameter, and (2) the effects of height. We compared the predicted extent of stem injury at different heights from surface fire with predictions for a crown fire. We used synthetic forcing, qualitatively based on data from a prescribed surface fire and a crown fire (Butler et al. 2004).

2.2.4.1 Symmetry experiment

As a fire passes a tree, it usually heats the stem unevenly according to the direction and velocity of the wind. We used FireStem2D to examine the different effects a given total heating dose can have as a function of its distribution over the circumference of a tree. We used a virtual test section with an assumed diameter of 14 cm and the thermal properties

of *Pinus strobus* (as measured in the lab experiments, tree 16-1 from Table 1) to evaluate the effects of various spatial distributions of radiant heat-flux forcing and its interaction with stem diameter. The virtual test section was divided into 256 uniform wedges and each wedge was discretized into nodes in the radial direction. The distance between nodes was 0.1 mm. We used the same time series of heat-flux forcing that was applied to tree 16-1 (Table 1) in the lab experiments. We redistributed the heat flux circumferentially in five different ways, varying from uniform to strongly uneven. We further tested two of these five heating cases: an uneven heat-flux distribution (case 1), heating only the windward and leeward sides; and uniform heating around the stem (case 2), for three different assumed diameters of a white pine stem section 16-1 (8 cm, 14 cm and 24 cm).

2.2.4.2 Effect of height above ground

To examine how fire effects change with height, we simulated tree slices in various heights from the ground. This virtual experiment simulated both a surface fire and a crown fire to compare the results. We used virtual *P. strobus* and *Q. prinus* stems with 15 cm diameter and bark thickness of 2 mm and 7 mm, respectively with thermal parameters set as the mean values of sections of tree 16-1 and 19-1, respectively, from the laboratory experiments. The virtual stems were divided in 16 uniform wedges and each wedge was discretized into nodes in the radial direction. The distance between nodes was 1 mm.

2.2.4.2.1 Surface fire case

We assumed a range of fire temperatures between ambient (pre-fire) and 823 *K*. This range was observed in low-intensity prescribed surface fires (Jacoby et al. 1992). We used a normalized, high frequency time series to describe the temporal dynamics of the

heat forcing. This time series is based on observations from a prescribed fire conducted from 19-21 March 2011 at the Pine Barrens, NJ, USA (Warren Heilman, U.S. Forest Service, personal communication). Data included air temperature at several heights (1 – 20 m) above the ground, at 1-minute intervals during the entire day when the fire occurred.

We used air temperature measurements during the fire to calculate the radiant heat flux in different heights (z) based on equations 1.10-1.12, as follows:

$$q''_{forcing}(z) = h \cdot \left(T_f(z) - T_o(z)\right) + \sigma \cdot \left(T_f(z)\right)^4, \qquad (1.21)$$

where T_f(z) is the air temperature directly above the fire at height z (m) above ground and T_o(z) is the ambient air temperature at the same height before the fire started. Measurements show that $T_f(0)$ = 823 K (temperature at ground level), and $T_f(20)$ = 285 K (temperature above the crown height). We interpolated the heat-flux forcing for each simulated height between these two levels assuming an exponential profile, i.e. $q''_{forcing}(z) = q''_{forcing}(0) \cdot e^{c \cdot z}$, where c is a shape parameter that was found by solving this equation for z=20. In this virtual experiment we found that c = -0.0155.

These synthetic forcing conditions were calculated only for sensitivity analysis purposes. Horizontal cross-sections of a *P. strobus* (15 cm diameter, 2 mm bark thickness, and other properties set to those of tree 16.1 in Table 1) and a *Q. prinus* (15 cm diameter, 7 mm bark thickness, and other properties set to those of tree 20-1 in Table 1) stem at different heights were simulated.

2.3.4.2.2 Crown fire case

To examine the differences between a low-intensity fire and a crown fire and to evaluate how well FireStem2D can depict each, we used data from a crown fire (Butler et al. 2004) to evaluate the fire effects on a *P. strobus* (15 cm diameter and rest of properties same as tree 16-1 from Table 1) at different heights. The net heat flux is the sum of radiant and convective heat flux. To calculate net heat flux at various heights we used mean values of radiant heat fluxes and temperatures measured at tower 5 located in plot 1 (see Figure 2 in (Butler et al. 2004)).

2.3 Model performance

FireStem2D simulates temperature distribution in a tree stem in two dimensions. Longitudinal energy transport is not simulated. Example temperature distributions during different heating phases are depicted in Figure 2. The images illustrate the radial and circumferential heat transfer due to conduction.

2.3.1 FireStem2D Parameterization and Evaluation

Results from the physical experiments closely matched results from FireStem2D simulations of the same cases (Figures 3-6). To illustrate this, Figure 3 presents time series of temperatures of an *Acer saccharum (*tree 4-1), a *Liriodendron tulipifera* (tree 10-1), a *Nyssa sylvatica* (tree 13-1), and a *Quercus prinus* (tree 19-1). The species specific parameter, $W_{m,}$ showed a wide range between 0.05 in *Carya tomentosa* and *Quercus prinus* to 0.95 in *Acer saccharum* (Table 1).

Figure 4 shows comparisons between the observed time series of temperature at a single point, at a depth of 1-5 cm in 52 tree section from 25 trees of all eight species from the heating experiments, to the simulated temperatures of the corresponding grid-cell with FireStem2D. It is separated into heat-up and cool-down phases. FireStem2D tends to overestimate stem temperature regimes during heating and cooling phases (Figure 4). However, it provides very good predictions of the time of the peak temperatures for all cases (Figure 5). FireStem2D also shows very good potential for predicting the necrotic depth of tree stem subjected to heat flux (Figure 6).

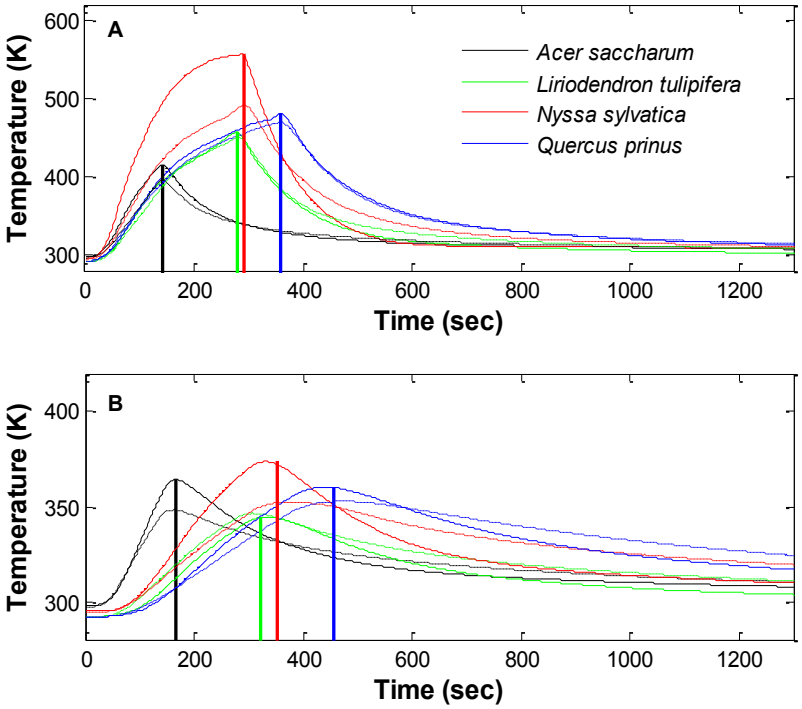

Figure 3. Comparison of laboratory observations and FireStem2D simulations of temperature variation through time for four tree species at different locations in the stem section: **A**. Just beneath surface. **B**. At the cambium. Solid curves mark FireStem2D simulation results and dashed curves mark laboratory observations. Bold vertical lines in each time series marks the observed timing of peak heating, and defines the end of the heat-up phase, and start of the cool-down phase, afterwards.

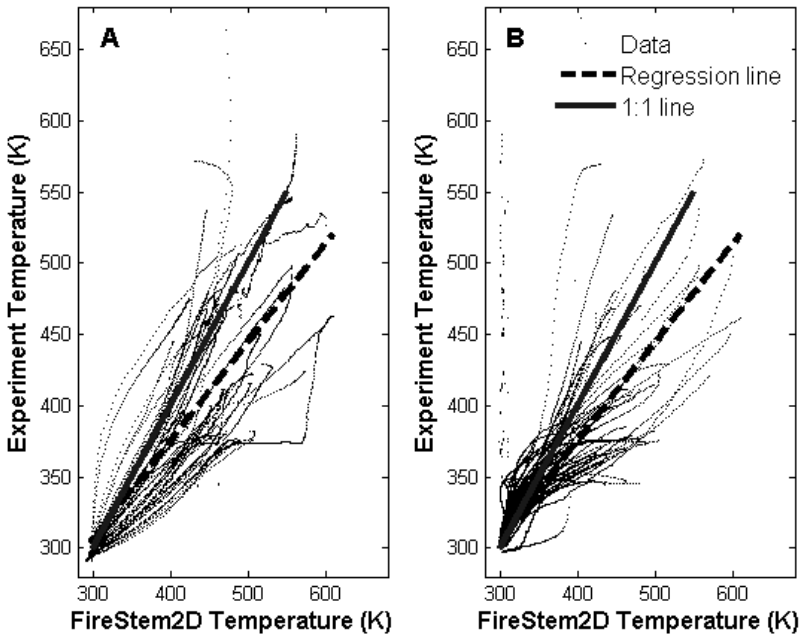

Figure 4. Scatter-plots of measured time series of temperature at a single point (at cambium, at a depth of 1 to 5 cm into the stem) for 52 tree sections collected from 25 trees of 8 different species (table 1): **A.** Heat-up phase (regression line: $y=0.6907(\pm0.013)x+96(\pm2.1801)$, $R^2=0.61$). **B.** Cool-down phase (regression line: $y=0.6946(\pm0.0043)x+100.6409(\pm1.3906)$, $R^2=0.64$). Dashed lines mark the overall model-observation fit, solid lines mark the ideal (1:1) model-observation relationship. FireStem2D predicts the temporal dynamics of temperature in the cambium well, although it slightly overestimates the peak temperatures.

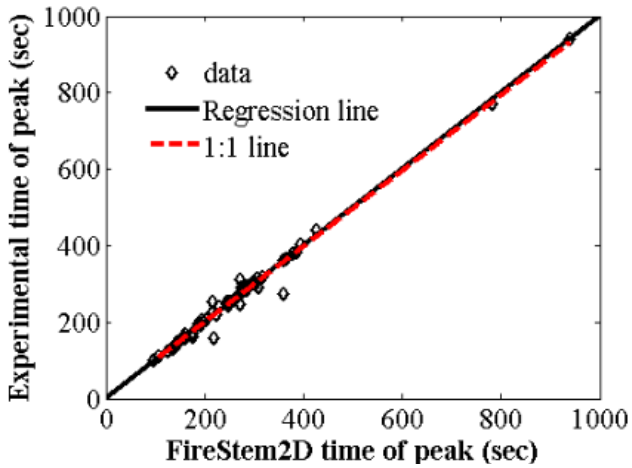

Figure 5. Scatter-plot of FireStem2D simulated versus measured peak-temperature time in all stem sections (Table 1). Dashed line marks the overall model-observation fit, solid line marks the ideal (1:1) model-observation relationship (regression line: $y=0.9885(\pm0.0355)x+1.9306(\pm10.7992)$, $R^2=0.98$). The model is not significantly different than the observations.

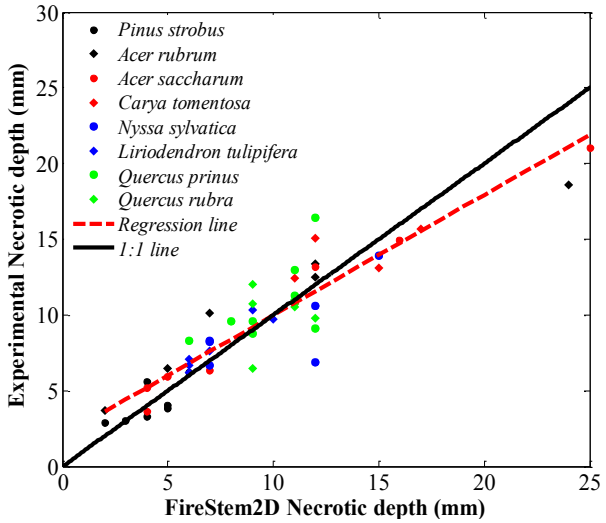

Figure 6. Scatter-plot of necrotic depth of 52 tree sections from 25 trees of 8 different species from the heating experiments (Table 1) compared with the simulated necrotic depth estimated with FireStem2D. Dashed line marks the overall model-observation fit, solid line marks the ideal (1:1) model-observation relationship (regression line y=1.051(±0.1325)x-0.6044(±1.3612), R^2=0.84). Regression line and 1:1 line are not significantly different, proving the very good prediction of necrotic depths.

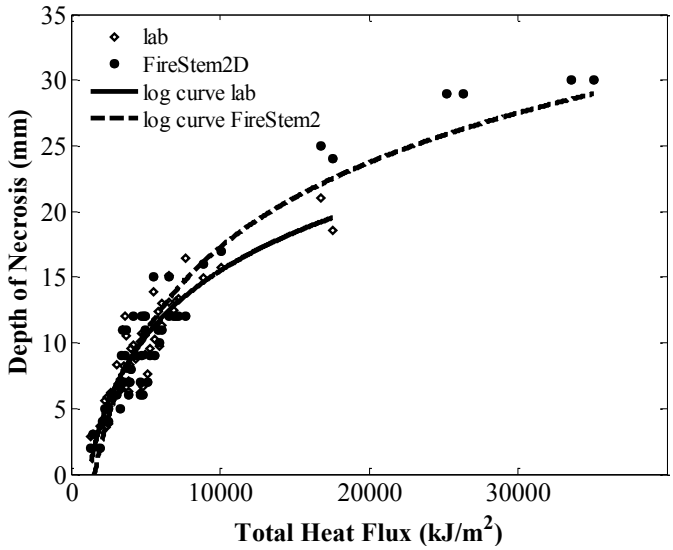

Figure 7. Depth of necrosis (mm) (y-axis) versus the measured total-energy flux integrated over time, THF in kJ/m^2 (x-axis), for all stem sections used in the lab experiments. Dashed line marks a logarithmic fit of simulation results (y=21.48(±1.89)log(x)-68.66(±7), R^2=0.93), solid line marks a logarithmic fit of observed laboratory results (y=16.63(±2.1)log(x)-51.05(±7.63), R^2=0.84). This model-driven empirical relationship can be used to extrapolate stem heating and vascular cambium necrosis beyond heat fluxes used in experimental stem heating trials.

Equations 1.17 and 1.18 imply a direct relationship between temperature variations and necrotic depth. In addition, temperature variations are related to surface heat flux. As a result there is also a direct relationship between surface heat flux and the depth of necrosis. This model-driven empirical relationship can be used to extrapolate stem heating and vascular cambium necrosis beyond heat fluxes used in experimental stem heating trials (Figure 7).

2.3.2 Sensitivity analyses

2.3.2.1 Circumferential heat distribution experiment

The experiment examines impacts of heat distribution around the tree stem to necrotic depth and its relationship with stem diameter. In our experiment, heat forcing was applied around a virtual *P. strobus* stem (same properties as previously) in five different ways described in Figure 8 and Figure 9.

The results show that cases 2, 3, and 5, the cases which heat the stem circumferentially with different intensity distributions, have greater effects than cases 1 and 4, which heat only half of the tree's circumference, at windward and leeward sides. Case 3 (3/8 of total heat at windward and leeward sides, and 1/8 at each of the other sides) has the greatest effects on the tree stem as it leaves only 79% of the tree's cross-sectional area unaffected by necrosis. However, the results in that case are only slightly different than cases 2 and 5 which leave 80% and 81% unaffected by necrosis, respectively. In this experiment we did not distinguish between sapwood and the total cross-section area. However, the model results can be used to provide specific predictions for the mortality of different critical tissues within the tree. Empirical knowledge of the depth of sapwood

relative to the total DBH exists in many species (e.g., (Bovard et al. 2005)) and could be used to predict necrosis of specifically the sapwood. Table 2 also indicates that the greater the diameter of the tree, the larger percentage of stem cross-sectional area survives and the smaller the possibility for tree mortality.

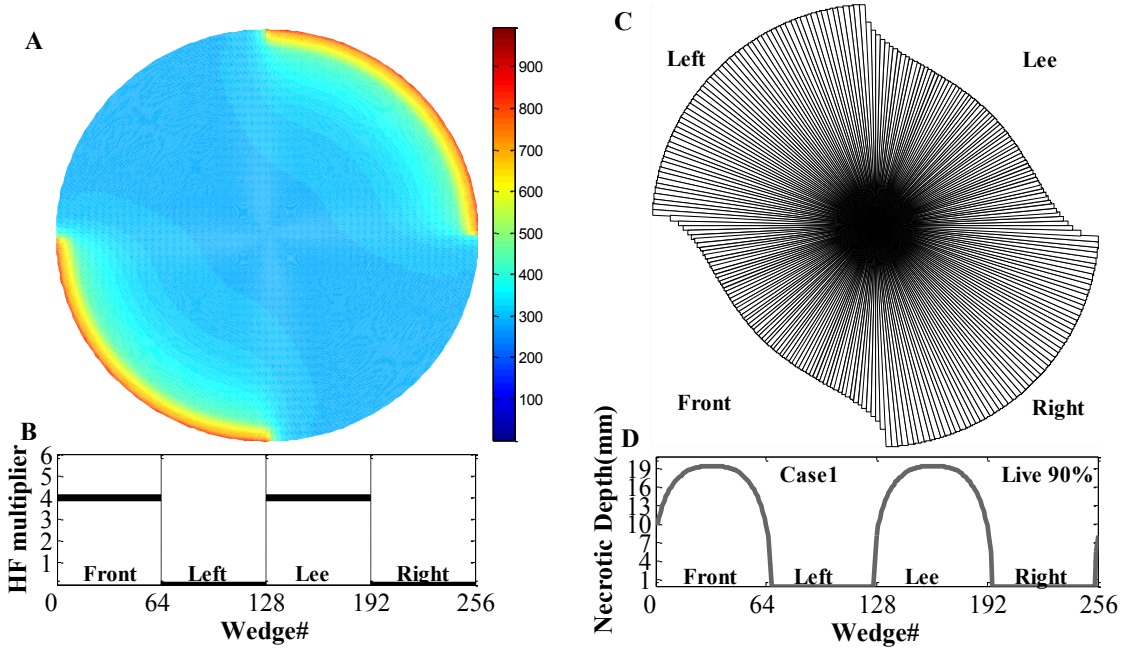

Figure 8. Forcing pattern and results for Case 1: **A.** Temperature distribution in the stem at the peak of heating process. **B.** Schematic illustration of heat forcing that was applied only to the front (upper right quadrant) and lee (lower left quadrant) sides as a plot of heat flux (HF) multiplier vs. the circumferential wedge number. The first wedge is located between 0 and 1.4 degrees from the top ("north") of the stem and wedge numbers are increased in the clockwise direction. At each wedge, the HF multiplier is applied to the circumferential mean heat-flux forcing. **C.** Remaining uninjured stem after heating. **D.** Necrotic depth of each wedge of the stem.

Tree species	Diameter (cm)	Percentage of live stem area (%)	
		Heat case 1	Heat case 2
Pinus strobus	8	31	28
	14	66	64
	24	84	84
Quercus prinus	8	46	36
	14	73	71
	24	85	84

Table 2. Percentage of live stem cross-sectional area (percentage of the tree area that remained intact after the burning experiment) for a *Pinus strobus* and a *Quercus prinus* with diameters 8, 14, and 24 cm, for simulation heat case 1 (heating only the front and lee sides of a tree section, along half of the tree's circumference), and 2 (uniform heating around the full circumference of tree stem).

2.3.2.2 Impact of height on fire effects

2.3.2.2.1 Surface fire

In the case of the *P. strobus,* the necrotic depth was almost uniform until a height of 12 m. For the *Q. prinus*, the necrotic depth was deeper than *P. strobus* (6 vs. 5 mm, respectively). It is also noted that in both cases, tree stems reach the greatest necrotic depth in less time at a height of 4 m above the ground (Figure 10a), at which point the fire temperature and radiative heat flux maximize.

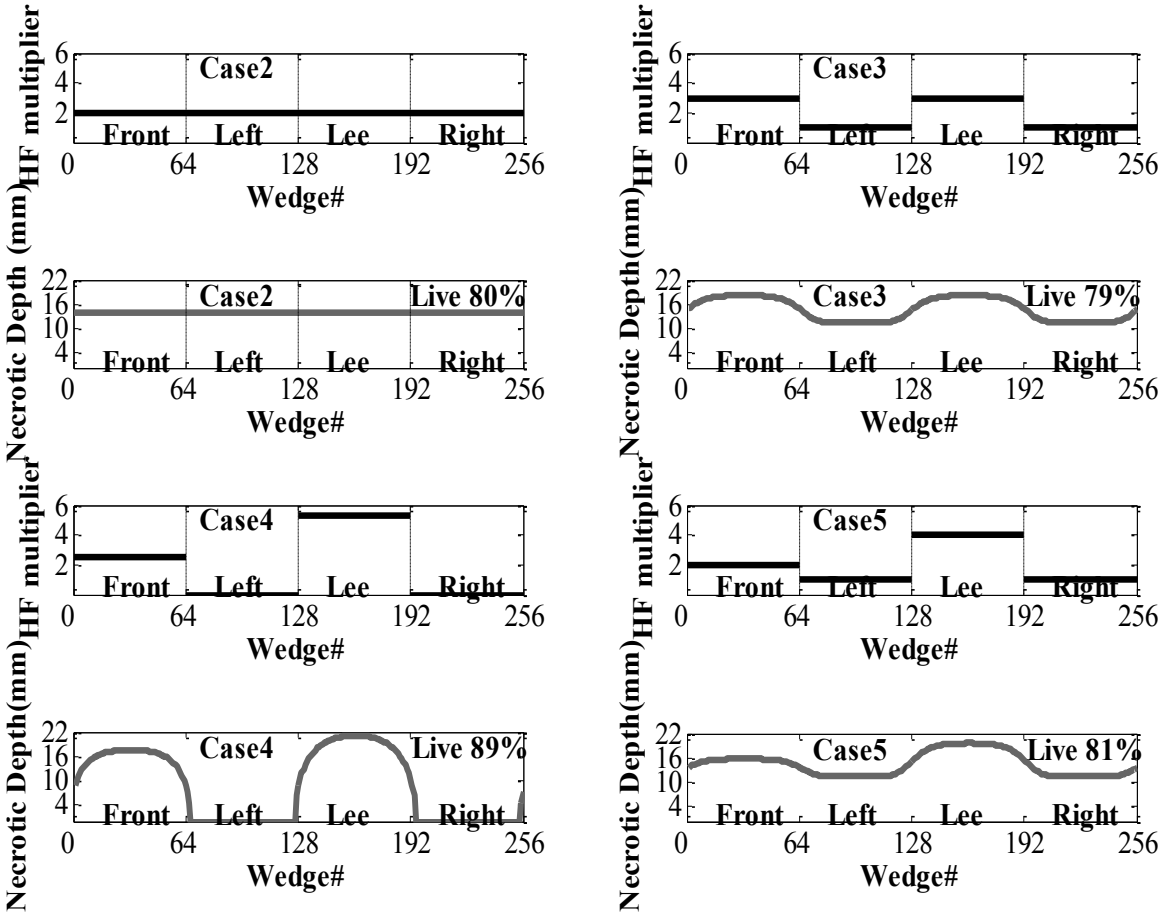

Figure 9. Forcing pattern and necrotic depth results for Cases 2-5**:** For each case, the upper panel plot shows (black line) how heat forcing was applied around the tree stem and the lower panel for the same case presents the Necrotic Depth (grey line) of each wedge of the stem. Plot layout is the same as panels B and D in figure 8. **Case 2.** Heat forcing was applied evenly around the tree stem. **Case 3.** 3/8 of heat forcing was applied at each of the front and lee side and 1/8 at each of the other sides. **Case 4.** 2.67/8 of heat forcing was applied at front side and 5.33/8 at the lee side. **Case 5.** 2/8 of heat forcing was applied at front side, 4/8 at lee side, and 1/8 at the left and right sides. Our simulation results show that different heating scenarios and heterogeneity of the heat flux around the stem can have different effects on the resulting necrosis and its potential to girdle the tree stem and lead to mortality.

2.3.2.2.2 Crown fire

Contrary to the low-intensity fire scenario, the depth of tissue necrosis increases with height for a virtual test tree (Figure 10b). In our estimation we ignored the fact that bark thickness varies inversely with height (Laasasenaho et al. 2005) to highlight the differences due to the effects of heat forcing.

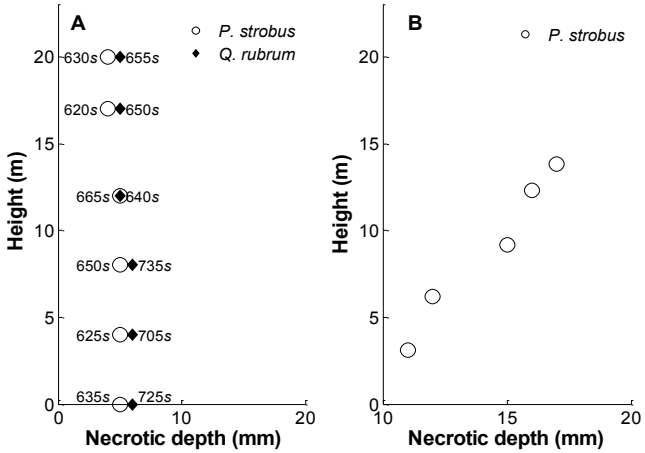

Figure 10. Simulated impact of height (above ground) on necrosis depth in two different virtual experiments: **A.** Low intensity fire: Necrotic depth at different heights: 0m, 4m, 8m, 12m, 17m, 20m for a *P. strobus* (solid markers) and a *Q. prinus* (open markers). The diagram also lists the time at which each necrotic depth was reached. In low intensity fires lower tree levels suffer strongest effects than stem parts higher in the crown. **B.** Crown Fire: Necrotic depth in different heights: 3.1m, 6.2m, 9.2m, 12.3m, 13.8m for a *P. strobus*.

2.4 Discussion

Results show that FireStem2D accurately predicts temporal variation in stem temperatures (Figure 3) and necrotic depths (Figure 6) and the time of peak temperatures in all cases (Figure 5). However, we assume that the overestimation of the temperatures

(Figure 4) is attributed to the fact that the model's 2-D structure neglects vertical vapor transport processes. As this is a 2-D model, it does not, by definition, handle three-dimensional processes such as vertical transport of heat and water. In reality, sap is transported upward during the heating, especially when the xylem temperature is very high, as evidenced by bubbling of sap at the top of the stem section, which advects heat and reduces the observed maximal temperature.

Michaletz et al. (2012) demonstrated that temperature regimes below the bark are affected by xylem water flux through a process that leads to cavitation and vessel deformation. These effects occurred at temperatures $\geq$338 K, which is higher than the threshold temperature at which tissue necrosis would occur. Although water transport processes are not included in FireStem2D, the model is well suited to provide stem temperature regimes for modeling cavitation and vessel deformation and how it might affect whole-tree heating and injury. Michaletz et al. (2012) and Butler and Dickinson (2010) suggest that a useful next step in tree heating and injury research would be consideration of the effects of heat transport by stem water flux. Significant cooling by water transport is likely to be restricted to actively transpiring trees. Furthermore, we speculate that the conditions under which such cooling is effective will be limited by the deformation and vessel collapse in the stem, because of heat-driven cavitation in foliage and thin branch vessels as a result of extreme vapor pressure deficits in the heat plume during surface fires of even moderate intensity (Kavanagh et al. 2010). We predict that cooling by water flux will be most important during low-intensity surface fires that are followed by long-term smoldering and heating at the base of tree stems (e.g., (Ryan and Frandsen 1991)). Incorporating these processes in stem-injury models is the logical next

step. However, until more is known about trees' water relations during fires, it is not clear whether the added complexity and increased simulation time needed to resolve three-dimensional heat and water transport could effectively improve stem-injury prediction accuracy.

The fact that the model is parameterized by species and not by individual tree (same W_m for all sections of same species) contributes to the error between model and observation; however, this error does not lead to a consistent bias. For example, no species is clustered above or below the model prediction line (Figure 6). The variation in temperature prediction accuracy between trees of the same species indicates that there are some differences in thermal properties between individual trees, due to either phenotypic plasticity or differences in life history. However, an individual-level parameterization would have rendered the model impractical, and the overall good agreement between the model and observation justifies the species-level parameterization.

The sensitivity analysis for the stem and necrotic depth shows the potential application of the model. Fire effects may vary around the circumference of a tree, depending on velocity of the wind. FireStem2D allows the heat from the fire to be prescribed as a dynamic time series and to vary around the stem's circumference and at different heights.

Tree death is assumed to follow deterministically if the stem is girdled and the tree does not re-sprout. Trees often survive cambial necrosis around part of their circumference. Approximately 15-20% of the cambium is needed to be intact for a tree to survive (Ducrey et al. 1996). Despite the fact that the same cases of heat forcing distributions were used in all the experiments, results varied between the species and life

stages, indicating a strong sensitivity to the thermal properties of the bark and wood (Table 2). Specifically, young *Q. prinus* (8 cm) showed roughly 25-50% deeper necrosis than young *P. strobus*. However, for large stems (24 cm) in both species the percentage of live stem did not change with different heating patterns. This indicates that using fire to maintain pine forests by removing young oak trees may be more effective in the earlier stages of forest succession when both pines and oaks are young. FireStem2D can estimate the necrotic depth at any point around the circumference of the tree stem, as well as to estimate what fraction of the total cambium was injured at different heights. This will bridge the knowledge gap between understanding of the fire heat dynamics and predicting of tree stem injury. Therefore, FireStem2D is a useful tool for wildland fire management decision support.

The use of heat-flux boundary conditions makes it possible to couple FireStem2D to a fire behavior model. Fire managers routinely use models to forecast fire behavior (Hyde et al. 2013). Several models ranging in complexity from the semi-empirical BEHAVE model (Burgan and Rothermel 1984) to the three-dimensional high resolution WFDS (Mell et al. 2007) and FIRETEC (Cassagne et al. 2011) can provide prediction of fire spread rates and intensities when weather conditions and key fuel characteristics are known. These fire behavior predictions can be used to estimate the distribution of heating intensities around a tree bole or stem, which, in turn, serve as inputs to stem injury models such as the Firestem2D model described here (Butler and Dickinson 2010). Simpler empirical assumption of fire-line heat could also be used by FireStem2D; however, to really utilize the full advantages of a 2-D model, empirical understanding of the role of wind in the heat distribution around the stem should be incorporated in the heat forcing.

FireStem2D can also be used in forecasting the effects of active wildfires if we can predict heat flux accurately, given the fuel conditions in the forest and the climate conditions expected.

FireStem2D could be broadly applied given further parameterization for the thermal parameters of other dominant tree species in different regions. The expanded applicability of FireStem2D makes it a useful tool that can be parameterized for any species and can predict necrotic depths for any species under any heat-flux conditions. In addition, the model provides a strong theoretical basis on which to extrapolate stem heating and vascular cambium necrosis beyond heat fluxes used in experimental stem heating trials (Figure 8).

Chapter 3: Resolving the Effects of Aperture and Volume Restriction of the Flow by Semi-Porous Barriers using Large-Eddy Simulations

The flow inside and around forests and cities receives growing attention. Beyond providing a challenge for fluid dynamics and atmospheric simulation, it has applications in various research areas, such as the study of the emission and dispersion of particles and volatile organic compound from forests (Bergen 1975; Prueger et al. 2008; Wolfe and Thornton 2011), the study of tree-stand stability and resistance to wind-throw (Gardiner et al. 1997; Dupont and Brunet 2006, 2008b), the study of the effectiveness of trees as wind breaks (Santiago et al. 2007), the role of buildings and street canyons on urban climate and air quality (Macdonald et al. 2002; Harman and Belcher 2006; van Hooff and Blocken 2010), and the ejection and dispersal of seeds and pollen particles from heterogeneous forests (Dupont et al. 2006; Bohrer et al. 2008; Bohrerova et al. 2009; Maurer et al. 2013). Studies of the atmospheric boundary-layer structure above forest edges (Liu et al. 1996; Patton et al. 1998; Belcher et al. 2003; Yang et al. 2006; Yue et al. 2007; Cassiani et al. 2008; Dupont and Brunet 2008a; Banerjee et al. 2013; Chamecki 2013; Fontan et al. 2013) have recognised the resemblance of a forest edge to either a forward- or a backward-facing step (depending on the wind direction relative to the forest edge) and focused on the analysis of the approaching or exiting flow fields. A feature that distinguishes forest edges

and city blocks from other barriers is that they represent a semi-porous barrier. In forests, stems, branches, and leaves restrict the open volume inside the canopy, which constitutes the step-like barrier, and produce drag on the flow; but they do not completely block the flow as a solid step would do. While air does not flow through stems or leaves, viewed at the model's grid-mesh resolution, which is typically much coarser than a leaf or a stem width, they represent a subgrid-scale (SGS) disturbance that cannot be explicitly resolved. As with forest edges, urban streets and building rows also form semi-porous barriers, but in this case the distinction between open and blocked spaces is at a coarser resolution, typically 10-50 m for buildings vs. 0.1-1 m for leaves, branches and stems of trees.

The step analogy of forest edges has been studied via analyses of field observations (Detto et al. 2008; Panferov and Sogachev 2008), data from wind-tunnel and flume experiments over artificial canopies (Seraphin and Guyenne 2008; Chamorro and Porte-Agel 2009; Markfort et al. 2010; Folkard 2011; Fontan et al. 2013), or from various model simulations (Patton et al. 2006; Dupont and Brunet 2008b, a; Paik et al. 2009; Huang et al. 2011; Schlegel et al. 2012). To date, high-resolution models of forest edges, using either the large-eddy simulation (LES) or Reynolds-averaged Navier-Stokes (RANS) model, represent forest edges as a drag term while other types of sharp transitions are represented as solid barriers using a terrain-following (sigma-Z) coordinate system or an immersed boundary condition. Typically, the effects of partial volume and aperture restriction within a semi-porous barrier are not represented. Moreover, when using a terrain-following coordinate system approach, or an immersed boundary within RANS, explicit turbulent flow inside the barrier is not allowed. Here, we use the RAMS-based Forest Large-Eddy Simulation (RAFLES) models. An important feature of this model is

the ability to represent both the effects of drag, primarily from leaf surfaces in forests and walls in urban settings, and of volume restriction in the barrier sub-domain, mostly from stems and branches in forests and the buildings themselves in an urban simulation.

The focus of our study that is published in journal of Boundary Layer Meteorology (Chatziefstratiou et al. (2014)) is to examine the features of disturbances to the flow caused by the transition from an open space to a rectangular, prism-shaped, semi-porous barrier and back to an open, unobstructed domain. We focus on the effects that are resolved by including the volume restriction as compared to a drag-only representation of the obstruction. We study those components of the streamwise mean momentum budget which are most affected by the explicit resolution of the barrier's volume and aperture. We predict that the reduced aperture will lead to a backup of the flow in the upwind edge of the barrier and will deflect the flow upward, leading to increased uplift in front of the barrier, and sideways, and leading to a sustained cross-wind velocity component. We also predict that the slow-down of the wind exiting the volume-restricted barrier into the open air will lead to strengthening of the recirculation in the downwind side of the barrier. Adjustment of the flow to the local conditions imposed by the volume and aperture may lead to changes in the turbulence divergence and advection of velocity inside and around the barrier, compared to wind-field simulations that do not resolve the volume of the barrier.

3.1 Methodology

3.1.1 Model description

RAFLES model was developed and evaluated by Bohrer et al. (2008, 2009) and explicitly resolves flow in realistic three-dimensional (3-D) heterogeneous canopies. RAFLES model is based on the Regional Atmospheric Modelling System (RAMS), a regional model that can operate as a large-eddy simulation (LES) model (Avissar et al. 1998; Avissar and Schmidt 1998) and solves the 3-D Navier–Stokes equations on a rectangular, vertically stretched grid mesh, using a quasi-hydrostatic approach and the Boussinesq approximation. The canopy in RAFLES model is represented as an explicit multi-layer, 3-D heterogeneous sub-domain where vegetation (or structure walls in an urban "canopy") exchanges drag, and latent and sensible heat with the air flowing through the canopy sub-domain (Bohrer et al. 2007). In LES, variables are decomposed into two components: a resolved (mean, box-filtered) component, marked by an overbar, and the SGS perturbations from that mean, marked by a prime. By partitioning the components of the semi-compressible Navier–Stokes variables into resolved and SGS the prognostic equation for the resolved scale velocity written in Einstein notation becomes,

$$\frac{\partial \overline{u_i}}{\partial t}+\frac{1}{\rho_o}\left[-\frac{\overline{u_i}\partial\left(\rho_o \overline{u_j}\right)}{\partial x_j}+\frac{\partial\left(\rho_o \overline{u_i}\,\overline{u_j}\right)}{\partial x_j}+\frac{\partial\left(\rho_o \overline{u_i' u_j'}\right)}{\partial x_j}\right]=\delta_{i3} g \frac{\overline{\theta_{vp}}}{\theta_{vo}}-\theta_o\left(\frac{\partial \overline{\pi}}{\partial x_i}\right)+F\left(\overline{u_i}\right)+D_i\left(\overline{V}\right), \qquad (3.1)$$

where $\overline{u}$ is the resolved wind velocity component , ρ_o is the air density , t is time, g is the acceleration due to gravity, δ is the Kronecker delta, θ_{vp} is the virtual potential temperature (K), θ_{vo} is a reference virtual potential temperature (K) used at the model initialization,

horizontally homogeneous and constant in time, and π is the pressure expressed in terms of the Exner function (Klemp and Wilhelmson 1978),

$$\frac{\partial \bar{\pi}}{\partial t} = \frac{\left(c_s \min(1, \frac{0.95\Delta x}{4 c_s \Delta t}) \right)^2}{\rho_0 \theta_0^2} \frac{\partial (\rho_0 \theta_0 \overline{u_j})}{\partial x_j}, \qquad (3.2)$$

In Equation 1 $F\left(\overline{u_i}\right)$ represents the sum per unit mass of horizontal wind forcing through the domain (N kg^{-1}), which forcing is comprised of Rayleigh friction as a boundary condition at the top layers of the model and a Newtonian nudging term, applied high above ground. $D_i\left(\overline{V}\right)$ represents the components of the barrier drag force per unit mass (N kg^{-1}) that is a function of the resolved-scale velocity.

The formulation of the SGS turbulent kinetic energy (TKE), $\bar{e} = \overline{u_i' u_i'} / 2$, is based on Deardorff, (1980):

$$\frac{\partial \bar{e}}{\partial t} + \frac{\partial \left(\rho_o \overline{u_j}\right)}{\rho_o \partial x_j} - \frac{\bar{e}}{\rho_o} \frac{\partial \left(\rho_o \overline{u_j}\right)}{\partial x_j} = \frac{g}{\overline{\theta_v}} 0.3 l_\varepsilon e^{-1/2} \left(1 + 0.61 \bar{q} \frac{\partial \overline{\theta_l}}{\partial z} + 0.61 \bar{\theta} \frac{\partial \bar{q}}{\partial z} \right)$$

$$- \left(K_m \left(\frac{\partial \overline{u_i}}{\partial x_j} + \frac{\partial \overline{u_j}}{\partial x_i} \right) + \frac{2}{3} \delta_{ij} \bar{e} \right) \frac{\partial u_i}{\partial x_j} - \frac{\partial}{\partial x_i} \left(-2 K_m \frac{\partial \bar{e}}{\partial x_i} \right) - \frac{8}{3} C_{dl} A_l \left| \overline{V} \right| \bar{e} - \frac{0.7 e^{-3/2}}{3 l_\varepsilon}, \qquad (3.3)$$

where K_m is the momentum eddy diffusivity defined as $K_m = 0.1 l_\varepsilon e^{-1/2}$, where l_ε is an empirical length scale for mesh size and dissipation defined in Bohrer et al. (2009) and

based on Deardorff (1980). The first term on the right-hand side is a buoyancy production or consumption term, which is positive when the heat flux is positive and negative otherwise; the second term on the right-hand side is the shear production or consumption term, the fourth term represents the contribution of the barrier to the drag on SGS motion (Shaw and Patton 2003), and the fifth term accounts for the viscous dissipation of TKE and is formulated as in Bohrer et al. (2009).

The RAFLES model uses a cut-cell coordinate-system approach for finite-volume discretization (Adcroft et al. 1997; Walko and Avissar 2008). By applying the Gauss divergence theorem for a vector field $\vec{F}$, the control-volume integrals of the gradient of a vector quantity can be transformed into surface integrals as follows,

$$\int_{\Psi} \nabla \cdot \vec{F} \, d\Psi = \int_{\sigma} \vec{F} \cdot \vec{n} \, d\sigma - \int_{\sigma} \vec{F} \cdot \vec{n} \, d\sigma = \sum_{i=1}^{3} \frac{\dot{\Delta}(\sigma_i F_i)}{\Psi}, \qquad (3.4)$$

where Ψ is the open volume of the computational cell (the control volume), $\vec{n} = (n_1,\ n_2,\ n_3)$ are the unit normal vectors, and $\sigma_1,\ \sigma_2,\ \sigma_3$, are the aperture areas normal to the *x*, *y* and *z* directions, respectively. The aperture area σ represents the common area between two adjacent cells through which flow passes. The operator $\dot{\Delta}(\ )$ represents a discrete numerical difference between terms that were evaluated at two subsequent parallel apertures.

RAFLES model uses a split-time leapfrog discretization scheme (Haltiner and Williams 1980) that allows different terms of the equation to be integrated at different

timestep intervals, indicated in Equation 3.5 below by the superscript (*t*). The pressure gradient term is integrated over small (dissipation) timestep intervals $\Delta t_s = \Delta t / N_{ts}$ that are smaller than the longer timestep Δt; $N_{ts} \geq 1$ is the integer number of small time-steps within each longer timestep Δt; An intermediate timestep, $\Delta t_m = m\Delta t_s \leq \Delta_t$, where *m* is an integer, is applied to the advection and the turbulent tendency terms. RAFLES model uses the Arakawa and Lamb (1977) type C staggered grid scheme. Combining the parametrization for SGS TKE (Equation 3.3) the cut-cell coordinate system (Equation 3.4) and a leap-frog time discretization with the momentum equation (Equation 3.1), the space- and time-discretized numerical form is obtained,

$$\frac{\overline{u_i}^{(t+1)} - \overline{u_i}^{(t-1)}}{2\Delta t}$$

$$+ \frac{M}{N_{ts}} \sum_{m=1}^{N_{ts}/M} \left[\frac{\dot{\Delta}_j}{\rho_o \Psi} \left(\left(\rho_o \sigma_j \overline{u_i} \overline{u_j} \right) - \overline{u_i} \left(\rho_o \sigma_j \overline{u_j} \right) - \rho_o \sigma_j K_m \left(\frac{\Delta \overline{u_i}}{\Delta x_j} + \frac{\Delta \overline{u_j}}{\Delta x_i} \right) + \rho_o \sigma_j \frac{2}{3} \delta_{ij} \bar{e} \right)^{t-1+m\Delta t_m} \right]$$

$$= F\left(\overline{u_i}\right)^{(t)} + D_i\left(\overline{V}\right)^{(t)} + \delta_{i3} g \frac{\overline{\theta_{vp}}^{(t)}}{\theta_{vo}} - \frac{\theta_o}{N_{ts}} \sum_{n=1}^{N_{ts}} \left[\left(\frac{\Delta \bar{\pi}_p}{\Delta x_i} \right)^{(t-1+n+\Delta t_s)} - \frac{\Delta \overline{\pi_g}}{\Delta x_i} \right], \qquad (3.5)$$

Similar discretization is applied to the TKE and Exner function equations.

3.1.2 Cut-Cell Formulation of Barriers

The finite volume discretization method used in Equation 3.1 introduces four additional variables in the discretized momentum equation (Equation 3.5) – the open cell

volume and three open apertures areas that need to be defined. The volume of each mesh-grid cell is reduced by an amount equal to the barrier volume within the cell. Similarly, the open aperture areas on the cell faces are reduced by an amount equal to the projected barrier area in the direction of each cell face. The cut-cell method was originally developed to represent topography and large solid barriers that have SGS components due to the mismatch between the barrier structure and the mesh-grid discretization.

To represent semi-porous barriers we assume that for each cell that is obstructed by the barrier there is some reduction in the open apertures and volume, σ and Ψ, but not a complete restriction. Figure 11 illustrates a tree as an analogy to a semi-porous barrier. Wherever a solid element (e.g., tree stems, buildings or arbitrary rods) partially obstructs a grid-cell, the projection of the area of that stem on the grid face, σ, is reduced leading to a proportional reduction in any flux across that face. In the horizontal direction ($i = (1, 2)$; $i \neq j$):

$$\sigma_i = \Delta x_j \Delta x_3 - 2\int_{x_3-0.5\Delta x_3}^{x_3+0.5} r_{x_3}\, dx_3, \qquad (3.6)$$

which simplifies in the case of a vertically constant radius (as assume here) to $2r\Delta x_3$. In the vertical direction ($i = 3$):

$$\sigma_i = \Delta x_1 \Delta x_2 - \max\left|\pi r_{x_3}^2\right|_{x_3-0.5\Delta x_3}^{x_3+0.5\Delta x_3}, \qquad (3.7)$$

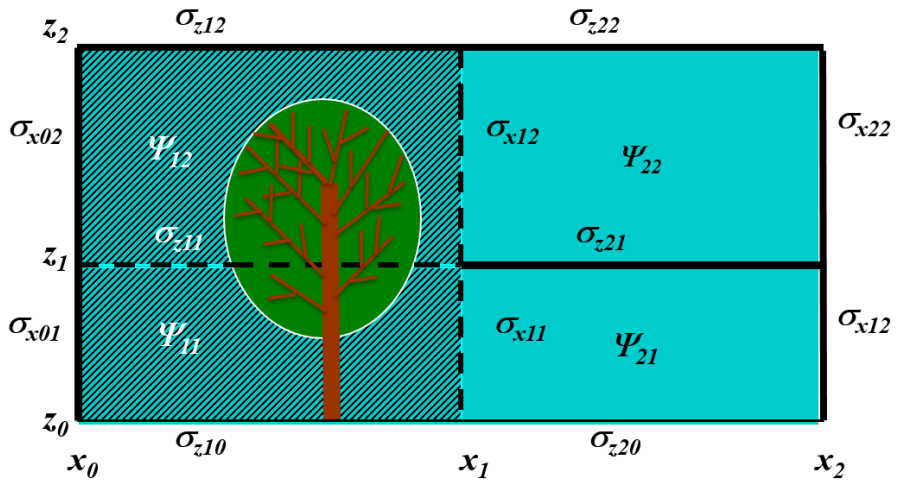

Figure 11. The cut-cell method: semi-porous barrier representation. Control volumes are labelled with Ψ and the corresponding control surfaces with σ. Ψ_{22} and Ψ_{21} represent the control volume of unobstructed cells. Ψ_{11}, Ψ_{12} are reduced by an amount equal to the obstructing vegetation volume portion represented in brown and green (for stem and branches, and leaves, respectively) in the corresponding grid cell. The apertures at the grid surface interfaces are also reduced such that: $0 = \sigma_{x11} < \sigma_{x12} < \sigma_{x01} = \sigma_{x21} < \sigma_{x20} = \sigma_{x22} = \Delta y \Delta z$ in the streamwise direction and $0 = \sigma_{z10} = \sigma_{z20} < \sigma_{z11} < \sigma_{z21} = \sigma_{z12} = \sigma_{z22} = \Delta y \Delta x$ in the vertical direction. Flow through the blocked apertures σ_{z10}, $\sigma_{z20,}$ is totally restricted, through the fully open apertures σ_{x01}, σ_{x21}, σ_{x02}, σ_{x22}, σ_{z21}, σ_{z12}, σ_{z22}, is totally unrestricted and is partially restricted for all other apertures.

The resulting reduced open volume of the obstructed grid-cell, Ψ, is,

$$\Psi = \Delta x_1 \Delta x_2 \Delta x_3 - 3.14 \int r_{x_3}^2 dx_3 = 3.14 r^2 \Delta x_3, \qquad (3.8)$$

where r_{x_3} is the vertical profile of the radius of the obstructing object in the cell, assumed here to represent a cylinder with a vertically constant radius, i.e. $r_{x_3} = r$. The obstacle-induced face reduction is considered uniform over the face, as if regulated by a Venetian blind. Similarly, the volume reduction of a cell that contains an obstacle is assumed to be uniform within the cell.

3.1.3 Barrier Structure and Drag

We simulated barriers with highly simplified shapes. In RAFLES model, barriers were originally designed to represent forests and can exert drag, exchange water vapour, heat and CO_2 with the atmosphere, in addition to the volume and aperture reduction. In this experiment, we assumed that the barrier is composed of vertical cylinders, using the RAFLES model machinery for tree stems without taper and without leaves. The drag force per unit air mass that each element in the barrier, D_w, exerts on the flow is expressed as,

$$D_{wi} = \begin{cases} -C_{dl}\left(\dfrac{\pi\left(\Delta x_i \Delta x_3 - \sigma_j\right)}{\Psi}\right)\left|\overline{V}\right|\overline{u_i} & i=(1,2); j=(1,2); i \neq j \\ -C_{dl}\left(\dfrac{\pi}{2}\dfrac{\sum\left(\Delta x_i \Delta x_j - \sigma_j\right)}{\Psi}\right)\left|\overline{V}\right|\overline{u_i} & i=3; j=(1,2) \end{cases} \quad (3.9)$$

where $\left|\overline{V}\right|$ is the wind speed, $C_{dl} = 0.15 + 1.328R_1^{-0.5}$ (Shaw and Patton 2003) is the skin drag coefficient for the barrier (and, here, chosen at a typical value for vegetation), R_1 is the drag-generating object's Reynolds number. The barrier's drag-generating surface area is calculated in Equation 3.8 from the difference between the grid-cell edge size, $\Delta x_i \Delta x_j$ and the open aperture of that edge, σ_j.

3.1.4 Boundary, Initial Conditions, and Experimental Set-up

Periodic boundary conditions are applied at the lateral domain edges and Rayleigh friction is applied to the upper five grid levels to reduce reflection at the top boundary.

Free-slip conditions for the horizontal velocity and zero vertical velocity are assumed at the bottom boundary, while surface momentum fluxes due to the soil friction are imposed through the drag term at the bottom boundary for the three velocity components.

The model is initialized using horizontally homogeneous and vertically detailed profiles of air pressure, potential temperature, humidity, air density and the horizontal components of wind velocity. Initial profiles are based on similarity theory up to the neutrally mixed boundary-layer top (assumed here at 200 m above the ground) with horizontal wind forcing using Newtonian nudging of the domain-wise mean wind speed above this layer, prescribed at 1 m s^{-1} for the low-wind cases and at 5 m s^{-1} for the high-wind cases (table 3). The initial vertical component of wind velocity is set to zero and the initial SGS TKE is set equal to the minimum value of 0.0005 m^2 s^{-2}. Surface latent and sensible heat fluxes are not prescribed, corresponding with neutrally buoyant boundary-layer conditions. For this project we set the model timestep Δt_s = 0.02 s, with the greater nested timesteps defined by N_{ts} = 8 and m = 4.

The model domain for the present experiment was set to 0.5 x 0.5 x 1.4 km^3 resulting in 100 x 100 x 95 grid points; the horizontal grid resolution is 5 x 5 m^2 and the vertical grid resolution is 3 m between the ground and z = 100 m. Above this height a 20% vertical stretching is applied for each consecutive vertical layer up to a maximum grid spacing of 30 m.

Case Label	Drag generating area density (m^2 drag area/m^3air)	Simulation type	Stem radius (m)	Aperture $\frac{\sigma_x}{\Delta y \Delta z}$	%Volume blockage $100\frac{\Delta x \Delta y \Delta z - \Psi}{\Delta x \Delta y \Delta z}$	Newtonian nudging of wind above 200 m /Shear velocity
DragSparse (Low velocity)	0.04π	Drag only	0.5	1	0	1/0.024
DragDense (Low velocity)	0.1608π	Drag only	2	1	0	1/0.024
ContSparse (Low velocity)	0.042π	Control	0.5	4/5	3.1420	1/0.024
ContDense (Low velocity)	0.1608π	Control	2	1/5	50.380	1/0.024
DragSparse (High velocity)	0.042π	Drag only	0.5	1	0	5/0.184
DragDense (High velocity)	0.1608π	Drag only	2	1	0	5/0.184
ContSparse (High velocity)	0.042π	Control	0.5	4/5	3.1420	5/0.184
ContDense (High velocity)	0.1608π	Control	2	1/5	50.380	5/0.184
RestSparse (High velocity)	0	Restriction only	0.5	4/5	3.1420	5/0.184
RestDense (High velocity)	0	Restriction only	2	1/5	50.380	5/0.184

Table 3: Ten cases were simulated. The simulation time in all cases was set to 12 hours, which allowed the simulation to reach a quasi-stationary stage.

The barrier is represented by a block of 27 m in height (*h*), 125 m in width and 125 m in length containing 25 x 25 SGS "cylinders" (one per column of model cells). In

their SGS representation, these cylinders are, in fact, assumed to be equally spaced within the barrier and do not have an actual resolved shape within each grid-cell. This set up results in homogeneous volume and aperture reductions for all the grid-cells within the barrier sub-domain and symmetry between the horizontal faces, i.e. $\sigma_x = \sigma_y$. We chose a rectangular prism-shaped barrier; this shape is typical of a vegetated patch in a savannah, in a remnant forest surrounded by agricultural landscape, or a surviving forest patch after a strong fire. With a much higher density of the barrier, such a shape can also represent a small collection of buildings. As this investigation focuses on the effects of the representation of the volume of the semi-porous barrier, a prism-shaped barrier provides the opportunity to discuss effects in all three directions. However, other barrier shapes, such as a forest strip (wind-break), a linear gap in a continuous forest or a forward or backward-facing step may provide interesting cases, and though not directly evaluated in this work could be resolved using our model.

We present ten simulation cases, the characteristics of which are listed in Table 2. We tested two types of barriers, one sparse and one dense; the dense barrier had a larger portion of blocked space. We assumed the diameter of the virtual SGS cylinders that form the barrier elements within each pixel increased in the dense barrier, relative to the sparse one, and calculated the corresponding increase in its surface area, causing a corresponding increase in drag. Our sparse case is equivalent to the middle case of Poggi et al. (2004) and thus corresponds with a sparse canopy, since the densest case in Poggi et al. (2004) is comparable to a dense canopy. Our dense case set-up corresponds with a dense built-up area in a residential low-rising city block (Bohnenstengel et al. 2011). For each case, we also tested a drag-only equivalent, where we prescribed the same barrier-induced drag-

generating surface areas and forcing conditions but ignored the barrier volume by prescribing all apertures and volumes to be fully open. We tested each case under low (1 m s^{-1}) and high (5 m s^{-1}) wind-speed components above the canopy. We also tested two cases (sparse and dense under high wind) with only volume and aperture closure and without drag, by assuming a surface drag coefficient of zero. Simulations ran for 12 h to achieve a quasi-stationary state. In cases forced by high wind speeds the results reached a semi-stationary solution rather quickly and the averages of the last 30 min where used for analysis. We ran simulations forced by weaker winds for an additional hour to allow convergence of the mean and used the mean of the last 90 min for analysis.

3.1.5 Analysis of Simulation Results

The resolved covariance of the wind-speed components was calculated for each point in the simulation domain by calculating the point-perturbation from the instantaneous horizontal mean of the velocity component. These were further averaged in time, using data from 900 or 2700 snapshots saved every 2 sec during the last 30 or 90 min of the simulation (high or low wind-speed cases, respectively). For example, w_t, is the 30- or 90-min average of $\overline{w}$ (the instantaneous, resolved grid-scale vertical wind component) at each grid point and timestep and $\left(\hat{w}\right)''$ is the 30- or 90-min average (marked by the double overbar) of the perturbation of $\overline{w}$ (the instantaneous, resolved grid-scale vertical wind component) at each grid point and timestep from the horizontal mean of the vertical velocity at the same height and timestep, $\hat{w}$, and $\sigma_w = \left(\overline{\overline{\left(\left(\hat{w}\right)'\left(\hat{w}\right)'\right)}}\right)^{0.5}$

marks the 30- or 90-min standard deviation of the vertical velocity perturbations. Similar notation applies to the *u* and *v* components of velocity and the momentum flux *uw*.)

Total TKE was calculated as $\hat{e} = 0.5 \cdot \left(\sigma_w^{\,2} + \sigma_u^{\,2} + \sigma_v^{\,2}\right) + \overline{\overline{(e)}}$.

3.2 Evaluation of the effects of aperture and volume restriction of the flow by barriers

3.2.1 Barrier effects on vertical and horizontal velocity components in the streamwise direction

In all high velocity cases we observe persistent uplift zones upwind of the barrier that become particularly strong ≈ 2*h* (54 m) upwind of the barrier's forward-facing edge (Figure 12a, 12b, 12e, 12f). These persistent uplift zones are always stronger in control cases (Figure 12c, 12g) than in drag-only cases. At the downwind edge of the barrier the flow is especially turbulent and becomes detached from the barrier surface. A lee-side uplift is formed at the downwind edge of the barrier that is always followed by a downward flow, forming together a recirculation zone that is again more intense in the control cases (Figure 12c, 12g). As a result of the stronger recirculation zone at the control cases, the streamwise wind-speed component (u_1 component, i = 1) is higher in the uplift region and lower in the downward part compared to the corresponding drag-only cases (Figure 12d, 12h). Both streamwise and vertical wind-velocity components contribute to the relative strengthening of the recirculation zones in control cases.

Although we do not observe strong persistent uplift zones in low velocity cases (Figure 13), the comparison of corresponding control and drag-only cases (Figure 13c, 13g) shows that control cases have stronger recirculation zones at the same positions as in high

velocity cases. In addition, the differences in streamwise wind speed between drag-only and control cases, (Figure 13d, 13h) show similar behavior to the high velocity cases, being higher at the downwind edge in the control cases and lower a few meters after.

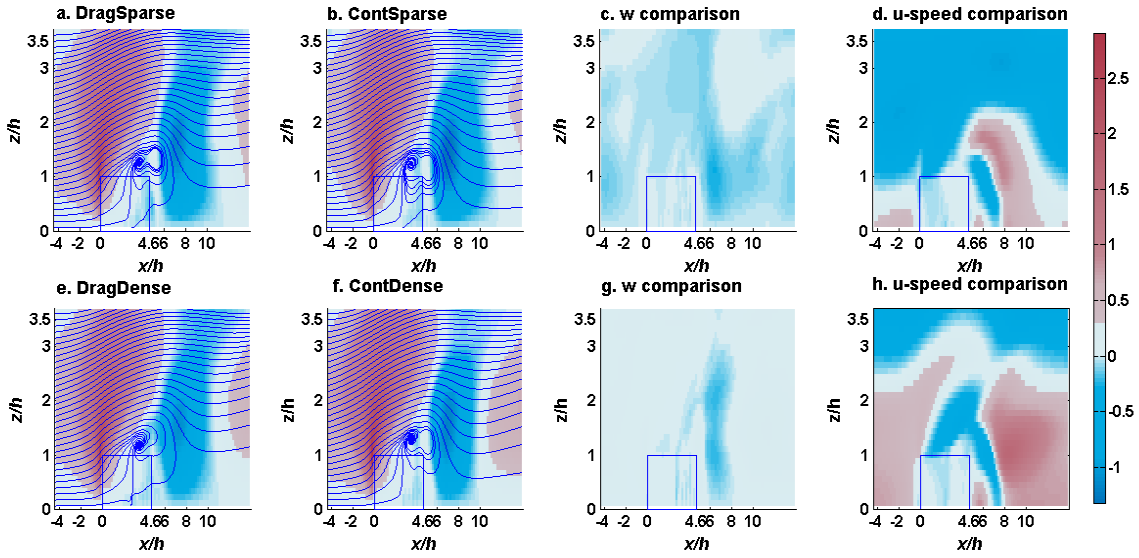

Figure 12. High velocity cases - Upper panels: Sparse cases, lower panels: Dense cases. The color represents: **a.** Sparse, drag-only case: normalized vertical wind velocity, averaged through the cross-wind side of the barrier, w_t / u_*, **b.** Sparse, control case: w_t / u_{**}, **c.** Differences of w_t / u_* between sparse cases (control - drag-only), **d.** Differences of normalized horizontal wind speed between sparse cases (control - drag-only), averaged through the crosswind side of the barrier $u-speed_t / u_*$, **e.** Dense, drag-only case: normalized vertical wind velocity, averaged through the cross-wind side of the barrier, w_t / u_*, **f.** Dense, control case: w_t / u_*, **g.** Differences of w_t / u_* between dense cases (control - drag-only), **h.** Differences of normalized streamwise wind speed ($u-speed_t$) between dense cases (control - drag-only), averaged through the cross-wind side of the barrier, $u-speed_t / u_*$. Blue continuous lines depict the streamlines. Labels and setup for all cases are described in table 3. Upwind uplift zones (red areas) and recirculation zones (white & blue areas downwind of barrier) are stronger in control cases. A separation region occurred on the downwind edge of the barrier.

Volume-restriction-only simulations, in which drag effects on the flow were neglected (Figure 14), provide further insight in the effects of volume restriction. In these cases, we still observe an uplift zone at the upwind edge of the barriers followed by downward flow past the downwind edge of the barrier. These findings support our initial assumption that both drag and volume restriction play an important role in the formation of the uplift and recirculation zones.

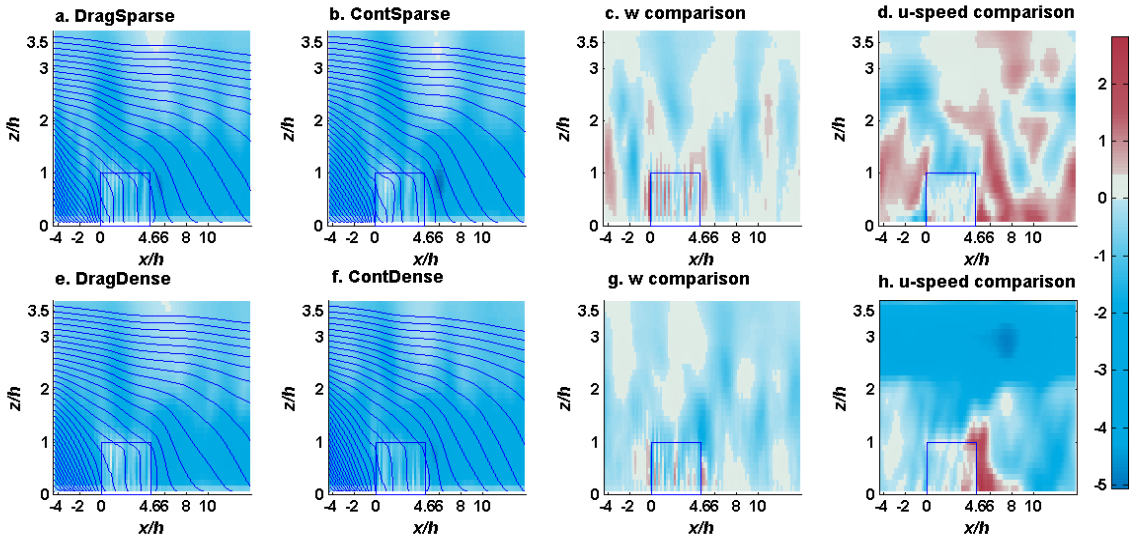

Figure 13. Low velocity cases - Upper panels: Sparse cases, lower panels: Dense cases. The color represents: **a.** Sparse, drag-only case: normalized vertical wind velocity, averaged through the cross-wind side of the barrier, w_t/u_*, **b.** Sparse, control case: w_t/u_{**}, **c.** Differences of w_t/u_* between sparse cases (control - drag-only), **d.** Differences of normalized horizontal wind speed between sparse cases (control - drag-only), averaged through the crosswind side of the barrier $u-speed_t/u_*$, **e.** Dense, drag-only case: normalized vertical wind velocity, averaged through the cross-wind side of the barrier, w_t/u_*, **f.** Dense, control case: w_t/u_*, **g.** Differences of w_t/u_* between dense cases (control - drag-only), **h.** Differences of normalized streamwise wind speed ($u-speed_t$) between dense cases (control - drag-only), averaged through the cross-wind side of the barrier, $u-speed_t/u_*$. Blue continues lines depict the streamlines. Labels and setup for all cases are described in table 3. Upwind uplift zones (red areas) and recirculation zones (white & blue areas downwind of barrier) are stronger in control cases. A separation region occurred on the downwind edge of the barrier.

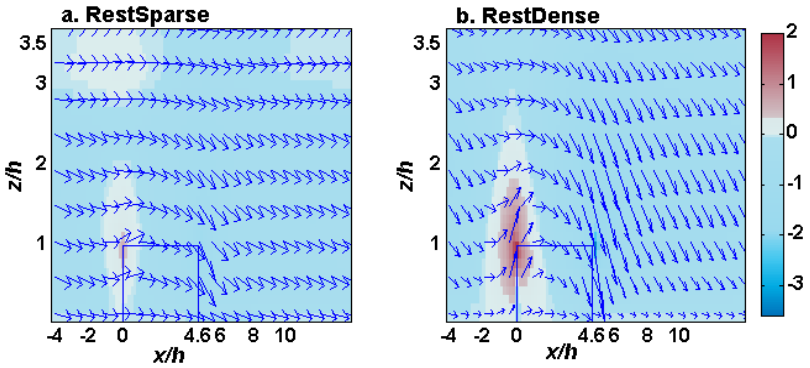

Figure 14. High velocity cases, Restriction-only (no drag) cases – The color represents the normalized vertical wind speed averaged through the crosswind side of the barrier, w_t/u_*. Arrows represent the direction of the wind and they are 10 times exaggerated in the vertical direction. Labels and setup for all cases are described in table 3. In no-drag cases we still observe an uplift zone at the upwind edge of the barriers and a weak recirculation zone past the downwind edge of the canopy.

Next, we investigated the adjustment region of the flow in the barrier. According to Belcher et al. (2003), the length of the adjustment region can be defined as the distance required by the flow to be in equilibrium with the canopy. Consistent with this, we define the adjustment zone as the length from the beginning of the barrier up to the first pixel where the mean vertical velocity just below the barrier top has vanished (i.e., $w_t/F < 0.01$)

(Dupont and Brunet 2008a). For high velocity cases (Figure 12) the length of the adjustment zone is roughly 40 m. For the low velocity cases (Figure 13) the length of the adjustment zone is negligible and the flow adjusted within a single pixel (5 m). We do not observe any differences among cases with the same velocity regarding the length of the adjustment zone. However, both in the low and high velocity cases, the streamwise velocity component past the adjustment length (Figure 12d, 12h and 13d, 13h) is lower in the entry region and higher in the exit region at the upper levels of the barrier in control cases. This implies that the flow in the control cases adjusts more rapidly to the density changes than in the drag-only cases.

3.2.2 Barrier effects on the vertical and horizontal velocity components in the cross-stream direction

Considering the effects of the barrier in the cross-stream direction for high velocity cases, our results showed two almost symmetrical circulation zones at the side edges of the barrier (Figure 15a). The intensity of the uplift associated with these circulation zones is much lower than that in the streamwise direction. The vertical and the cross-wind velocity components inside the barrier are very small (w_t/F < 0.01 or equivalently $w_t / u_* < 0.03$), and thus the edge effects are negligible and the flow parallel to the side walls adjusts almost immediately to the flow regime inside the barrier.

The existence of the barrier also affects the horizontal cross-wind velocity component (v_t). In the high velocity cases, $v_t \approx 0$ ($v_t / u_* < 0.03$) inside the barrier (Figure 15b) except for the 5 - 6 pixels (25 - 30 m) closest to edges of the barrier (where $-1 < v_t / u_* < 1$). The circulation in opposite directions controls v_t around the corners of the barrier.

Exactly downstream of the barrier we notice a divergence region for almost 50 m and thereafter the flow converges. The lateral edge effects in low velocity cases are smaller than in the high velocity cases and we do not present them here. To be on the safe side and eliminate potential edge effects in the analysis of our results, we excluded eight pixels (40 m) of each lateral side (near the side walls, parallel to streamwise axis) for all the cases when we analyze the mean flow patterns through the barrier in the streamwise direction.

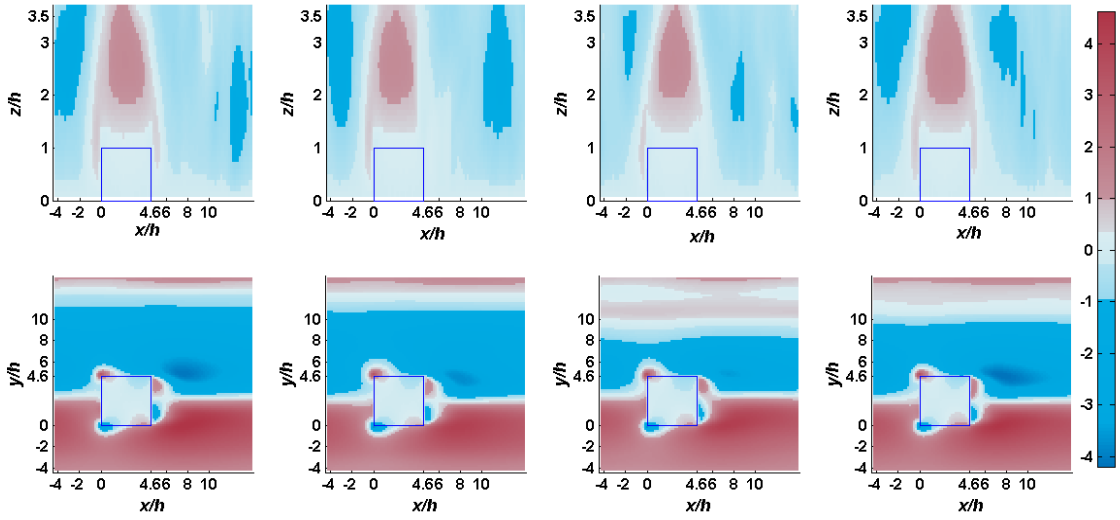

Figure 15. High velocity cases – The color represents: **a.** Normalized vertical wind velocity at *y*-*z* plane averaged through the streamwise side of the barrier, w_t / u_*. Panels from left to right: sparse drag-only case, dense drag-only case, sparse control case, dense control case. **b.** Normalized cross-wind wind velocity at *y*-*z* plane averaged throughout the streamwise side of the barrier, v_t / u_*. Panels from left to right: sparse drag-only case, dense drag-only case, sparse control case, dense control case. Labels and setup for all cases are described in table 3.The edge effects at *y*-*z* plane are not significant.

3.2.3 Barrier effects on turbulence, pressure gradient and advective sources of momentum

To further investigate the mechanisms through which resolving the volume affects the simulation results we divided the momentum sources in the streamwise momentum equation (i = 1 in Equation 1) to three components: turbulence divergence (Φ_{x_turb}), pressure gradient (Φ_{x_pres}), and momentum advection (Φ_{x_adv}). The three terms are calculated as follows,

$$\Phi_{x_turb} = \frac{\overline{\overline{\partial\left(\left(\hat{u}\right)'\left(\hat{u}\right)'\right)}}}{\partial x} + \frac{\overline{\overline{\partial\left(\left(\hat{u}\right)'\left(\hat{v}\right)'\right)}}}{\partial y} + \frac{\overline{\overline{\partial\left(\left(\hat{u}\right)'\left(\hat{w}\right)'\right)}}}{\partial z}, \qquad (3.10)$$

$$\Phi_{x_pres} = \frac{\overline{\overline{\partial P_t}}}{\rho_0 \partial x}, \qquad (3.11)$$

$$\Phi_{x_adv} = \overline{\overline{u_t \frac{\partial u_t}{\partial x} + v_t \frac{\partial u_t}{\partial y} + w_t \frac{\partial u_t}{\partial z}}}, \qquad (3.12)$$

where P_t is the resolved-scale pressure perturbation from the horizontal mean that was calculated from the instantaneous Exner function, and for convenience we denote the explicit streamwise, cross-wind and vertical coordinates as x, y and z instead of x_1, x_2 and x_3 (respectively).

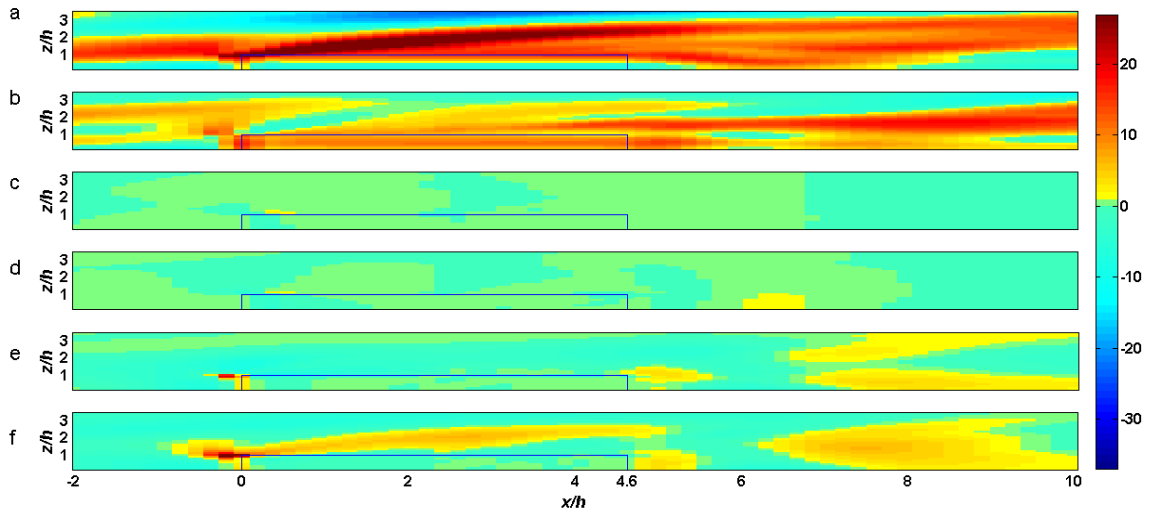

Figure 16. High velocity cases **-** Comparison of spatial variation of the streamwise momentum source terms, averaged through the crosswind side of the barrier. Difference of turbulence divergence between control and drag-only sparse cases (a), dense cases (b). Difference of pressure gradient terms between control and drag-only sparse cases (c), dense cases (d), Difference of advective terms between control and drag-only sparse cases (e), dense cases (f). All terms are normalized with u_*^2 / h .

In the high velocity cases (Figure 16), the comparison of control cases to the respective drag-only cases shows that the turbulence term encompasses the most extreme differences between cases. This is particularly the case in the uplift zones where turbulence divergence generated by the volume and aperture restriction plays the most important role in generating differences in mean streamwise momentum between the cases (Figure 16a, 16b). Pressure gradient and momentum advection are mostly responsible of forming the recirculation zone downwind of the barrier (Figure 16c - 16f). Again, the comparison between corresponding cases shows that the recirculation zones are more intense in the cases where both volume restriction and drag are prescribed (control cases). In the low

velocity cases (Figure 17), as expected, the differences between cases are smaller and less spatially consistent.

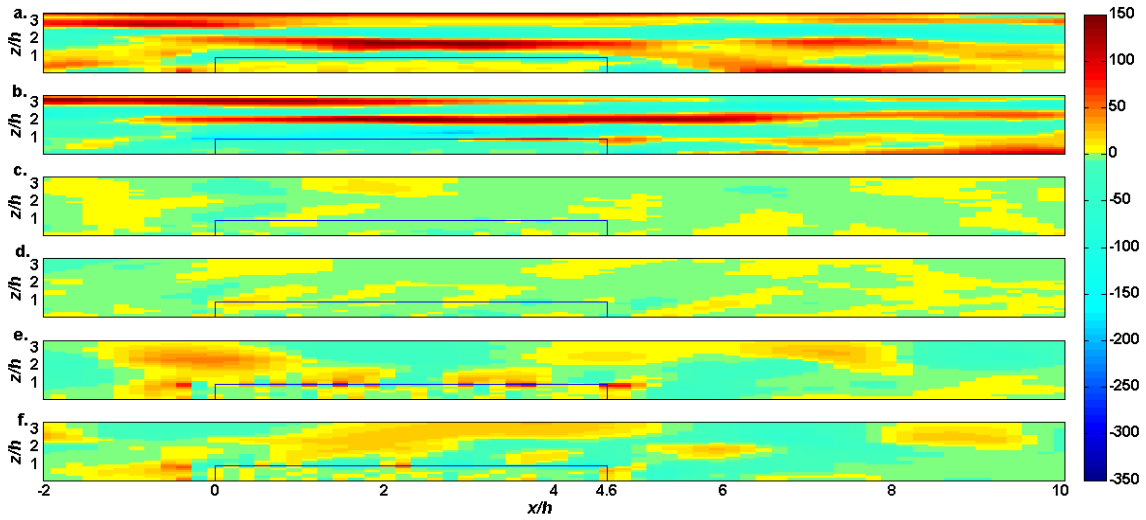

Figure 17. Low velocity cases - Comparison of spatial variation of the streamwise momentum source terms, averaged through the crosswind side of the barrier. Difference of turbulence divergence between control and drag-only sparse cases (a), dense cases (b). Difference of pressure gradient terms between control and drag-only sparse cases (c), dense cases (d), **e.** Difference of advective terms between control and drag-only sparse cases (e), dense cases (f). All terms are normalized with u_*^2 / h .

Resolving the volume restriction of the barrier reduces the magnitude of shear stress inside the barrier in low velocity cases (Figure 18a). At the upwind and downwind edges of the barrier the momentum flux is higher in the control cases and is lower than the drag-only cases inside the barrier and above it, indicating a thinner shear layer above the barriers when the volume is resolved. The plots of high-velocity cases (Figure 18b) are

similar to low-velocity cases, but show less variability across different simulation cases and they remain always positive.

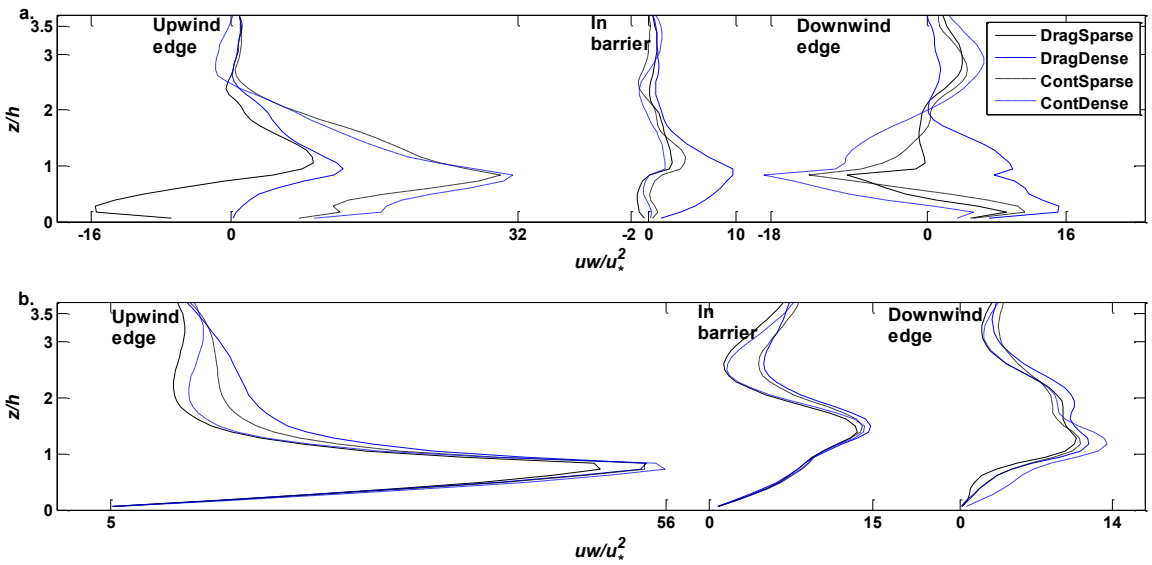

Figure 18. Comparison of variation of temporally and horizontally mean shear, averaged at three positions along the streamwise direction. **a.** Low velocity cases, **b.** High velocity cases. Labels and setup for all cases are described in table 3. Resolving the volume restriction of the barrier reduces momentum flux in the barrier.

3.2.5 Barrier effects on vorticity

Vorticity is slightly higher in the control cases shortly upwind of the barrier and decreases rapidly in the entry zone, resulting in less vorticity inside the barrier than for the drag-only cases (Figure 19a). At the exit zone, vorticity increases again and at the downwind edge of the barrier vorticity in the control cases is higher than in the drag-only

cases. In the low velocity cases we do not observe clear differences in vorticity (Figure 19b) among the various cases.

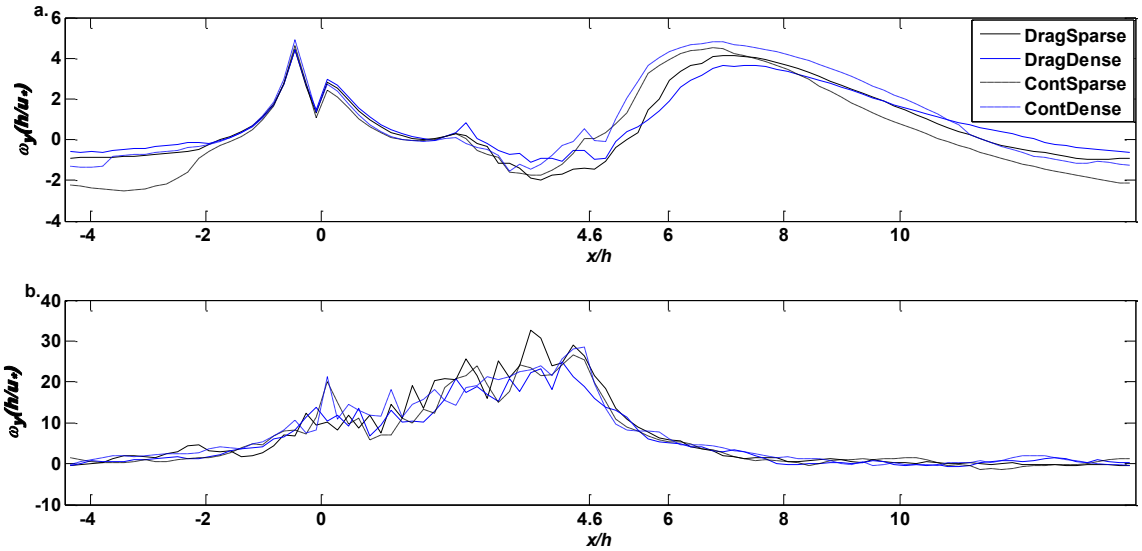

Figure 19. Comparison of normalized mean vorticity, $\omega_y\left(\frac{h}{u_*}\right)=\frac{h}{u_*}\left(\frac{\partial u_t}{\partial z}-\frac{\partial w_t}{\partial x}\right)$, averaged through the crosswind side of the barrier, across 4 extreme simulation cases at 22.5m above ground. **a.** High velocity cases, **b.** Low velocity cases. Vorticity is higher in the control cases just before the canopy and drops fast as flow enters the canopy resulting in less vorticity than in drag-only cases. Just downwind of the canopy vorticity is again higher in the control cases. In low velocity cases vorticity in control cases starts decreasing faster than drag only cases very close to the canopy edge. Same happens in high velocity cases but further downwind.

3.3 Discussion

A barrier-resolving atmospheric large-eddy simulation, RAFLES model, was employed with the aim of examining, in silico, the effects of SGS solid volume restriction in semi-porous barriers. This was achieved by using a SGS finite volume approach to the

cut-cell method for subgrid-scale representation of the barrier volume and aperture restrictions. The comparison of the cases where we prescribe only drag (drag-only cases) to those for which we prescribe drag and volume restriction (control cases) showed more persistent uplift zones upwind of the barrier, enhanced turbulent zones above the barrier and more intense recirculation zones downwind of the barrier in the control cases. The differences in these regions between the control and drag-only cases were greater in the high velocity than in the low velocity cases.

Many of the previous studies describing the effects of a semi-porous forward-facing barrier focused on an area 2-7h (h = canopy height) downwind of the forward-facing edge and inside and above the barrier, where a zone of intense vertical fluctuations in the wind is predicted (Belcher et al. 2003; Dupont and Brunet 2008a). We find that one of the most important modifications to the flow, with potentially large consequences to transport and advection from the surface, is the strengthening of this increased turbulence zone, which we observed in the high velocity cases (Figure 12, Figure 16a, 16b). A small region at the top of the barrier downwind of its forward-facing edge, where the pressure gradient was greater in the control cases relative to the drag-only cases (Figure 16c, 16d) indicates that some of the intensifying of the enhanced turbulence zone is due to the pressure gradient, as predicted by Belcher et al. (2003). This location corresponds with the location where the enhanced turbulence eddies emerge from the barrier.

The introduction of volume restriction in barrier simulation reduced the shear inside the shear layer by accelerating the flow in the barrier. This effect was relatively stronger in the low velocity cases. Therefore, the most pronounced differences between the control and drag-only cases in the low velocity simulations were in the vertical profile of

shear inside and above the barrier. However, the differences in the pressure and turbulence fields in the low velocity cases were minor.

In the high velocity cases we observed strengthening of a persistent uplift zone upwind of the barrier forward-facing edge where not only the vertical fluctuations increased but also the mean velocity was consistently upward. Such an uplift zone is typically described as a result of a solid forward-facing step (Hattori and Nagano 2010). We found that even without resolving drag, volume restriction alone could generate this uplift effect (Figure 14) and that when prescribing volume restriction in addition to drag the uplift effect is intensified (Figure 12). Our analysis suggests that built-up of pressure immediately upwind of the flow restriction that is imposed by the barrier, particularly near the lower part of the barrier (Figure 16c, 16d), and a strong advection of momentum due to a coherent structure at the top edge of the forward facing wall of the barrier (Figure 16e, 16f), are responsible for this sustained uplift.

Our simulations show a recirculation zone in the high velocity cases (observed for a forest edge by Detto et al. 2008) at the barriers down-wind edge (Figure 12). The stronger and more extensive recirculation zones are noticed in the cases that include aperture plus volume restriction (Figure 12c, 12d, 12g, 12h). The recirculation affects both the stream-wise and the vertical velocity components. Though much weaker, a relative increase in the recirculation is apparent also in the low velocity cases, when comparing the vertical and stream-wise velocity components behind the barrier, between the control and the drag-only cases (Figure 13c, 13d, 13g, 13h). The restriction-only cases generate a persistent downdraft at the back of the barrier, similar to the one that would be expected from a solid barrier (Figure 14). We propose that the enhancement of the recirculation in the control

cases is mostly driven by the differences in turbulence divergence, compared to the drag-only cases, though some differences in pressure also play a role (Figure 16a, 16b, 16c, 16d). We found that turbulence divergence played the most important role in the difference between the control and the drag-only cases in transferring and generating momentum at the sustained uplift region and in creating more intense turbulence zones. Advective terms contribute mostly in areas of rapid adjustments of the flow, such as the top-front corner of the barrier. Differences in pressure gradient had an overall small role, but contributed to generating momentum in the recirculation and uplift zones.

We show that resolving the volume affects the strength and location of coherent structures that are attached to the barrier, such as the sustained uplift and recirculation zones (Figure 12, 13). Recent flume experiments by Fontan et al. (2013) and first-order closure calculations by Banarjee et al. (2013) have suggested that a 'turbulently inviscid scheme', meaning RANS equations considering the interplay between pressure gradient, drag force, and advection could explain the onset and some aspects of the magnitude of the mean circulation - without requiring detailed or complex turbulent representation of the stresses. Our simulations support their conclusions that resolving the attachment of coherent structures in the flow to the barrier is critical to determining the location and intensity of these recirculation zones. However, turbulence divergence also plays an important role. Our study demonstrates that volume-resolving LES could be used as surrogates to flume and wind-tunnel experiments for parameterization of the effects of semi-porous barriers.

Not consistent with our predictions, we did not find cross-wind deflection and did not detect any significant cross-wind inside the barrier. In the cross-wind direction the

vertical velocity component adjusted to the barrier almost instantaneously such that differences between control and drag-only cases were not apparent. The persistent uplift zones that we notice upwind of the barrier may drive upward dispersion (ejection) of particles that arrive from the upstream region and deflect them from entering the barrier. This may lead to reduced particle flow into the barrier, and may reduce the effectiveness of wind barriers to stop dispersing dust and other volatile compounds and aerosols. For example Prueger et al. (2008) observed that a small group of farm buildings drives increased dispersion of dust from an animal feeding facility. Others observed more intense uplift dispersion of smoke near forest edges (Bergen 1975; Goodrick et al. 2013). Simultaneously, the stronger recirculation zones in the control cases imply more accumulation of particles at the lee side of barriers. This may impact snow and dust accumulation downwind of vegetation patches, especially in cases of high wind speeds (Winstral et al. 2013). It can also lead to heat accumulation in the downwind edge of a forest in case of fire. Resolving the barrier volume and aperture also leads to differences in the vertical profiles of turbulence and shear stress in and above the barriers, which may be important for simulating phenomena that depend on fluxes from barriers, such as urban heat islands (Bohnenstengel et al. 2011) and air quality implication of particle dispersion into cities and emission of particles and volatile organic compounds from cities and forests.

Chapter 4: Tracking fire-emitted heat transport in low intensity fires using large eddy simulations

Many years of extensive logging and fire suppression resulted in substantial degradation and loss of fire-dependent ecosystems (Allen et al. 2002). Recently, the important role that fire plays in preservation of structure and function of forests has been recognized (Keane et al. 2008). The reintroduction of fire to fire-dependent ecosystems, such as pine forests, by prescribing controlled fires started gaining ground (Dickinson and Ryan 2010). When managing prescribed fires, forest managers aim to benefit the fire-dependent species and avoid future catastrophic fires, while at the same time eliminate excessive tree mortality and smoke dispersion (Reinhardt et al. 2001; Finney 2005; Hyde et al. 2013). Software tools that predict tree mortality (Dickinson et al. 2004; Keane et al. 2008; Michaletz and Johnson 2008; Kavanagh et al. 2010; Hoffman et al. 2012; Chatziefstratiou et al. 2013), and fire behavior (Linn and Cunningham 2005; Pimont et al. 2011; Mell et al. 2012) have been developed to assist forest managers in prescribing fire knowledgably and preventing the unwanted effects of fires.

Wildland fire behavior and its effects are a result of complex mechanisms that couple combustion and ignition processes of the ground and canopy fuels, ecological processes that are related to the organization, density composition and moisture of the fuels, and atmospheric processes responsible for fanning the fire, and for advection of heat,

smoke and burning ambers that may ignite further fires downwind. Current studies are providing advances in the form of the development and application of coupled atmosphere-fire models that simulate the interaction among atmosphere, fire, forests, and topography at multiple scales (Linn and Cunningham 2005; Mell et al. 2007; Mell et al. 2009; Sullivan 2009; Calkin et al. 2010; Parsons et al. 2011; Pimont et al. 2011).

Due to scarcity of suitable burning days and the large effort associated with a prescribed fire event, fire managers want to maximize the area burned and minimize the number of distinct prescribed burn events without causing undue damage to the ecosystem. Thus, the use of dense fire patterns was considered an appropriate management technique, because it allows for rapid burn out and optimal smoke dispersal (Johansen 1984, 1987). Experience showed, however, that high density ignition is a risky practice as it sometimes results in accidental crown fire that leads to high tree mortality rates. The dense canopy is assumed to create substantial drag that prevents venting of hot plume gases causing buildup of heat below and within the canopy. The proposed solution is to enhance canopy ventilation by forest thinning and by creating gaps in the canopy (Pimont et al. 2011; Hoffman et al. 2012). However, thinning the canopy may lead to increased smoke dispersion. Fire managers are responsible for maintaining air quality standards at communities around the areas where fire is prescribed. Striking the right balance between fire-assisted ecosystem restoration and maintenance goals and potential negative impacts due to fire-driven tree mortality and excessive smoke dispersion from a prescribed fire is challenging, but necessary for efficient prescribed burning.

The aim of this work is to examine the interactions between forest structure and fire pattern and their narrow consequences to heat transport and accumulation inside the

canopy during prescribed fires in forest ecosystems. More specifically, we introduced a simplified fire-like heat source module to an atmospheric model, RAFLES (Bohrer et al. 2009), to simulate heat exchange between canopy and atmosphere during simplified, prescribed, low-intensity surface fires in forests of different canopy leaf densities, gap fractions, and fire patterns.

Furthermore, of particular concern to air-quality management are the impacts of fires to air quality. For example, smoke from fires that occur in wildland-urban interface (WUI) areas can linger for relatively long periods of time and have an adverse effect on human health or reduce visibility over roads and highways in the vicinity of and downwind of these fires (Mercer and Weber 1994). Thus, understanding how the heat and thermal uplift interact with fires and canopy structure is crucial for fire and air quality management.

4.1 Material and methods

4.1.1 Simulation of Experimental Set up

The full model formulation of RAFLES is provided in Bohrer et al (2009). As it is the focus of this study, we repeat the model's formulation for conservation of heat:

$$\frac{\partial \bar{\theta}}{\partial t} = \frac{1}{\rho_0}\left[\frac{\bar{\theta}\partial\left(\rho_0 \overline{u_j}\right)}{\partial x_j} - \frac{\partial\left(\rho_0 \overline{u_j}\,\bar{\theta}\right)}{\partial x_j} - \frac{\bar{\theta}\partial\left(\rho_0 \overline{u_j'\theta'}\right)}{\partial x_j}\right] + S_\theta, \qquad (4.1)$$

where S_θ is the sum of sources and sinks of heat, u is wind velocity, t is time, θ is potential temperature, and ρ_0 is air density. The variables are decomposed into two components: a resolved (mean, box-filtered) component, marked by overbar, and the sub-grid-scale (SGS) perturbations, marked by prime.

Periodic boundary conditions are applied at the lateral domain edges. No-flow boundary condition is set at the top boundary with free slip conditions for the horizontal velocity and zero vertical velocity. Rayleigh friction is applied to the upper five grid levels to simulate artificial waves forming near the top boundary. At the domain floor, the velocity normal to the floor is specified to be zero. Surface momentum fluxes are imposed through a drag term on the three wind velocity components at the land surface and throughout the canopy sub-domain, as a function of drag generating surface and the surface roughness properties at each canopy or surface pixel. Details of the canopy and surface drag formulations are presented in Chatziefstratiou et al. (2014).

The simulated spatial domain was identical for all simulations, measuring 1250 m × 1250 m × 1400 m along the x, y, and z axes, respectively. The horizontal grid resolution is 5 × 5 m^2 and the vertical grid resolution is 3 m from the ground and up to 100 m, above this height, a 20% stretching is applied for each consecutive vertical layer up to a maximum grid spacing of 30 m. The simulation domain included 250 x 250 x 95 pixels.

4.1.2 Virtual experiment

4.1.2.1 Canopy structures

We simulated 6 canopies with various structures, each with two different fire patterns. The canopy height was kept at 15 m for all the cases. In our initial case the mean diameter at breast height (DBH), the mean leaf area index (LAI), mean surface net radiation (F_{tot}), and mean Bowen ratio were determined by onsite measurements. The 6 canopy structures are depicted in Figure 20.

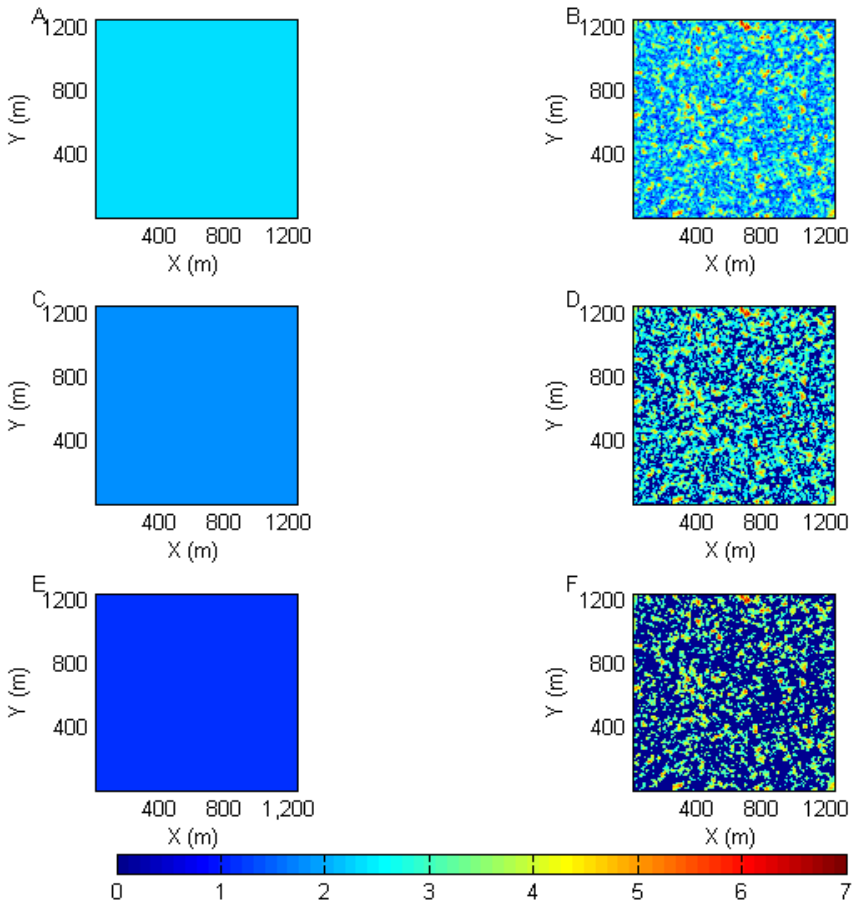

Figure 20. Canopy description. Color depicts Leaf Area Index (LAI). Left column depicts homogeneous cases, right column depicts heterogeneous/gappy cases. A. (case name: Hom): mean LAI=2.3825, B. (case name: Het): mean LAI=2.3825, C. (case name: L75): mean LAI=1.785 (75% of initial), D. (case name: G75): mean LAI=1.785 (75% of initial), E. (case name: L50) mean LAI=1.19 (50% of initial), F. (case name: G50) mean LAI=1.19 (50% of initial).

4.1.2.2 Meteorological forcing and initialization

Though it is not directly important for this study, we have based our initial conditions and base-line canopy structure on observations taken during a prescribed fire in the NJ Pine Barrens during April 2011, with initial temperature approximately 272K and horizontal mean wind velocity approximately 3 m/s (Figure 21).

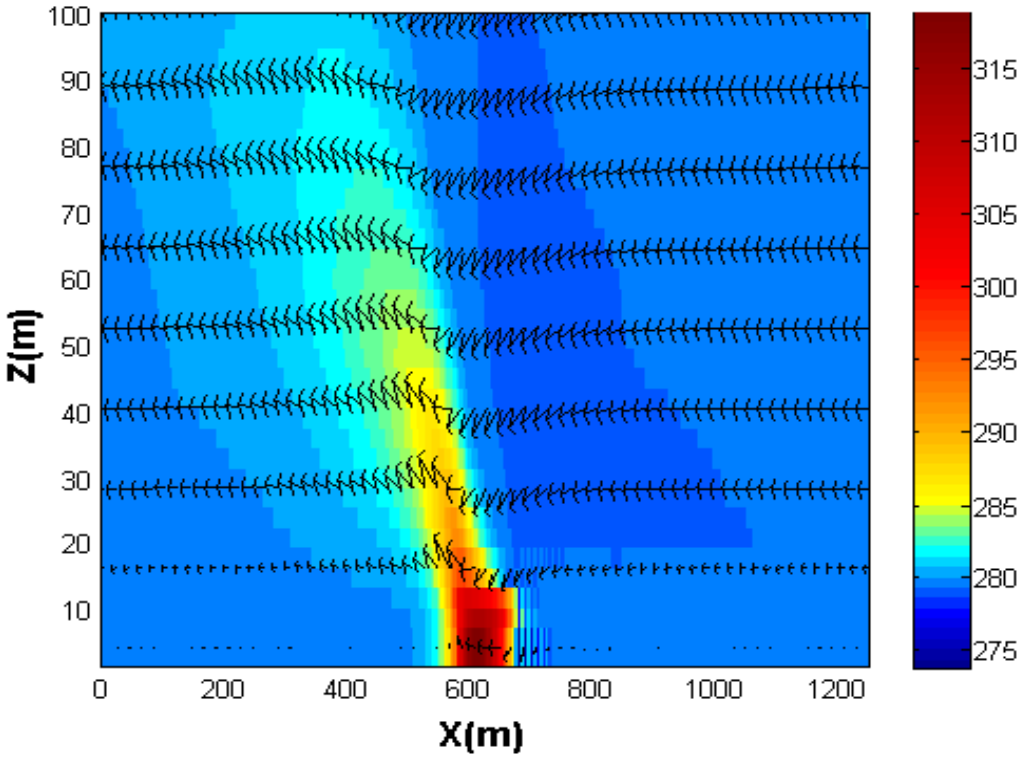

Figure 21. Vertical cross-section of the experimental domain showing the burning plot. The arrows represent the wind velocity (m/s) and the color the temperature (K).

4.1.2.3 Fire simulations

Simulations ran for 2.5 hours to achieve a quasi-stationary stage, before heat was released. In our simulations, fire was represented in a highly simplistic approach as a heat source. We tested two contrasting patterns of "fire" – homogenous and heterogeneous. In all cases, we released heat over a 100 m wide "fireline" strip throughout the simulation domain (Figure 22). The periodic boundary at the y axis, thus, allows us to reduce the dimension of our analysis to 2 directions (spanwise and vertical) and avoid edge effects by crosswind flow. The location of the fireline throughout the simulation and the heat flux prescribed are assumed steady and invariable within each "burning phase". The fireline intensity is 1,000 KW/m, which is within the typical range of a low-intensity prescribed fire. For simplicity, we assumed that the fire is only represented by heat flux and did not include additional water vapor or other volatile buoyant scalar fluxes. We simplified the dynamics of a fireline to 3 burning phases: burning, smoldering and cooling, and represented each phase with a different heat flux 1,000 KW/m, 100 KW/m, and no heat flux, respectively. For the convenience of the simulation, we assume each phase lasted 5 minutes, through this assumption is highly unrealistic. Here, we mainly focus on the burning phase, which lasts for 300 s and the following results are averaged throughout the 300 s of the burning period and along horizontal strips parallel to the fire line. We tested two different fireline patterns – homogeneous, where the heat flux was uniform throughout the fireline, and heterogeneous where we used the V-Cage model (Bohrer et al 2007) to generate an arbitrary field of heat flux values twice as high as the initial ones but applied at the half area (Figure 22).

4.2 Results

Following (Monson and Baldocchi 2014) we calculated the different terms in the conservation equation governing heat as follows:

Vertical advection:

$$AdvZ = \frac{1}{\Delta x \Delta y} c_p \int_{x_0}^{x_{end}} \int_{y_0}^{y_{1250}} \rho \overline{w} \frac{\partial \overline{T}}{\partial z} \mathrm{dxdy}, \qquad (4.2)$$

Horizontal advection:

$$AdvX = \frac{1}{\Delta y \Delta z} c_p \int_{y_0}^{y_{1250}} \int_{z_0}^{z_{end}} \rho \overline{u} \frac{\partial \overline{T}}{\partial x} \mathrm{dydz}, \qquad (4.3)$$

Vertical turbulent divergence:

$$TurbZ = \frac{1}{\Delta x \Delta y} c_p \int_{x_0}^{x_{end}} \int_{y_0}^{y_{1250}} \rho \frac{\partial \overline{w'T'}}{\partial z} \mathrm{dxdy}, \qquad (4.4)$$

Horizontal turbulent divergence:

$$TurbX = \frac{1}{\Delta y \Delta z} c_p \int_{x_0}^{y_{1250}} \int_{y_0}^{z_{end}} \rho \frac{\partial \overline{u'T'}}{\partial x} \mathrm{dydz}, \qquad (4.5)$$

Change of heat storage:

$$HStor = \frac{1}{\Delta x \Delta y \Delta z} c_p \int_{x_0}^{x_{end}} \int_{y_0}^{y_{1250}} \int_{y_0}^{z_{end}} \rho \frac{\partial \overline{T}}{\partial t} \mathrm{dxdydz}, \qquad (4.6)$$

where x_0 is the beginning of the control volume, x_{end} is the end of the control volume towards x-axis and z_0 is the beginning of the control volume, z_{end} is the end of the control volume towards z-axis. All the results are averaged throughout the y-axis, as we release heat throughout the specific axis (Figure 22) and for the 300 s of burning phase. Next, we discuss two cases, in the first one, we average our results for the area between x_0 = 385m end x_{end} = 670m, and in the second one we calculate point measurements at x = 575m, where w't' peaks for the homogeneous case (Figure 23). H is the canopy height. w refers to vertical velocity (m/s), u refers to stream-wise horizontal velocity (m/s), T refers to temperature (K), ρ is air density (approximately 1.25 Kg/m^3), c_p is heat capacity of dry air (1004 J/(KgK)). Δx, Δy, Δz is the grid dimensions in x, y and z axis respectively, as discussed above. The overbar indicates temporal average of the value and the prime indicates the instant value minus the temporal average.

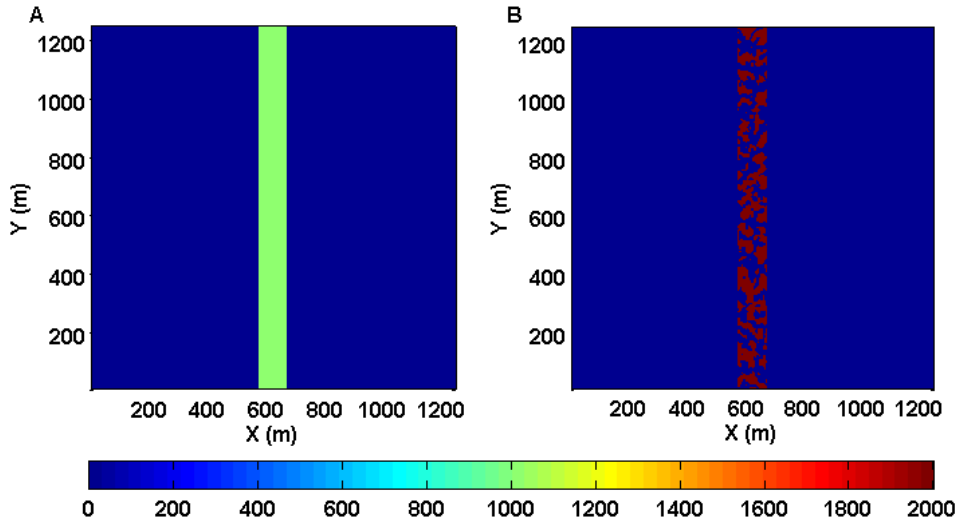

Figure 22. Fire patterns. Color depicts fireline heat flux (Kw/m). The total fire intensity was kept the same in all cases. A. Homogeneous case, B. Heterogeneous case (marked with the letter F from here on).

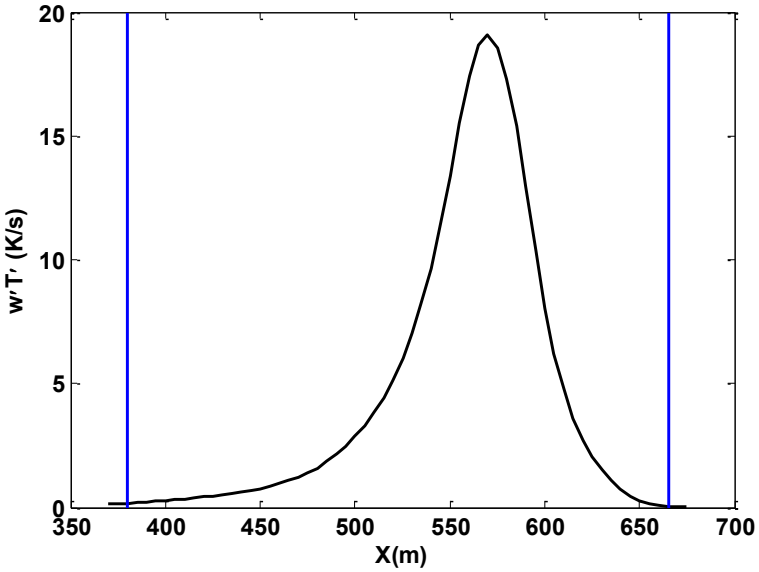

Figure 23. Change of vertical turbulent flux in K/s at 21 m height (≈1.5 canopy height). Blue lines enclose the area in x-axis where w't' is assumed significant.

4.2.1 Heat dispersion in and above canopy for "averaged case"

We first studied the "baseline" case with the homogeneous canopy and fire pattern and with the results averaged both throughout the y direction and the area between x_0 = 385m end x_{end} = 670m. This is an ideal case, since in reality we are only able to calculate heat flux at a very limited number of points in the canopy. The vertical profile that compares all the heat transfer mechanisms (Figure 24) shows that the dominant mechanisms of transferring heat in the canopy and out of it, are vertical turbulent flux and horizontal advective flux. The turbulent eddies that are formed in the canopy and in the roughness sublayer play dominant role in transferring heat vertically. In flux measurements above forests, it is assumed that above canopy top, the flux divergence is zero and thus the vertical flux coming out of the canopy is equal to w't'. However, our results show that flux

divergence starts positive then becomes negative and it never goes to zero. In addition to turbulence, horizontal advection also contributes significantly to heat dispersion. Thus, even if we assume that flux divergence becomes negligible at some height next to canopy top, we will still have to account for horizontal advective flux. However, because of the complexity and the higher number of meteorological towers that the calculation of horizontal advection demands, it is usually ignored in flux measurements.

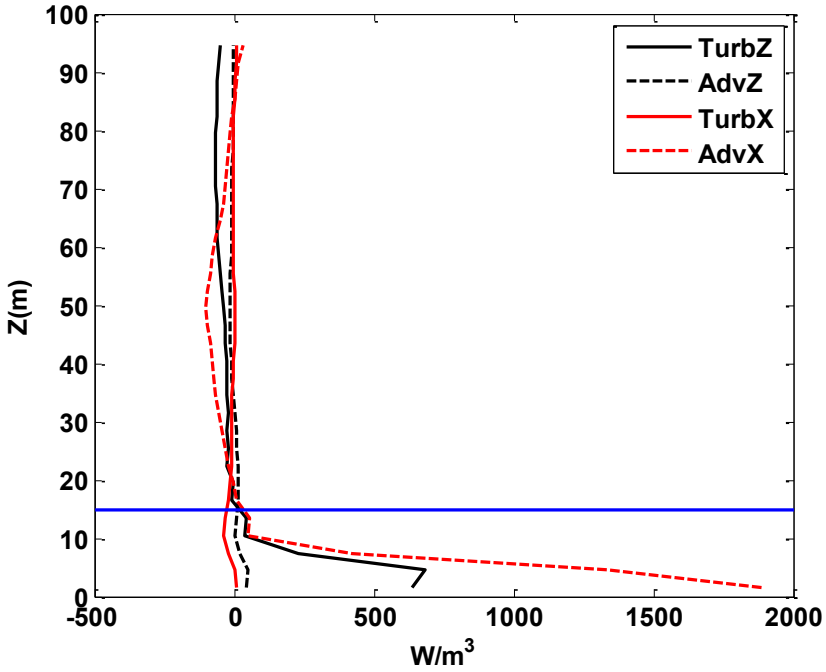

Figure 24. Averaged vertical profiles of vertical turbulent flux (*TurbZ*) and advection (*AdvZ*), horizontal turbulent flux (*TurbX*) advection (*AdvZ*) for the homogeneous canopy and fire pattern. The blue line marks the height of the canopy

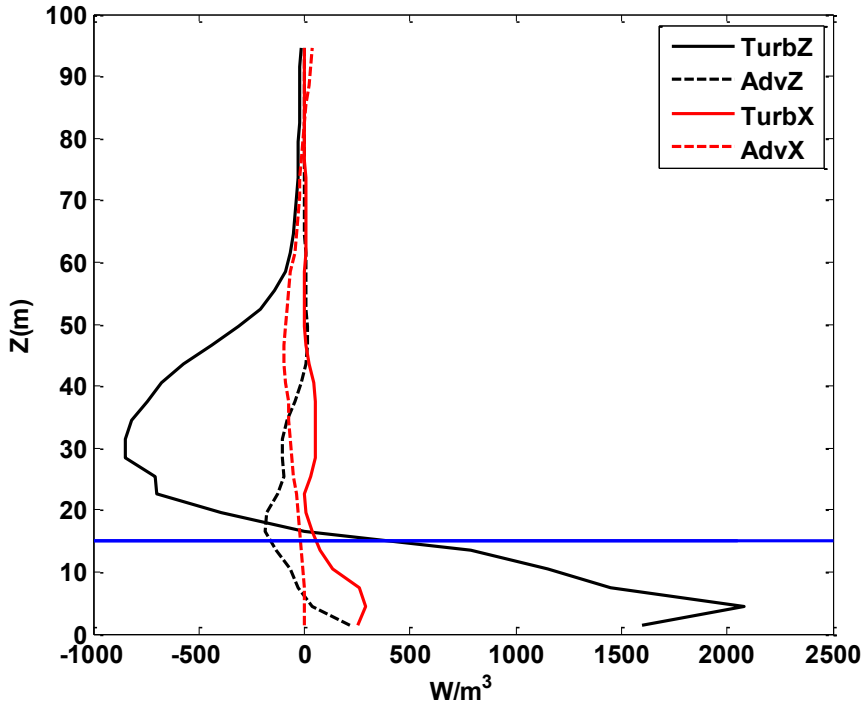

Figure 25. Point (at x=565m) vertical profiles of vertical turbulent flux (*TurbZ*) and advection (*AdvZ*), horizontal turbulent flux (*TurbX*) advection (*AdvZ*) for the homogeneous canopy and fire pattern. The blue line marks the height of the canopy.

4.2.2 "Average" Vs "point" calculations

In most applications the vertical turbulent fluxes are measured only in very few points (1-3) shortly above canopy and advection is usually assumed negligible (Aubinet 2008; Baldocchi 2008). However, our results in the case of a point calculation of heat flux at x = 670m show that significant turbulent divergence is extended up until 3-4 times the canopy height (Figure 25). That implies that it is not advisable to calculate turbulent flux at a height closer to the canopy, which is usually the case, because at that height the

turbulent divergence is not negligible and thus w't' is not equal to the vertical heat flux coming out of the canopy. In addition to that, it is very hard to suggest only one or two places where we can set the meteorological towers and expect to capture the whole heat coming out of canopy, because there are spots in the canopy with high heat flux and places with low heat flux coming out. Thus, we cannot measure in one spot and make safe predictions regarding the whole heat coming out of the canopy. Flux measurements are even more complicated when the fireline moves, which is usually the case.

4.2.3 Heat storage and temperature in and above canopy

Heat storage (Figure 26) in the canopy, in the control volume described in Figure 23 is higher in cases with homogeneous canopy structure and fire pattern. Moreover, mean temperature in the canopy is higher for the homogeneous cases even in the cases with reduced leaf area (Figure 27). The introduction of any kind of heterogeneity, both in the canopy by adding gaps and especially in the fire pattern by burning in irregular pattern, reduces both the heat stored in the canopy and the temperature in the canopy. This reduction, implies that in these cases heat leaves canopy faster either with advection or turbulence. To verify that, following we looked at the turbulent and advective heat flux profiles.

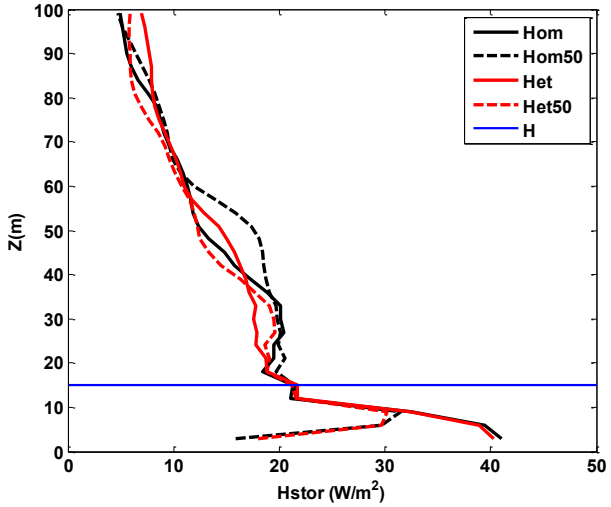

Figure 26. Heat storage (*HStor*) for different simulation cases. The blue line marks the height of the canopy.

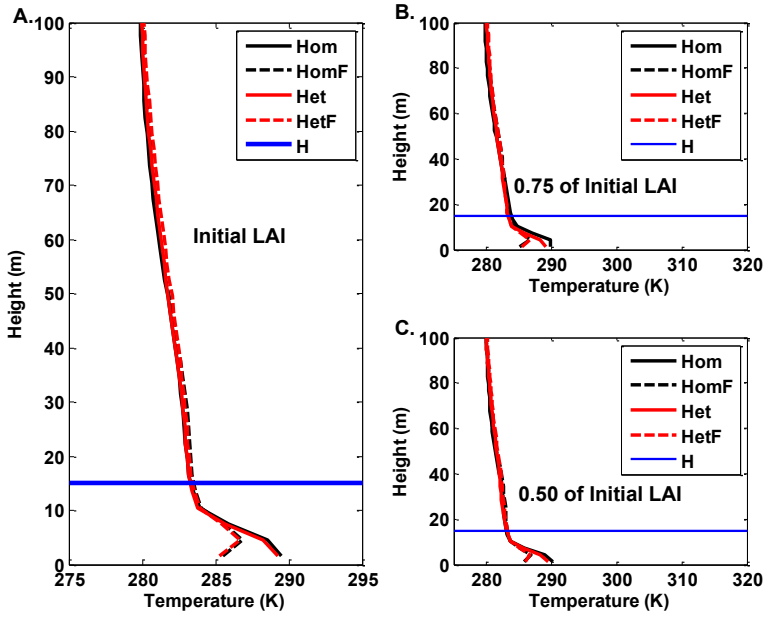

Figure 27. Temperatures in the burning plot and above it. Canopy structures are depicted in figure 20. The letter F at the end of half of the cases stand for heterogeneous fire pattern. Fire patterns are showed in Figure 22. The blue line marks the height of the canopy.

4.2.4 Effects of canopy and fire heterogeneity on heat flux

On the one hand, vertical turbulent heat flux is higher in the case with homogeneous canopy structure and fire pattern at every height (Figure 28). For all cases, it peaks exactly at the canopy top. The introduction of any kind of heterogeneity reduces vertical turbulent heat flux. On the other hand, horizontal advective heat flux is higher in the heterogeneous cases (Figure 29). It peaks at the bottom of the canopy and then reduces as we move higher in the domain. The differences in heat flux are more obvious when comparing cases with the same canopy structure and different fire pattern.

Although horizontal advective flux becomes stable and almost negligible at a height approximately four times the canopy height, vertical turbulent heat flux keeps changing even higher than six times canopy height.

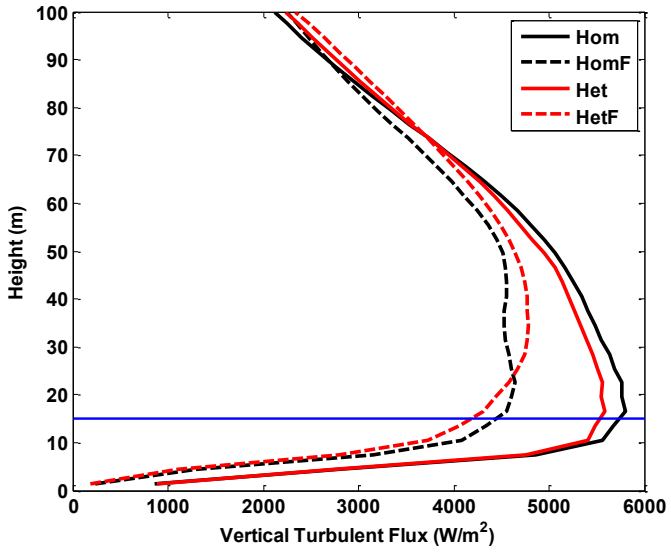

Figure 28. Vertical turbulent flux Vs height. The blue line marks the height of the canopy.

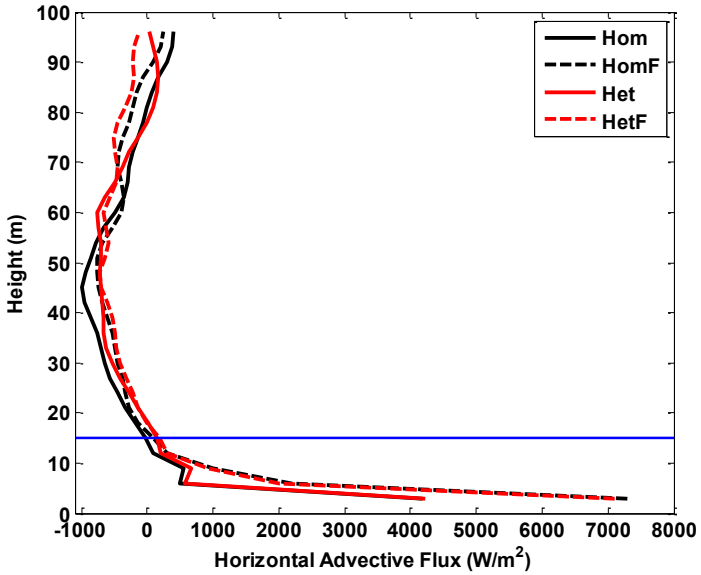

Figure 29. Horizontal advective flux Vs height. The blue line marks the height of the canopy.

4.3 Discussion

A LES atmospheric model was employed to introduce a heat release module and study heat dispersion in canopies of different structures in low intensity fires. The first goal of our study was to investigate whether it is possible to suggest a realistic way of measuring accurately the heat coming out of a canopy during a fire. Our results showed that flux divergence in case of point measurements becomes zero above 4 times. Thus setting a meteorological tower right above canopy top to measure vertical heat flux which is common practice is not ideal. Moreover, according to our results, both vertical turbulent flux play horizontal advective flux play dominant roles in heat dispersion in the atmosphere and it is recommended to be studied together when tracking fire heat flux.

Next we compared cases of various canopy structures and fire patterns. The cases with the homogeneous canopies and the homogeneous fire patterns entrap the most heat for the longest time period and release the heat to the atmosphere in the lowest rate resulting in higher temperatures in the canopy (Figures 27). Thus, in homogeneous forests where there are concerns of high tree mortality rates because of high temperatures in the canopy, it would be advisable to create some gaps and prefer heterogeneous fire patterns over homogeneous.

Moreover, by comparing the heat storage to the turbulent and advective fluxes, we conclude that heat does not stay in the canopy for too long and almost immediately after the burning all the heat stored in the canopy gets released to the atmosphere. The strong turbulent and advective fluxes reduce the capacity of the canopy to store heat and thus the canopy releases the heat that was built up during the fire very fast. Therefore, we would not expect to notice extended post fire tree mortality in the cases discussed here.

In general, we observed that any kind of heterogeneity reduces temperature in the canopy. That indicates that in the heterogeneous cases, heat escapes the canopy easier. Therefore, it is suggested to avoid conducting measurements near gaps that act as paths to vent heat from the canopy.

Chapter 5: Conclusions

5.1 Summary of this work

We presented two novel computational tools that contribute to the prediction of fire effects and the linking of fire mechanisms to fire effects, a stem heat transfer model and a heat release module of an atmospheric model. Our 2D stem heat-transfer model, FireStem2D, accurately predicts temporal variation in stem temperatures and necrotic depths in the circumference of a tree. As fire effects may vary around the tree circumference, depending on velocity of the wind, and tree death is assumed to follow deterministically if the stem is girdled, the unique ability of our model to simulate heat transfer in 2 directions, provides results that can lead to valid predictions on whether the tree will survive or not a fire event. Moreover, FireStem2D can estimate what fraction of the total cambium was injured at different heights. This will bridge the knowledge gap between understanding of the fire heat dynamics and predicting of tree stem injury. Therefore, FireStem2D is a useful tool for wildland fire management decision support. The use of heat-flux and not temperature boundary conditions, unlike other heat transfer models, makes it possible to couple FireStem2D to a fire behavior model (e.g., BEHAVE, WFDS, FIRETEC) that can provide fire heat flux when weather conditions and key fuel characteristics are known. FireStem2D, as a physics-based model could be broadly applied given further parameterization for the thermal parameters of tree species not included in this work. The expanded applicability of FireStem2D makes it a useful tool that can be

parameterized for any species and can predict necrotic depths for any species under any heat-flux conditions.

Further, we incorporated a heat release module to an LES atmospheric model, RAFLES. An important aspect of RAFLES is its ability to simulate canopy not only by the drag that imposes on the air flow but also by the restriction that the volume of the tree stems imposes on the air flow. Our simulations showed that representation of the effects of the volume and the aperture closure due to vegetated canopy and other semi-porous obstacles on flow is important. When the volume and the aperture closure were represented the updraft of airflow at the upwind edge of the barrier intensified. Simultaneously, the downdraft at the downwind edge became stronger, also resulting in the formation of a stronger recirculation zone. The small-scale interactions of wind with vegetation and/or structures are hard to measure or conduct as a large-scale empirical experiment. LES models can provide a tool for *in silico* experiments of these interactions (e.g., Dupont and Brunet 2008b; Bohrer et al. 2013). In such cases, representation of subgrid-scale volume restriction could provide an improvement to LES-resolved dynamics that should be considered.

The incorporation of our heat release module to RAFLES, was aimed to simulate a low-burning understory fire that allowed us to investigate how different canopy structures interact with additional surface heat flux and how these interactions influence turbulence and heat exchange between canopy and atmosphere. Striking the right balance between fire-assisted ecosystem restoration and maintenance goals and potential negative impacts due to excessive tree mortality or excessive smoke dispersion from a prescribed fire is challenging, but necessary for efficient prescribed burning. For fire managers, knowing in

advance how much heat would accumulate and how fast would get dispersed, should they prescribe a burning with given fire pattern and canopy structure, would assist them for better prescribed fire planning and forest management.

5.2 Future directions

While this work contributed to the research and modeling of fire effects, there is still ground for improvement of our models to better capture the physical phenomena and be linked to fire behavior models to eventually constitute easy tools for fire effects predictions.

As far as FireStem2D concerns, an important aspect of the model is that it uses heat flux boundary conditions. Thus, it is recommended that future work establish the link between our stem heating model and a fire behavior model. Future work could also be focused on further development of FireStem2D, so that it accounts for the vertically advected heat by the sap transported upwards when the xylem temperature is high.

As far as the heat release module of RAFLES concerns, our goal is not to replace existing fire behavior models, but to examine how heat released by a fire would interact with a 3D realistic canopy structure and affect biosphere. The module is a simplified heat release model that does not account for the thermophysical processes occurring during a fire. It is recommended that future work would be focused on how to release heat in a more realistic rate and allow the fire line move during burning.

5.3 The future of fire effects modeling

Although forecasting the evolution of fire effects and fire behavior models can be rather risky, we can still provide a rough estimation of the future of such models based on work that has been done until present and the growing interest of the society towards the risks of uncontrolled or poorly managed fires.

Forecasting fire effects is not a recent endeavor. As early as the beginning of previous century researchers started developing models that describe the response of trees to fire. They started with empirical models that afterwards they also incorporated some theoretical principals (e.g., BEHAVE) and only in recent years fully theoretical models started developing for forecasting fire effects (e.g., Firestem2D) and fire behavior (e.g., FIRETEC, WFDS). Nowadays, the emerging increase of catastrophic fires raises even more concern not only for the environment but for human lives and property, as well. Poor management (Allen et al. 2002) and climate change (Schoennagel 2004) are the two major factors that contributed to the increase of catastrophic fires in recent years. Westerling et al. (2006) showed that large wildfire activity increased in the mid-1980s, with higher large-wildfire frequency, longer wildfire durations, and longer wildfire seasons. The increase is strongly associated with increased spring and summer temperatures and earlier spring snowmelts of recent years.

As discussed earlier, fire managers, as a response to the growing awareness of uncontrolled fire effects, constantly reevaluate their tactics for efficient wildland fires management. However understanding wildland fires that are driven by complex physical and chemical processes whose interactions depend on the coupling between atmosphere, fire, topography, and solid fuels is not an easy task. Furthermore, it is very difficult to study

them with full-scale repeatable experiments due to money, time and safety constraints. Therefore, fire effects and fire behavior models are gaining ground and attract scientific interest.

Appendix: Thermal tolerance parameter estimation.

Thermodynamic parameters describing pseudo-first-order heat impairment of bark, stem, and foliage were estimated or obtained from three papers. Caldwell (Caldwell et al. 1993) examined impairment of tissue respiration in discs cut from cucumber leaves. Dickinson and Johnson (Dickinson and Johnson 2004) quantified impairment of tissue respiration in samples of live bark. Lorenz (Lorenz 1939) estimated survival in populations cortical parenchyma cells sectioned from the stems of seedling. Tissue impairment described by cell death and impairment of cellular respiration are analogous (Dickinson et al 2004). First-order rate constants are described by the following relationship (Rosenberg et al. 1972):

$$\mathrm{f} = \frac{\mathrm{k_B} T}{h} \exp\left(\frac{\Delta S}{R}\right) \exp\left(\frac{-\Delta H}{RT}\right) \quad , \qquad \text{Equation A1}$$

where f is the rate constant (s^{-1}), k_B is the Boltzman constant (1.38 × 10–23 $J\ K^{-1}$), T is temperature (K), h is Planck's constant (6.63 × 10–34 $J{\cdot}s$), ΔS is the activation entropy ($J\ mol^{-1}\ K^{-1}$), R is the universal gas constant (8.31 $J\ mol^{-1}\ K^{-1}$), and ΔH is the activation enthalpy ($J\ mol^{-1}$). Rate constants for different temperature exposures were estimated from tables reported in Lorenz (1939) and extracted from figures in Caldwell et al. (1993)

because raw data were not reported in tables. Thermodynamic parameters estimated from (Caldwell et al. 1993, Dickinson and Johnson 2004, Lorenz 1939) are shown in Table A1.

We examined whether parameters in Table A1 followed compensation law behavior as did parameters describing heat effects on proteins, viruses, yeasts, and bacteria reported in Rosenberg et al. (1972). Thermodynamic parameters were highly correlated (R^2 = 0.997):

$$\Delta S = \frac{1}{T_{crit}} \Delta H - b = \frac{1}{341} \Delta H - 258 \quad , \qquad \text{Equation A2}$$

where T_c (K) is the compensation temperature and b is the intercept ($J\ mol^{-1}\ K^{-1}$). These values are similar to Rosenberg et al. (1972) values, where T_{crit} ranged from 325-331 and b ranged from 268 to 272. The parameter values in Equation A2 and the average of the activation enthalpy estimates in Table A1 (ΔH = 318,344) were used in FireStem2D (see Equation 17).

Study	Species	N	T_{min}	T_{max}	ΔS	ΔH
Dickinson and Johnson (2004)						
Fall/Winter	*Populus tremuloides*	17	43	65	372(140)	217524(46603)
Fall/Winter	*Picea glauca*	11	43	65	455(328)	246032(107117)
Spring/Summer	*Populus tremuloides*	10	43	65	665(133)	312522(43889)
Spring/Summer	*Picea glauca*	12	53	65	575(208)	283968(68354)
Spring/Summer	*Pseudotsuga menziesii*	15	43	65	528(252)	270036(81790)
Spring/Summer	*Pinus contorta*	17	43	65	518(214)	267984(70254)

Continued

Table 4. Thermodynamic parameters estimated by fitting Equation A1 to data. Data from the 25 °C pretreatment group were used from Caldwell (1993). Caldwell tested two varieties of cucumber (Poinsett and Ashley) and mean rate constants were extracted from his Figure 4 so standard deviation estimates were not valid. The temperature range (Tmin to Tmax) for each experiment is given (ºC).

Table 4 continued

Lorenz (1939)						
	Catalpa speciosa	7	59	66	1649(533)	648885(178796)
	Pinus strobus	11	56	66	895(217)	396706(72666)
	Ulmus americana	12	57	68	844(244)	381648(81858)
	Picea glauca	14	56	69	529(176)	274719(59148)
	Pinus resinosa	9	58	66	872(198)	389085(66524)
Caldwell (1993)						
	Cucumus sativa - *Poinsett*	10	46	60	87(NA)	112131(NA)
	Cucumus sativa - *Ashley*	7	40	60	784(NA)	337230(NA)

References

Adcroft A, Hill C, Marshall J (1997) Representation of topography by shaved cells in a height coordinate ocean model. Mon Weather Rev 125: 2293-2315.

Allen CD, Savage M, Falk DA, Suckling KF, Swetnam TW, Schulke T, Stacey PB, Morgan P, Hoffman M, Klingel JT (2002) Ecological restoration of Southwestern ponderosa pine ecosystems: A broad perspective. Ecol Appl 12: 1418-1433.

Arakawa A, Lamb VR (1977) Computational design of the basic dynamical processes of the UCLA general circulation model. Methods in Computational Physics: Advances in Research and Applications Chang J, Ed., Academic Press, 174-265.

Aubinet M (2008) Eddy covariance CO(2) flux measurements in nocturnal conditions: An analysis of the problem. Ecol Appl 18: 1368-1378.

Avissar R, Eloranta EW, Gurer K, Tripoli GJ (1998) An evaluation of the large-eddy simulation option of the regional atmospheric modeling system in simulating a convective boundary layer: A FIFE case study. J Atmos Sci 55: 1109-1130.

Avissar R, Schmidt T (1998) An evaluation of the scale at which ground-surface heat flux patchiness affects the convective boundary layer using large-eddy simulations. J Atmos Sci 55: 2666-2689.

Baldocchi D (2008) Breathing of the terrestrial biosphere: lessons learned from a global network of carbon dioxide flux measurement systems. Aust J Bot 56: 1-26.

Banerjee T, Katul G, Fontan S, Poggi D, Kumar M (2013) Mean flow near edges and within cavities situated inside dense canopies. Boundary-Layer Meteorol 149:19–41: 19–41.

Belcher SE, Finnigan JJ, Harman IN (2008) Flows through forest canopies in complex terrain. Ecol Appl 18: 1436-1453.

Belcher SE, Jerram N, Hunt JCR (2003) Adjustment of a turbulent boundary layer to a canopy of roughness elements. J Fluid Mech 488: 369-398.

Bergen JD (1975) Air movement in a forest clearing as indicated by smoke drift. Agric Meteorol 15: 165-179.

Bergman TL, Lavine AS, Incropera FP, Dewitt DP (2011) Introduction to heat transferJohn Wiley & Sons, 960 pp.

Bohnenstengel SI, Evans S, Clark PA, Belcher SE (2011) Simulations of the London urban heat island. Q J R Meteorol Soc 137: 1625-1640.

Bohrer G, Wolosin M, Brady R, Avissar R (2007) A Virtual Canopy Generator (V-CaGe) for modeling complex heterogeneous forest canopies at high resolution. Tellus Ser B-Chem Phys Meteorol 59B: 566-576.

Bohrer G, Nathan R, Katul GG, Walko RL, Avissar R (2008) Effects of canopy heterogeneity, seed abscission, and inertia on wind-driven dispersal kernels of tree seeds. J Ecol 96: 569–580.

Bohrer G, Katul GG, Walko RL, Avissar R (2009) Exploring the effects of microscale structural heterogeneity of forest canopies using large-eddy simulations. Boundary-Layer Meteorol 132: 351–382.

Bohrerova Z, Bohrer G, Cho KD, Bolch MA, Linden KG (2009) Determining the viability response of Pinus taeda pollen under abiotic stresses typical to atmospheric conditions during long distance dispersal. Ecol Appl 19: 656-667.

Bova AS, Dickinson MB (2005) Linking surface fire behavior, stem heating, and tissue necrosis. Canadian Journal of Forest Research 35 814-822.

Bovard BD, Curtis PS, Vogel CS, Su HB, Schmid HP (2005) Environmental controls on sap flow in a northern hardwood forest. Tree Physiol 25: 31-38.

Burgan RE, Rothermel RC (1984) BEHAVE: Fire behavior prediction and fuel modeling system - fuel subsystem, National Wildfire Coordinating Group, Ogden, UT, 126 pp.

Butler BW, Cohen J, Latham DJ, Schuette RD, Sopko P, Shannon KS, Jimenez D, Bradshaw LS (2004) Measurements of radiant emissive power and temperatures in crown fires. Can J Res 34: 1577-1587.

Butler BW, Dickinson MB (2010) Tree injury and mortality in fires – developing process-based models. Fire Ecology 6: 55-79.

Caldwell CR (1993) Estimation and analysis of cucumber (Cucumis sativus L.) leaf cellular heat sensitivity. Plant Physiology 101: 939–945.

Calkin DC, Ager AA, Gilbertson-Day J, Scott JH, Finney MA, Schrader-Patton C, Quigley TM, Strittholt JR, Kaiden JD (2010) Wildfire risk and hazard: procedures for the first approximation, Fort Collins, CO.

Cassagne N, Pimont F, Dupuy JL, Linn RR, Marell A, Oliveri C, Rigolot E (2011) Using a fire propagation model to assess the efficiency of prescribed burning in reducing the fire hazard. Ecol Model 222: 1502-1514.

Cassiani M, Katul GG, Albertson JD (2008) The effects of canopy leaf area index on airflow across forest edges: Large eddy simulation and analytical results. Boundary-Layer Meteorol 126: 433-460.

Chamecki M (2013) Persistence of velocity fluctuations in non-Gaussian turbulence within and above plant canopies. Phys Fluid 25: 1-14.

Chamorro LP, Porte-Agel F (2009) Velocity and Surface Shear Stress Distributions Behind a Rough-to-Smooth Surface Transition: A Simple New Model. Boundary-Layer Meteorol 130: 29-41.

Chatziefstratiou EK, Bohrer G, Bova AS, Subramanian R, Frasson RPM, Scherzer A, Butler BW, Dickinson MB (2013) FireStem2D-A Two-Dimensional Heat Transfer Model for Simulating Tree Stem Injury in Fires. Plos One 8.

Chatziefstratiou EK, Velissariou V, Bohrer G (2014) Resolving the Effects of Aperture and Volume Restriction of the Flow by Semi-Porous Barriers Using Large-Eddy Simulations. Boundary-Layer Meteorol Volume 152: 329-348.

Clements, C. B., B.E. Potter, S. Zhong, 2006: In situ Measurements of Water Vapor, Heat and CO2 Fluxes within a prescribed Grass Fire.International Journal of Wildland Fire, 15(3), 299-306.

Costa JJ, Oliveira LA, Viegas DX, Neto LP (1991) On the temperature distribution inside a tree under fire conditions. Int J Wildland Fire 1: 87-96.

Crank J, Nicolson P (1996) A practical method for numerical evaluation of solutions of partial differential equations of the heat-conduction type. Advances in Computational Mathematics 6: 207-226.

Deardorff JW (1980) Stratocumulus-capped mixed layers derived from a 3-dimensional model. Boundary-Layer Meteorol 18: 495-527.

Detto M, Katul GG, Siqueira M, Juang J-H, Stoy PC (2008) The structure of turbulence near a tall forest edge: The backward facing step flow analogy revisited. Ecol Appl 18: 1420–1435.

Dickinson MB (2002) Heat transfer and vascular cambium necrosis in the boles of trees during surface fires. Proceedings Forest Fire Research & Wildland Fire Safety, Viegas (ed.), Millpress, Rotterdam, ISBN 90-77017-72-0.

Dickinson MB, Johnson EA (2001) Fire effects on trees. Forest fires: behavior and ecological effects. Johnson EA, Miyanishi K, Eds., Academic press, 477-525.

Dickinson MB, Johnson EA (2004a) Temperature-dependent rate models of vascular cambium cell mortality. Canadian Journal of Forest Research 34: 546-559.

Dickinson MB, Jolliff J, Bova AS (2004b) Vascular cambium necrosis in forest fires: using hyperbolic temperature regimes to estimate parameters of a tissue-response model. Aust J Bot 52: 757-763.

Ducrey M, Duhoux F, Huc R, Rigolot E (1996) The ecophysiological and growth responses of Aleppo pine (Pinushalepensis) to controlled heating applied to the base of the trunk. Canadian Journal of Forest Research 26: 1366-1374.

Dupont S, Brunet Y (2008a) Edge flow and canopy structure: A large-eddy simulation study. Boundary-Layer Meteorol 126: 51-71.

Dupont S, Brunet Y (2008b) Impact of forest edge shape on tree stability: a large-eddy simulation study. Forestry 81: 299-315.

Dupont S, Brunet Y, Jarosz N (2006) Eulerian modelling of pollen dispersal over heterogeneous vegetation canopies. Agric Meteorol 141: 82-104.

Dupont S, Patton EG (2012) Momentum and scalar transport within a vegetation canopy following atmospheric stability and seasonal canopy changes: the CHATS experiment. Atmos Chem Phys 12: 5913-5935.

Finney MA (2005) The challenge of quantitative risk analysis for wildland fire. For Ecol Manage 211: 97-108.

Flint HR (1925) Fire resistance of Northern Rocky Mountain conifers. Idaho Forester 7: 7-10, 41-43.

Folkard AM (2011) Flow regimes in gaps within stands of flexible vegetation: laboratory flume simulations. Environ Fluid Mech 11: 289-306.

Fontan S, Katul GG, Poggi D, Manes C, Ridolfi L (2013) Flume experiments on turbulent flows across gaps of permeable and impermeable boundaries. Boundary-Layer Meteorol 147: 21-39.

Gardiner BA, Stacey GR, Belcher RE, Wood CJ (1997) Field and wind tunnel assessments of the implications of respacing and thinning for tree stability. Forestry 70: 233-252.

Gill M, Ashton DH (1968) The Role of Bark Type in Relative Tolerance to Fire of Three Central Victorian Eucalypts. Aust. J. Bot 16: 491-8.

Glass SV, Zelinka SL (2010) Moisture Relations and Physical Properties of Wood. Wood Handbook: Wood as an Engineering Material. Ross RJ, Ed., Forest Products Laboratory, U.S. Department of Agriculture, Forest Service, 4_1-4_19.

Goodrick SL, Achtemeier GL, Larkin NK, Liu Y, Strand TM (2013) Modelling smoke transport from wildland fires: a review. Int J Wildland Fire 22: 83-94.

Gutsell SL, Johnson EA (1996) How fire scars are formed: coupling a disturbance process to its ecological effect. Canadian Journal of Forest Research 26: 166-174.

Hale JD (1955) Thickness and density of bark trends of variation for six pulpwood species. Pulp and Paper Magazine of Canada 56(13): 113-117.

Haltiner GJ, Williams RT (1980) Numerical prediction and dynamic meteorology Wiley & Sons, Inc., 477 pp.

Harman IN, Belcher SE (2006) The surface energy balance and boundary layer over urban street canyons. Q J R Meteorol Soc 132: 2749-2768.

Harmon ME (1984) Survival of trees after low-intensity surface fires in smoky mountains national-park. Ecology 65: 796-802.

Hattori H, Nagano Y (2010) Investigation of turbulent boundary layer over forward-facing step via direct numerical simulation. International Journal of Heat and Fluid Flow 31: 284-294.

Heilman W (2013), Development of Modeling Tools for Predicting Smoke Dispersion from Low-Intensity Fires, Final Report: JFSP Project Number 09-1-04-1, http://www.geo.msu.edu/firesmoke/index.html.

Hoffman C, Morgan P, Mell W, Parsons R, Strand EK, Cook S (2012) Numerical Simulation of Crown Fire Hazard Immediately after Bark Beetle-Caused Mortality in Lodgepole Pine Forests. For Sci 58: 178-188.

Huang J, Cassiani M, Albertson JD (2011) Coherent turbulent structures across a vegetation discontinuity. Boundary-Layer Meteorol 140: 1-22.

Hyde K, Dickinson MB, Bohrer G, Calkin D, Evers L, Gilbertson-Day J, Nicolet T, Ryan K, Tague C (2013) Research and development supporting risk-based wildfire effects prediction for fuels and fire management: status and needs. Int J Wildland Fire 22: 37-50.

Jacoby PW, Ansley RJ, Trevino BA (1992) An improved method for measuring temperatures during range fires. J Range Manage 45: 216-220.

Johansen RW (1987) Ignition paterns and prescribed fire behavior in Southern pine stands. Georgia Forest research paper 72: 1-7.

Jones JK, Webb BW, Jimenez D, Reardon J, Butler B (2004) Development of an advanced one-dimensional stem heating model for application in surface fires. Can J Res 34: 20-30.

Jones JL (2003) Development of an advanced stem heating model. A thesis submitted to the faculty of Brigham Young University.

Jones JL, Webb BW, Butler BW, Dickinson MB, Jimenez D, Reardon J, Bova AS (2006) Prediction and measurement of thermally induced cambial tissue necrosis in tree stems. Int J Wildland Fire 15: 3-17.

Kavanagh KL, Dickinson MB, Bova AS (2010) A way forward for fire-caused tree mortality prediction: modeling a physiological consequence of fire. Fire Ecology 6: 80-94.

Kayll AJ (1963) A technique for studying the fire tolerance of living tree trunks. Canada Dept. Forestry Pub. 1012.

Keane RE, Agee JK, Fule P, Keeley JE, Key C, Kitchen SG, Miller R, Schulte LA (2008) Ecological effects of large fires on US landscapes: benefit or catastrophe? Int J Wildland Fire 17: 696-712.

Klemp JB, Wilhelmson RB (1978) Simulation of 3-dimensional convective storm dynamics. J Atmos Sci 35: 1070-1096.

Laasasenaho J, Melkas T, Alden S (2005) Modelling bark thickness of Picea abies with taper curves. For Ecol Manage 206: 35-47.

Linn RR, Cunningham P (2005) Numerical simulations of grass fires using a coupled atmosphere-fire model: basic fire behavior and dependence on wind speed. Journal of Geophysical Research 110, D13107.

Liu J, Chen JM, Black TA, Novak MD (1996) E-epsilon modelling of turbulent air flow downwind of a model forest edge. Boundary-Layer Meteorol 77: 21-44.

Lorenz R (1939) High temperature tolerance of forest trees. St. Paul: University of Minnesota Agricultural Experiment Station.

Macdonald RW, Carter Shofield S, Lawson PR (2002) Physical modeling of Urban roughness using arrays of regular elements. Water, Air and Soil Pollution 2: 541-554.

Markfort CD, Perez ALS, Thill JW, Jaster DA, Porte-Agel F, Stefan HG (2010) Wind sheltering of a lake by a tree canopy or bluff topography. Water Resour Res 46.

Martin RE (1963a) A basic approach to fire injury of tree stem. 2nd Tall Timbers Fire Ecology Conference 2: 151-162.

Martin RE (1963b) Thermal properties of bark. Forest Products Journal 13: 419-426.

Maurer KD, Bohrer G, Medvigy D, Wright SJ (2013) The timing of abscission affects dispersal distance in a wind-dispersed tropical tree. Funct Ecol 27: 208-218.

McCarthy EF, Sims IH (1935) The relation between tree size and mortality caused by fire in southern Appalachian hardwoods. J For 33: 155-157.

Mell W, Jenkins MA, Gould J, Cheney P (2007) A physics-based approach to modelling grassland fires. Int J Wildland Fire 16: 1-22.

Mell W, Maranghides A, McDermott R, Manzello SL (2009) Numerical simulation and experiments of burning douglas fir trees. Combustion and Flame 156: 2023-2041.

Mercer GN, Weber RO (1994) Plumes above line fires in a cross-wind. Int J Wildland Fire 4: 201-207.

Michaletz ST, Johnson EA, Tyree MT (2012) Moving beyond the cambium necrosis hypothesis of post-fire tree mortality: cavitation and deformation of xylem in forest fires. New Phytol 194: 254-263.

Michaletz ST, Johnson EA (2008) A biophysical process model of tree mortality in surface fires. Can J Res 38: 2013-2029.

Millikin DE (1955) Determination of bark volumes and fuel properties. Pulp and Paper Magazine of Canada 56(13): 106-108.

Monson R, Baldocchi D (2014) Terrestrial Biosphere-Atmosphere FluxesTerrestrial Biosphere-Atmosphere Fluxes.

Morvan D, Dupuy JL (2001) Modeling of fire spread through a forest fuel bed using a multiphase formulation. Combustion and Flame 127: 1981-1994.

Paik J, Sotiropoulos F, Porte-Agel F (2009) Detached eddy simulation of flow around two wall-mounted cubes in tandem. International Journal of Heat and Fluid Flow 30: 286-305.

Panferov O, Sogachev A (2008) Influence of gap size on wind damage variables in a forest. Agric Meteorol 148: 1869-1881.

Parsons RA, Mell WE, McCauley P (2011) Linking 3D spatial models of fuels and fire: Effects of spatial heterogeneity on fire behavior. Ecol Model 222: 679-691.

Patankar SV (1980) Numerical heat transfer and fluid flow. Hemisphere Publishing Corporation.

Patton EG, Sullivan PP, Ayotte KW (2006) Flow and transport above and within forests in complex topography. Integrated Land-Ecosystem Atmosphere Study Conference, Boulder, CO., 376 pp.

Patton EG, Shaw RH, Judd MJ, Raupach MR (1998) Large-eddy simulation of windbreak flow. Boundary-Layer Meteorol 87: 275-306.

Peterson DL, Ryan KC (1986) Modeling Postfire Mortality for Long-range Planning. Environment Management 10: 797-808.

Pimont F, Dupuy JL, Linn RR, Dupont S (2011) Impacts of tree canopy structure on wind flows and fire propagation simulated with FIRETEC. Ann For Sci 68: 523-530.

Poggi D, Porporato A, Ridolfi L, Albertson JD, Katul GG (2004) The effect of vegetation density on canopy sub-layer turbulence. Boundary-Layer Meteorol 111: 565-587.

Potter BE, Andresen JA (2002) A finite-difference model of temperatures and heat flow within a tree stem. Canadian Journal of Forest Research 32: 555-584.

Prueger JH, Eichinger WE, Hipps LE, Hatfield JL, Cooper DI (2008) Air-flow distortion and turbulence statistics near an animal facility. Atmos Environ 42: 3301-3314.

Regland KW, Aerts DJ (1991) Properties of wood for combustion analysis. Bioresource Technology 37: 161-168.

Rego F, Rigolot E (1990) Heat transfer through bark-a simple predictive model. Third International Symposium on Fire Ecology:Fire in Ecosystem Dynamics: 257-161.

Reinhardt ED, Ryan KC (1989) Estimating Tree Mortality Resulting From Prescribed Fire. Prescribed Fire in the Intermountain Region Forest Site Preparation and Range Improvement Symposium.

Ryan KC, Frandsen WH (1991) Basal injury from smoldering fires in mature Pinus ponderosa Laws. Int J Wildland Fire 1: 107-118.

Santiago JL, Martin F, Cuerva A, Bezdenejnykh N, Sanz-Andrés A (2007) Experimental and numerical study of wind flow behind windbreaks. Atmos Environ 41: 6406-6420.

Schlegel F, Stiller J, Bienert A, Maas HG, Queck R, Bernhofer C (2012) Large-eddy simulation of inhomogeneous canopy flows using high resolution terrestrial laser scanning data. Boundary-Layer Meteorol 142: 223-243.

Seraphin A, Guyenne P (2008) A flume experiment on the adjustment of the mean and turbulent statistics to a transition from short to tall sparse canopies. Boundary-Layer Meteorol 129: 47-64.

Shaw RH, Patton EG (2003) Canopy element influences on resolved- and subgrid-scale energy within a large-eddy simulation. Agric Meteorol 115: 5-17.

Shirley HL (1936) Lethal high temperatures for conifers, and the cooling effect of transpiration. Journal of Agricultural Research 53: 239-258.

Siau JF (1983) A proposed theory for non-isothermal unsteady state transport of moisture in wood. Wood Sci Technol 17: 75-77.

Simpson W, TenWolde A (1999) Wood handbook-Wood as an engineering materialU.S. Department of Agriculture, Forest Service, Forest Products Laboratory.

Spalt KW, Reifsnyder WE (1962) Bark characteristics and fire resistance: a literature surveySouthern Forest Experiment Station, Forest Service, U.S. Departments of Agriculture in cooperation with school of Forestry, Yale University.

Starker TJ (1934) Fire resistance in the forest. J For 32: 462-467.

Sullivan AL (2009) Wildland surface fire spread modelling, 1990-2007. 1: Physical and quasi-physical models. Int J Wildland Fire 18: 349-368.

Van Hooff T, Blocken B (2010) Coupled urban wind flow and indoor natural ventilation modelling on a high-resolution grid: A case study for the Amsterdam ArenA stadium. Environ Modell Softw 25: 51-65.

Vines RG (1968) Heat transfer through bark, and the resistance of trees to fire. Aust J Bot 16: 499-514.

Wade DD, Lunsford JD (1989) A guide for prescribed fire in southern forestsU.S. Department of Agriculture, Forest Service.

Waldrop TA, Goodrick SL, Harper CA (2012) Intoduction to prescribed fire in southern ecosystems.

Walko RL, Avissar R (2008) The Ocean-Land-Atmosphere Model (OLAM). Part II: Formulation and tests of the nonhydrostatic dynamic core. Mon Weather Rev 136: 4045-4062.

Winstral A, Marks D, Gurney R (2013) Simulating wind-affected snow accumulations at catchment to basin scales. Adv Water Resour 55: 64-79.

Wolfe GM, Thornton JA (2011) The Chemistry of Atmosphere-Forest Exchange (CAFE) Model - Part 1: Model description and characterization. Atmos Chem Phys 11: 77-101.

Yang B, Raupach M, Shaw RH, U KTP, Morse AP (2006) Large-eddy simulation of turbulent flow across a forest edge. Part I: flow statistics. Boundary-Layer Meteorol 119: 377-412, DOI: 10.1007/s10546-006-9083-3.

Yue W, Parlange MB, Meneveau C, Zhu W, van Hout R, Katz J (2007) Large-eddy simulation of plant canopy flows using plant-scale representation. Boundary-Layer Meteorol 124: 183-203.